UNIVERSITY OF CAPE COAST

VALIDATION OF PLANNED RADIATION ABSORBED DOSE FOR BREAST CANCER TREATMENT USING RADIOMETRIC FILM DOSIMETER

BY

THERESA BEBAAKU DERY

Thesis submitted to the Department of Physics of the School of Physical Sciences, College of Agriculture and Natural Sciences, University of Cape Coast, in partial fulfilment of the requirements for the award of Doctor of Philosophy degree in Physics

JULY 2018

DECLARATION

Candidate's Declaration

I hereby declare that this thesis is the result of my own original research and that no part of it has been presented for another degree in this university or elsewhere.

Candidate's Signature: .... Date: ..24/04/2019..

Name: Theresa Bebaaku Dery

Supervisors' Declaration

We hereby declare that the preparation and presentation of the thesis were supervised in accordance with the guidelines on supervision of thesis laid down by the University of Cape Coast.

Principal Supervisor's Signature:........................ Date: 24/04/2019

Name: Dr. Joseph Kwabena Amoako

Co-Supervisor's Signature:........................ Date: 24/04/2019

Name: Professor Paul Kingsley Buah-Bassuah

ABSTRACT

The essential role of radiotherapy is to ensure detection and treatment of breast cancers using appropriate doses, these seem not to harm patients under review. Unintended detriments in the treatment and the risk of secondary cancers are mostly associated with delivering much higher doses than planned dose. This study focused on using phantoms for the determination, and comparison of planned doses with actual doses delivered to the breast, during radiation treatment. Adelaide phantoms were constructed using locally procured materials to mimic the surrounding tissues of the human female thoracic cavity. Balloons, mango seed, cassava stick and candle were radiologically assessed and used as surrogates for the lung, heart, spinal cord and glandular tissue of the breast respectively. EBT3 film dosimeter was used with the standard (anthropomorphic) and Adelaide phantoms to measure doses absorbed by the breast and non-target organs; the doses were delivered from Co-60 and linear accelerator systems. Monte Carlo N-Particle transport code was also used on a virtual phantom to compute the dose distribution from the cobalt machine. The spinal cord absorbed the lowest dose of 0.03 ± 0.02 Gy and 0.05 ± 0.01 Gy, while the left lung received the highest doses of 0.74 ± 0.04 Gy and 0.78 ± 0.01 Gy for Co-60 and LINAC respectively. Based on the findings, it was clearly determined that the target organ received the expected dose within the acceptable tolerance level of 5%. Additionally, the non-target organs equally received a minimuim radiation dose according to required standards. A non-clinical significance differences of planned and delivered doses were achievable following appropriate quality control both with anthropomorphic and constructed phantoms.

KEY WORDS

Dosimetry

Hounsfield Unit

Monte Carlo

Phantom

Radiochromic film

Radiotherapy

ACKNOWLEDGEMENTS

My most sincere thanks go to my principal supervisor Dr. J. K. Amoako, for being instrumental in creating the initial impetus of this thesis and his ability to push me beyond my own abilities and my co-supervisor Prof. P. K. Buah-Bassuah, for his innovative ideas and fruitful discussions, making sure all of the analyses conducted in this thesis were of high quality. To my employer, Ghana Atomic Energy Commission, and to the Head and staff of the Department of Physics, University of Cape Coast for their support throughout my study.

My special thanks go to the staff of the Sweden Ghana Medical Centre and the Oncology Department, Korle-Bu Teaching Hospital, especially, Mr. G. F. Acquah, Mr. P. Kyeremeh, Mr. D. Gadeka, Mr. S. N. Tagoe, Mr. E. O. Nkansah, and Mr. A. B. Ashun, who helped me in setting the dosimetry equipment for the required measurements. Thanks to Dr. A. K. Awua for all his input on clinical questions, scientific writing and statistical discussions, and to Mr. W. Osei-Mensah, who assisted me with the Monte Carlo simulation.

I owe a great deal of thanks to Prof. A. K. Kyere and Mr. A. D. Jirapa for their constant encouragement. Thanks to Prof. M. Boadu, for her understanding, encouragement and motivation. Thanks to Mr. B. Dery for his assistance in the thesis grants. Thanks to Dr. F. Hasford, who read my thesis and made very insightful comments. I am greatly indebted to Mr. G. Anane-Antwi, for his invaluable help during the thesis write-up. I greatly cherish all the support from my friends, especially Mr. M. Pokoo-Aikins and Mr. D. N. Adjei. Thanks to my dear parents and siblings, for their constant love and prayers. The work presented in this thesis was made possible through grants from the Ghana Educational Trust Fund (GETFund).

DEDICATION

To my principal supervisor, Dr. Joseph Kwabena Amoako

TABLE OF CONTENTS

	Page
DECLARATION	ii
ABSTRACT	iii
KEY WORDS	iv
ACKNOWLEDGEMENTS	v
DEDICATION	vi
TABLE OF CONTENTS	vii
LIST OF TABLES	xii
LIST OF FIGURES	xv
LIST OF ACROYMNS	xix
LIST OF SYMBOLS AND CONSTANT	xxii
CHAPTER ONE: INTRODUCTION	1
Background to the Study	1
Statement of the Problem	4
Research Questions	7
Objectives of the Study	8
Scope	8
Relevance and Justification	9
Limitation	10
Organisation of the Study	10
Chapter Summary	11
CHAPTER TWO: LITERATURE REVIEW	12
Introduction	12
Photon Interaction Mechanism	12

Radiation Dosimetry 15

Phantom 17

Breast Composition 20

Dosimetry Protocols 24

Dosimetric Verification 24

Dosimeter Characteristics 25

Radiochromic Film 27

Optical Density Spectrum 28

Film Characteristic Curve 29

Photon Dose Algorithm 32

Radiotherapy Technology 33

Cobalt Teletherapy Machine 34

Linear Accelerator 35

Computed Tomography 37

Computed Tomography Numbers 39

Electron Density Characterization 40

ImageJ Software 42

Chapter Summary 43

CHAPTER THREE: MATERIALS AND METHODS 44

Introduction 44

Health Facility 44

Equipment 45

Water and Solid Phantoms 45

Ionization Chamber 47

Electrometer 48

Barometer and Thermometer	49
GafChromic EBT3 Film Dosimeter	49
Performance of Quality Control	50
Dosimetric Check	50
Mechanical Check	52
Safety Check	53
Calibration of Radiometric Films	54
Cutting of GafChromic EBT3 Film	54
Irradiation of GafChromic EBT3 Films	55
Scanning of GafChromic EBT3 Films	58
Reading of GafChromic EBT3 Films	59
Phantom Design	61
Fabrication of Phantoms	64
Tissue-Substitutes	67
Experimental Dose Measurement	69
Theoretical Dose Measurement	72
Monte Carlo Geometry	72
Statistical Analysis	77
Chapter Summary	79
CHAPTER FOUR: RESULTS AND DISCUSSION	80
Introduction	80
Results of Dosimetric Checks	80
Ionization Chamber Correction Factors	81
Temperature-Pressure Correction Factors	81
Radiation Beam Output Factor	83

Results of Mechanical Checks 85

Radiation Safety Survey 87

Evaluation of GafChromic EBT3 Film Dosimetry 88

Film Calibration and Sensitivity 89

Optical Density and Dose 91

Energy and Film Response 94

Dose and Film Area 96

GafChromic EBT3 Film Orientation 98

Scanners of GafChromic EBT3 Films 100

Scanner Uniformity 103

Results of Virtual Simulation 106

Dose Validation 113

Tissue Characterization 113

Validation of Ionization Chamber Measurements 115

Validation of Phantom Measurements 118

Validation of Critical Organ Doses 120

Chapter Summary 122

CHAPTER FIVE: CONCLUSIONS AND RECOMMENDATIONS 123

Overview 123

Summary 123

Conclusions 125

Recommendations 127

REFERENCES 128

APPENDICES 147

APPENDIX A: Worksheet for the Determination of Absorbed Dose 147

APPENDIX B: Equipment Specification for EBT3 Irradiation	149
APPENDIX C: Tissue Compositions and Densities Based on ICRU 44	150
APPENDIX D: Photon Plan Summary for Left Breast	151
APPENDIX D-1: Beam Information for 6 MV	151
APPENDIX D-2: Beam Information for 1.25 MeV	152
APPENDIX E: Quadrants of MCNP	153
APPENDIX E-1: Reference plane section into smaller volumes	153
APPENDIX E-2: First layer from ^{60}Co source	153
APPENDIX E-3: Second Layer from ^{60}Co source	153
APPENDIX E-4: Third Layer from ^{60}Co source	154
APPENDIX E-5: Fourth Layer from ^{60}Co source	154
APPENDIX E-6: Fifth Layer from ^{60}Co source	154
APPENDIX F: Optical Densities of the Energy Beams	156
APPENDIX G: Dose Measurement with Ionization Chamber	157
PUBLISHED ARTICLES FROM THESIS	158

LIST OF TABLES

Table		Page
1	Representation of Errors based on Location of Treatment	7
2	Characteristics of Photoelectric Effect, Compton Effect and Pair Production	14
3	Physical Properties of various Phantom Materials	20
4	Typical Values and Ranges for Different Tissues and Materials	40
5	Specification of the Machines used for the Study	45
6	Technical Specification of the Solid Phantom used in the Study	46
7	Ionization Chamber Specifications used in the Study	47
8	Elemental Composition of Perspex	63
9	Properties of Polystyrene	64
10	Reference Conditions for the Determination of Absorbed Dose to Water in ^{60}Co Gamma Ray Beams	73
11	Temperature and Pressure Correction Factors for LINAC and ^{60}Co Machines	82
12	Beam Output Results from Dosimetric Data	83
13	Results of Output Constancy with Gantry Angle	84
14	Results of the Output Linearity Test	85
15	Results from Mechanical Data for Cobalt-60 Machine	86

16	Results from Mechanical Data for Linear Accelerator Machine	87
17	Results of Radiation Safety Checks	88
18	Radiation Survey for Treatment Room	88
19	Summary of the Polynomial Regression Analysis for the RGB Channels	93
20	Relationship between Dose and Area of the Different Film Sizes	97
21	Error of Measured and Calculated Doses for ROI	98
22	Percentage Difference of Film Response between Landscape and Portrait Orientations	99
23	EBT3 Film Scanning Parameters	102
24	Epson Scanner Response to Doses	103
25	The Mean Pixel Values and Standard Deviations of the EBT3 film at Different Positions on the Scanner of Area 2400 mm^2	104
26	ANOVA for the MCNP Model	111
27	Hounsfield Units of Local Materials used in the Study in Comparison with HU for Human Tissues	114
28	Radiological Properties of Selected Materials	115
29	Results of Farmer Type Ionization Chamber Measurement	116
30	ANOVA of Ionization Chamber Measurements	117
31	Phantom Measurement for LINAC Irradiation	118

32 Deviations of Phantom Measurement for LINAC Irradiation 119

33 Phantom Measurement and Deviations for Co-60 Irradiation 120

34 Average Doses for Organs Around the Target Left Breast for Intact Breast 121

16	Results from Mechanical Data for Linear Accelerator Machine	87
17	Results of Radiation Safety Checks	88
18	Radiation Survey for Treatment Room	88
19	Summary of the Polynomial Regression Analysis for the RGB Channels	93
20	Relationship between Dose and Area of the Different Film Sizes	97
21	Error of Measured and Calculated Doses for ROI	98
22	Percentage Difference of Film Response between Landscape and Portrait Orientations	99
23	EBT3 Film Scanning Parameters	102
24	Epson Scanner Response to Doses	103
25	The Mean Pixel Values and Standard Deviations of the EBT3 film at Different Positions on the Scanner of Area 2400 mm^2	104
26	ANOVA for the MCNP Model	111
27	Hounsfield Units of Local Materials used in the Study in Comparison with HU for Human Tissues	114
28	Radiological Properties of Selected Materials	115
29	Results of Farmer Type Ionization Chamber Measurement	116
30	ANOVA of Ionization Chamber Measurements	117
31	Phantom Measurement for LINAC Irradiation	118

32	Deviations of Phantom Measurement for LINAC Irradiation	119
33	Phantom Measurement and Deviations for Co-60 Irradiation	120
34	Average Doses for Organs Around the Target Left Breast for Intact Breast	121

LIST OF FIGURES

Figure		Page
1	Diagram of energy range of photon interactions with material	13
2	Photon radiation transfers energy to charged particles through the medium	15
3	Absorbed energy and dose process within a given volume of matter	17
4	Picture of rando (female) anthropomorphic phantom sectioned transversely for dosimetric studies	18
5	Illustration of the anatomy of the breast	21
6	Fields in a breast treatment	21
7	Geometry of distance, depth and scatter	22
8	Illustration of percentage depth dose	23
9	Characteristic curve of film density versus log exposure	30
10	Plots of film response curves of optical density versus log exposure: (a) H&D curve; (b) H&D curve with contrast; (c) sensitometric; (d) dosimetry	31
11	Decay scheme of Co-60	34
12	Theratron equinox 100 Co-60 machine at National Centre of Radiotherapy and Nuclear Medicine, Korle-Bu, Accra, Ghana	35
13	Schematic diagram of a typical linear accelerator	36

14	Elekta synergy linear accelerator machine at Sweden Ghana Medical Centre, Accra, Ghana	37
15	CT image acquisition showing the transmission of X-rays through the patient by using (a) detector row, (b) with rotation of the x-ray tube and detector and (c) by multiple detector	38
16	Phantoms: (a) water phantom filled with water (b) solid plates phantom	46
17	Farmer type ionization chamber	48
18	PTW UNIDOS electrometer	48
19	Configuration of EBT3 Radiometric Film	50
20	Pieces of EBT3 film	55
21	Solid plates phantom setup	57
22	Irradiation setup for Cobalt-60	58
23	Scanned EBT3 films of 2 cm x 3 cm dimensions: (a) unexposed films; (b) exposed to 6 MV beam energy	59
24	Splitting of channel into RGB colours	60
25	Images of EBT3 films and scanning process using the red channel	61
26	A picture of the polystyrene used in the study	64
27	A picture of the Adelaide phantom a	65
28	Scan images of the anthropomorphic phantom	66
29	Adelaide phantom B construction processes	67
30	A picture of the Adelaide phantom B	67
31	CT scan of the Adelaide phantom A	68

32	Representation of dose point information	70
33	Setup of the irradiation of the anthropomorphic phantom with EBT3 Films: (a) intact breast; (b) mastectomy	71
34	Setup of the irradiation of the Adelaide phantom A with EBT3 Films: (a) intact breast; (b) mastectomy	71
35	Setup for irradiation geometry for beam calibration	74
36	MCNP 3D geometric view of simulated virtual phantom	75
37	MCNP 2D geometric view of simulated virtual water phantom: (a) 50x10 simulated tissue meshing in x-z plane (b) cross sectional view of 50x50 simulated tissue meshing in x-y plane	75
38	Characteristic curve of EBT3 film for 1.25 MeV beam energy from cobalt machine	89
39	Characteristic curve of EBT3 film for 6 MV beam energy of linear accelerator	90
40	Characteristic Curve of EBT3 Film for 15 MV beam energy of linear accelerator	90
41	Relationship between optical density and dose from different energy sources: (a) 1.25 MeV, (b) 6 MV, (c) 15 MV	92
42	Energy dependence of EBT3 Film	94
43	Relationship between dose, optical density and energy: (a) MeV; (b) MV	95

44	Relationship between energy and dose	96
45	Scanning orientation of EBT3 films	99
46	Different types of scanners and dose	101
47	Scatter plot of optical density and scanner position of the EBT3 films	105
48	Energy deposition at the first to fourth layers	107
49	Energy deposition at the fifth to eighth layers	108
50	Energy deposition at the ninth and tenth layers	109
51	Relative absorbed dose in each meshed layer	110
52	A graph of absorbed dose and depth	112
53	Plot for measured dose versus expected dose for 1.25 MeV	116
54	Plot for measured dose versus expected dose for 6 MV	117
55	Plot for measured dose versus expected dose for 15 MV	117

LIST OF ACRONYMS

1-D	One Dimensional
AAPM	American Association of Physicist in Medicine
ACS	American Cancer Society
ANOVA	Analysis of Variance
AOAC	Association of Official Analytical Chemist
BMP	Basic Multilingual Plane
CF	Correction Factor
CNSC	Canadian Nuclear Safety Commission
CT	Computed Tomography
DD	Delivered Dose
DF	Decay Factor
DF	Degree of Freedom
DICOM	Digital Imaging and Communication in Medicine
DNA	Deoxyriobonucleic Acid
dpi	Dot per inch
EcoLab	Ecological Laboratory
FAAS	Flame Atomic Absorption Spectrometry
FITS	Flexible Image Transport System
GIF	Graphical Interchange Format
H-D	Hurter - Driffield
HU	Hounsfield Unit
IAEA	International Atomic Energy Agency
IARC	International Agency for Research on Cancer
ICRP	International Commission on Radiation Protection
ICRU	International Commission on Radiation Units and Measurements
ISF	Inverse Square Factor

ISP	International Specialty Products
JPEG	Joint Photographic Experts Group
KERMA	Kinetic Energy Released Per Unit Mass
LINAC	Linear Accelerator
MATLAB	Matrix Laboratory
MC	Monte Carlo
MCNP	Monte Carlo Neutral Particle
MRI	Magnetic Resonance Imaging
MS	Mean Squares
MU	Monitor Unit
NCRNM	National Centre for Radiotherapy and Nuclear Medicine
OAR	Organs at risk
OD	Optical Density
ODI	Optical Distance Indicator
P	Pressure
PCF	Phantom Correction Factor
PD	Planned Dose
PDD	Percentage Depth Dose
PET	Positron Emission Tomography
PMMA	Poly Methyl Methacrylate
POP	Plaster of Paris
PVC	Polyvinyl Chloride
QC	Quality Control
RGB	Red Green Blue
ROI	Region of Interest
RTOG	Radiation Therapy Oncology Group
SAD	Source-to-Axis Distance

SGMC	Sweden Ghana Medical Centre
SS	Sum of Squares
SSD	Source-to-Surface Distance
T	Temperature
TBq	Tera Becquerel
TF	Tray Factor
TG	Task Group
TIFF	Tagged Image File Format
TLD	Thermo Luminescence Dosimeter
TPR	Tissue Phantom Ratio
TPS	Treatment Planning System
TRS	Technical Report Series
TT	Treatment Time
UCCIRB	University of Cape Coast Institutional Review Board
WF	Wedge Factor
WHO	World Health Organization

LIST OF SYMBOLS AND CONSTANT

Symbol	Meaning	Unit
a	Equivalent square	cm
a_c	Source activity	Bq
φ	Particle fluence	m^{-2}
μ_{tr}/ρ	Mass energy transfer coefficient	m^2/kg
d	Depth	cm
d_0	Reference depth	cm
$D_{W,5}$	Absorbed dose to water	Gy
$t_{1/2}$	Half life	s
I	Intensity	W/m^2
I_0	Unattenuated intensity	W/m^2
T_0	Reference temperature	°C
N_A	Avogradro's number	mol
P_0	Reference pressure	kPa
r_d	Field size at depth	cm
T_0	Reference temperature	°C
μ	Linear attenuation	cm^{-1}
x	Thickness	cm
ρ_Q	Electron density	g^{-1}
D	Dose	Gy
E	Energy	J
L	Length	cm
m	Mass	kg

V	Volume	cm^3
W	Width	cm
k	Proportionality constant	
N_{CT}	CT Number	
^{60}Co	Cobalt-60	
$N_{D,W}$	Detector Calibration Factor	
e^-	Electron	
e^+	Positron	
σ	Standard deviation	
γ	Gamma	
k_{ele}	Electrometer calibration factor	
k_{pol}	Polarity voltage	
k_s	Recombination correction factor	
$k_{T,P}$	Temperature Pressure Correction Factor	
r_c	Field size defined by collimator jaws	
R^2	Coefficient of determinant	
S_c	Air output ratio	
S_p	Phantom scatter factor	
Z_{ref}	Reference point of chamber	
$\% \, Diff$	Percentage difference	
δ	Percentage error	
A	Mass number	
C	Carbon	
Ca	Calcium	
Cd	Cadium	

Co	Cobalt
Fe	Iron
H	Hydrogen
H_20_2	Hydrogen peroxide
HNO_3	Nitric Acid
K	Potassium
Mg	Magnesium
Mn	Manganese
N	Nitrogen
Ni	Nickel
O	Oxygen
Sn	Tin
Z	Atomic number
$Z^{\#}$	Effective Atomic Number
Zn	Zinc

CHAPTER ONE

INTRODUCTION

This chapter gives the basic fundamental principles, of the use of radiation in the treatment of breast cancers. The problems identified and the objectives are presented. The relevance of the study is explained. The methodology of the study, specifically, the use of phantoms and radiochromic dosimeter in assessing the doses delivered is also presented and discussed. Finally, the chapter concludes with a summary on the organization of the research work.

Background to the Study

Cancer, the second leading cause of death worldwide (GLOBOCAN, 2012), is a group of diseases characterized by uncontrolled growth and spread of abnormal cells. Of these cancers, breast cancer, the erratic growth and proliferation of cells that originate in breast tissues, is the most frequently diagnosed cancer among women globally (GLOBOCAN, 2012). For advanced breast cancer, the tumour cells of the breast may break away and translocate to other parts of the body, causing advanced complications. Breast cancer treatment is more effective and a cure is more likely, when it is detected as early as possible (Allemani et al., 2015). According to the World Cancer Report, breast cancer incidence could go up by 50% to 1.5 million by 2020 as reported by Mahavir and Babita (2013). Breast cancers begin immensely in lobules, where breast tissue that is made up of glands for milk production and connecting ducts are located. The rest of the breast is made up of fatty, connective, and lymphatic tissues as described by American Cancer Society, (2016).

Radiation therapy is one of the major treatment options for cancers;

others include surgery, radiation therapy, and/or systemic therapy (e.g., chemotherapy, hormonal therapy, immune therapy, and targeted therapy). These treatment options may be used alone or in combination, depending on the type and the stage of the cancer, tumour characteristics and patient's age. The World Health Organization [WHO] reports that 60% of all cancer patients require radiation at one point during their treatment and that 40% of cancer cure results from radiotherapy (WHO, 2008).

The ultimate aim of radiotherapy is to deliver a measured dose to a specified volume, with the purpose of eradicating the tumour and sparing the surrounding normal tissue with minimal damage (Cherry & Duxbury, 2009). During radiation therapy, a high-energy beam is used to kill cancer cells. The beam may be delivered from a source outside the body (external beam radiation) or a source placed inside the body (brachytherapy) using either orthovoltage units, linear accelerators, or Cobalt-60 isotope machine (Darby et al., 2011). The standard for radiation therapy for women with breast cancer is external beam radiation (Haviland et al., 2013). This is non-invasive and allows for sparing normal healthy tissues and increase in dose to target (Baker, 2006). Different doses of radiation are needed for tumour control, depending on the type and initial number of clonogenic cells present, that is, cells from which tumours may be generated or regenerated. Radiation dose is delivered in fractionation with three portal compartments, plus a margin to compensate for geometric inaccuracies during the treatment period (Forrest, 2003).

The accuracy with which radiation dose is delivered to the tumour is the core of the systematic plan for therapy. This plan includes dose calculations and delivery of radiation beam. The accuracy is necessary in order to make sure that the dose delivered to the target is 100% or close to 100%. To ensure this, a physical phantom made of a solid material and/or a computational phantom, which is radiologically equivalent to human tissues, with the same absorption and scattering properties as water, since the human body consists mostly of water, is used to estimate the dose inside the body. Spiers (1943), showed that a phantom material should have the same density as the tissue it represents and must contain the same number of electrons per gram.

Water as a tissue substitute in radiation measurement was the first material to be used according to Kienbock (1906). This is because, it absorbs X-rays of various energies very much like muscle tissue of the body, it is readily available and it is easy to place a detector in at various depths and positions perpendicular to the vertical beam, provided the detector is waterproof. According to DeWerd & Kissick (2014), homogenized water or plastic phantoms are widely used for the calibration of radiation detectors and treatment systems.

Dose calculation is also a key component of a treatment planning system (TPS) (Lu, 2013). This is characterized by various parameters in the treatment machine used to deliver the radiation. This planning process is performed with patient's images to identify the anatomical structures and the machine parameters in order to simulate the actual treatment using a computing software. Success in estimation of this planned dose and its outcome are entirely dependent on the delivered dose to the respective site of the patient, with reproducible accuracy of estimation of the planned dose or within variation tolerance (Washington & Leaver, 2003). In radiotherapy treatment planning, scanned tumour volumes are defined specific to the region of interest to minimize the doses to the surrounding healthy tissues.

Clinically, dose planning systems have until recently used algorithms for photons, which make use of empirically determined inhomogeneity corrections. The methods used for calculating absorbed dose are classified as correction-based and model-based (Mackie et al., 1996; Van Dyk, 1999). The correction-based method was used to determine dose from the reference dose, measured under the standard conditions in a water phantom with some adjustments to account for specific treatment conditions such as contouring and inhomogeneities. The model-based method based on Monte Carlo, was also employed in the study to determine the dose distribution from the transportation of radiation.

Statement of the Problem

For this study, some major challenges with the use of radiation therapy for breast cancers in terms of complexities of the organ (breast), dose optimization, errors associated with measurement and calculation of doses in clinical oncology procedures globally and locally were identified.

Firstly, cancer worldwide accounts for 14% of all deaths among females (American Cancer Society, 2017). According to estimates from the World Health Organization [WHO] and International Agency for Research on Cancer (IARC), 3.5 million deaths and 6.7 million new cancer cases among females occurred worldwide in 2012 (GLOBOCAN, 2012; Ferlay et al., 2013). American Cancer Society, (2017) predicted that an increase to 5.5 million deaths and 9.9 million new cases among females is expected annually by 2030 due to the growth and aging of the population.

In Ghana, women are disproportionately afflicted with breast cancer at younger age, and the commonest cause of cancer death in females is malignancies of the breast, accounting for 17.24% of all cancer (American Cancer Society, 2010). Research studies have so far shown no single cause of breast cancer but some factors that appear to increase the likelihood of developing the disease include being a female, increasing age, and family history of breast cancer. Therefore, it is important to carefully evaluate the distribution of radiation energy absorbed by breast tissues and surrounding tissues and organs during the therapy procedure to avoid future occurrences, since a lot more women are likely to be diagnosed with breast cancer and therefore receive radiation for treatment.

Secondly, literature review on radiation therapy for breast cancer states that planning for breast cancer cases is technically challenging because of the varying size and shape of the breast/chest as well as the setup reproducibility and respiratory motion (Balaji et al., 2016). On account that it causes poor conformity, homogeneity, and hot spots outside the target volume. According to International Commission on Radiation Units and Measurements [ICRU] Report No. 50 and 62, the dose distribution delivered should be within +7% and -5% of the prescribed dose without exceeding the tolerance dose of the critical structure around the tumour volume (ICRU, 1993; 1999). To achieve this tolerance, such irregularities need to be corrected. Therefore, for this study phantoms were developed and tailored for the varying size and shape of breast to evaluate the actual radiation doses.

Thirdly, a direct measurement of the distribution of dose delivered to a cancer patient is essentially practically impossible. For a successful radiation treatment outcome, planning based on calculation models is much practical to perform (Korhonen, 2009). Hence, the radiation beam to the tumour needs to be planned, and in order to have a specific amount absorbed by the tumour to kill the tumour cells. The prescribed dose should correspond to the delivered absorbed dose in the patient as accurately as possible. The dose received by the tumour volume should be close to the prescribed dose level, this is because certain organs have critical dose levels that should not be exceeded, or otherwise serious side effects (infection, skin burns, irritation, fatigue, and lymphedema) might occur. In addition, the biological response of the cells to radiation is highly nonlinear, and therefore small errors in the predicted dose may lead to large errors in prediction of the biological response (Ahnesjö & Aspradakis, 1999).

Fourthly, in radiotherapy there is a potential of human error occurrence which might result in either an under dose or overdose. An additional dose to the target volume may lead to increased complications of inflamed lung tissue, heart damage and secondary cancers, to the normal tissues of a patient. It is important to minimize the error occurrences and their consequences. Asnaashari, Gholami and Khosravi (2014) conducted an investigation, which focused on the determination of probability of errors as a function of treatment organs at a radiotherapy centre. Table 1 shows the results obtained during their investigations.

Table 1: Representation of Errors based on Location of Treatment

Treatment Location	Number of Reports	% of Total
Head and Neck	47	34
Breast	38	28
Thorax	5	3
Abdomen	13	10
Pelvis	30	23
Other organs	3	2
Total	136	100

Source: Asnaashari et al., 2014

From Table 1, it was realized that the total errors for the breast was 28%, which is relatively higher compared to those for pelvis and abdomen. The findings were that most of the outstanding reasons of error occurrence was lack of full concentration of staff with other factors attributed to poor communication and transfer of information between staff. Nonetheless, not only the above are the only sources of error between the predicted and the delivered dose distributions, but other subsequent factors as well which include the wrong calculation of the dose rate and irradiation times for patients at the treatment units can also contribute to the overall error.

Finally, geometric uncertainty also contributes to dose problems to the organs at risk (OAR), by decreasing (underdose) or increasing (overdose) the required volume dose, as well as time of irradiation. This is as a result of difficulties with equipment (calibration and beam output) and mechanical related problems depending on the treatment techniques employed.

Research Questions

The research questions designed were as follows:

a) Is the planned dose (PD) significantly less than the delivered dose (DD)?

b) Does the critical organ receive more dose than the acceptable tolerance?

c) Is there a linear relationship between the delivered dose and the depth (distance) of penetration?

Objectives of the Study

The overall aim of this study was to assess the differences between planned and delivered radiation doses to constructed phantoms mimicking the female breast during radiation therapy.

This specifically led to the following:

a) Assess radiation dose received at a specific location in the target organ and within non-target organs during breast therapy.

b) Simulate absorbed dose delivered using the Monte Carlo N- Particle (MCNP) transport code.

Scope

The scope of the work was confined to the use of photon beams of X-ray energies, 6 MV and 15 MV, and gamma of 1.25 MeV used in external beam radiotherapy. The study employed a radiochromic film dosimeter to measure the absorbed dose at various depths in the phantoms used.

In this study, phantoms were constructed from local materials, to mimic the thoracic part of the female body, including the breast, for the dose verification. The phantoms had removable breasts and could be dismantled into transverse segments for the placement of detectors. The verification was done for two plans: one for the left side with the breast removed to represent the chest wall irradiation after mastectomy and one for the right side with the breast attached to represent the intact breast irradiation.

Again, Monte Carlo method was used to model the distribution of energy deposited in each photon interaction in an intended patient mimicking the phantom by simulating the shape, material and the system geometry of the cobalt machine.

Relevance and Justification

Accuracy and precision of dose delivery are primary requirements for effective and efficient treatment, because high doses are delivered to the cancerous tumours. Therefore, dosimetric verification prior to patient treatment, which has a key role in accuracy and precision in radiotherapy delivery is very essential. According to International Commission on Radiation Units and Measurements [ICRU] Report No. 83 published in 2010, the biggest contributors to treatment failures include geographical miss, due to inaccurate target delineation and dosimetric variation of more than 3% (ICRU, 2010). Moreover, a small difference in the delivered dose can make big differences in tumour control probability and in the avoidance of secondary induced cancer during breast cancer treatment.

Placement of radiation measuring instruments in the human body cannot be without difficulties and this may, thus hampering precise dose measurements. The focus of this study therefore, is to determine and compare the dose prescribed by the physician with what is actually received during treatment and assessed if the overall error exceed ±5%. The study constructed phantoms to evaluate and verify the actual radiation doses received for breast cancers. Additionally, the advantage of the constructed phantoms is to provide a relatively cheaper phantom for use by universities, research institutions and medical facilities in Ghana. The phantoms were constructed with locally available materials, which makes it cheaper than purchasing a commercial one.

In addition, the study presents modalities for ensuring good quality control and assurance to patients during treatment delivery and addresses the potential errors in dose measurement, calibration of beam output, as well as constancy check of the performance of the radiotherapy equipment.

Limitation

In this study, phantoms and radiochromic film dosimeter were used for the dose assessment for breast irradiation. The study was limited to the use of a standard (anthropomorphic phantom) and constructed phantoms for breast cancer treatment at the radiotherapy facilities in Accra, Ghana during the period of the study. The phantoms used were specific for photon beams only. Electron, proton and heavy ion beams were not considered in this thesis. No attempt was made to simulate the skin layer of the phantom. Polymers and plastics were generally utilized, excluding metals, in the construction of the phantom. The detailed elemental chemical compositions for the various materials that will be used in mimicking various organs (lung, heart and spinal cord) fabricated phantom will not be determined, but it will be assumed that it will not affect the measurements.

Organisation of the Study

The thesis is in chronological order of five chapters. Chapter one is an introduction to the research that provides a general summary on the relevance and justification of the study. It also describes the statement of problem being addressed and the objectives to achieve it. It describes the scope and limitation of the study, and the delimitation is also stated in this chapter.

Chapter Two reviews the literature relevant to the research problem. It includes the interaction of radiation with matter, quantities used in the measurements of photon energy and dosimetry protocols and the technology used. Again, it describes the properties of the phantoms and dose calculation based model used in the study.

Chapter Three focuses on the experimental and theoretical framework for the study. The chapter describes the various measuring procedures that were used to measure and process the data. ImageJ software and Microsoft Excel were used to analyse the experimental data. Monte Carlo software was also used to analyse the theoretical simulation of the study.

The results obtained from the data are presented and discussed in Chapter Four. The chapter describes the relationship between the measureable parameters to calculate the derived quantities in tables and graphical representation. Finally, the analysis of the presented data using the various practical and theoretical tools based on the objectives is also discussed in this chapter.

Chapter Five gives a comprehensive summary of the major findings from the measured parameters. The chapter provides the concluding summary of the study and recommendations to relevant stakeholders.

Chapter Summary

In this chapter, background to the study as well as the problems identified was presented. The objectives of the study were clearly stated to achieve the desired results. Moreover, the scope, limitation and the relevance of the study was explained. Finally, the chapter concludes with a summary on the organization of the research work.

CHAPTER TWO

LITERATURE REVIEW

Introduction

This chapter presents a review of literature relevant to the research problem of whether the planned dose prescribed by the physician is less or more than what the patient receives (delivered dose). It includes the interaction of radiation with matter, quantities used in the measurements of photon energy and dosimetric protocols and practices used in characterizing radiation. In addition, it describes the technology of radiation therapy, and also the properties of the dosimeter used. Dose calculation algorithm on Monte Carlo model is presented. Finally, the ImageJ software used in the calculation of the optical density is discussed.

Photon Interaction Mechanism

Radiation is the energy that is transmitted in the form of both electromagnetic waves and particles (Canadian Nuclear Safety Commission, 2012). Radiation interacts with a material when it passes through by transferring all or some of its energy to the atoms of that material. This interaction could damage the tissue by causing strands breaks in genetic molecules called deoxyribonucleic acid (DNA) in nucleus of living cell. Such damages of the tissue are considered a major cause of cancers, leading to harmful effects on the health of people. Radiation interaction with matter depends on the mass, energy of the beam, as well as on the density and atomic constituents of the absorbing material.

Photons are indirectly ionizing radiation which interact with matter in three principal processes namely photoelectric effect, Compton scattering, and pair production (Diacon, 2015). They undergo a transformative event when interacting with matter that leads to a significant energy transfer to electrons. This transfer impacts energy to matter, where radiation dose is deposited (Thapa, 2013). The relative importance of each of the interactions is mostly dependent on the incident photon energy (E) and the atomic number (Z) of the absorbing medium. The strength of each of the three principal ways of interactions is shown in Figure 1.

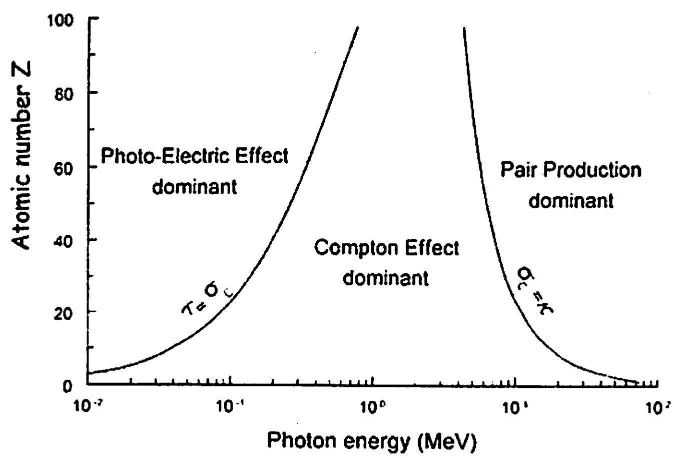

Figure 1: Diagram of energy range of photon interactions with material.
Source: Diacon, 2015

Figure 1 shows the energy range where each type of interaction is most significant. At low energies, the probability of the photoelectric effect increases strongly with Z of the material, depending on Z^4 to Z^5. The effect is much less likely to occur as the energy of the photon increases (Knoll, 1989). At intermediate energies and low Z materials, Compton scattering dominates and it is inversely proportional to energy (Gazda & Coia, 2004). The Compton effect is also dependent on Z but is less dependent on photon energy than the photoelectric effect. In the diagnostic energy range used in medical applications, Compton scattering predominates over photoelectric absorption in most human tissues (Webber, 1987). Pair production is the most dominant interaction process at very high energies.

Pair production is an interaction where the photon loses all its energy and an electron (e^-) – positron (e^+) pair is produced with a threshold energy of 1.02 MeV, and the rest mass energy of the electron is equivalent to 0.51 MeV. The kinetic energy available for the electron-positron pair is the difference between the incident photon energy and the threshold energy for pair production given as:

$$E_{e^-} + E_{e^+} = h\nu - 1.02 \text{ (MeV)} \quad (1)$$

The pair produced in the interaction has significant range and is responsible for the ionization, and therefore responsible for the associated biological damage that occurs at a high energy used in radiotherapy. Table 2, shows some characteristics of the three (3) main processes of photon interaction with matter.

Table 2: Characteristics of Photoelectric Effect, Compton Effect and Pair Production

Factors	Photoelectric Effect	Compton Effect	Pair Production
Photon interaction	Whole atom (bound electron)	Free electron	Nuclear Coulomb field
Mode of photon interaction	Photon disappears	Photon scattered	Photon disappears
Energy dependence	$(h\nu)^3$	Decrease with energy	Increase with energy
Threshold	No	No	$2m_oc^2$
Linear attenuation coefficient	τ	σ_c	κ
Particles released	Photoelectron	Compton (recoil) electron	Electron-positron pair
Atomic coefficient dependence on Z	$\tau \propto Z^4$	$\sigma_c \propto Z$	$\kappa \propto Z$

Source: Podgorsak, 2005

In the study, Compton scattering and pair production interactions were applicable because of their energy ranges in medical applications of diagnostic and therapy respectively.

Radiation Dosimetry

Photon dosimetry deals with the quantitative determination methods directly or indirectly of the amount of energy deposited in a given medium. Investigations and measurements of radiation effects require the respective radiation field at the point of interest (Seutjens et al., 2003). The two closely related fundamental quantities needed to define the radiation beam are kinetic energy released per unit mass (KERMA) and absorbed dose.

Kinetic Energy Released per Unit Mass is a non-stochastic quantity applicable to indirectly ionizing radiations such as photons and neutrons. It is defined as the mean energy transferred from the indirectly ionizing radiation to charged particles (electrons) in the medium dE_{tr} per unit mass dm:

$$K = \frac{dE_{tr}}{dm} \tag{2}$$

The energy of the photons is imparted to matter in two stages. Firstly, the photon radiation transfers energy to the secondary charged particles through the various photon interactions. Secondly, the charged particle transfers energy to the medium through atomic excitations and ionizations as shown in Figure 2.

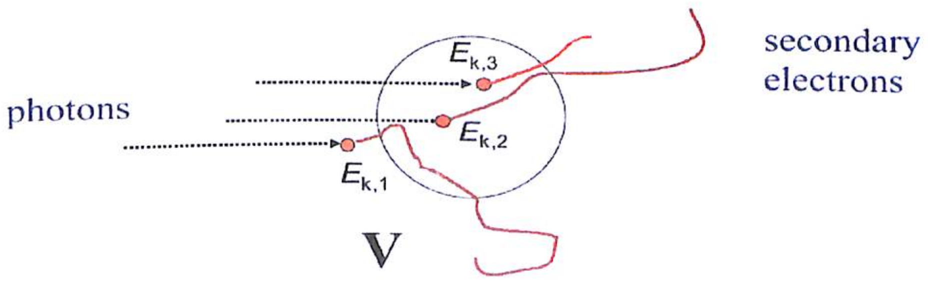

Figure 2: Photon radiation transfers energy to charged particles through the medium.

Source: Hartmann, 2015

The collision energy transferred within the volume is:

$$E_{tr} = E_{k,2} + E_{k,3} \tag{3}$$

where E_k is the initial kinetic energy of the secondary electrons. $E_{k,1}$ is transferred outside the volume and therefore is it not accounted for in the definition. $E_{k,2}$ and $E_{k,3}$ are the energies absorbed inside the volume.

For mono-energetic photons:

$$K = \Phi E \, \mu_{en}/\rho \tag{4}$$

where Φ is the particle fluence; E is the energy; μ_{tr}/ρ, mass energy transfer coefficient.

Absorbed dose is a non-stochastic quantity that is applicable to indirectly and directly ionizing radiations. For indirectly ionizing radiations, the energy is transferred as kinetic energy to secondary charged particles. The charged particles therefore transfer some of their kinetic energy to the medium and lose some of their energy in the form of radioactive loses. The absorbed dose, D, is defined as the mean energy ε imparted by ionizing radiation to matter of mass, m, in a finite volume V by:

$$\mathrm{D} = \frac{\mathrm{d}\varepsilon}{\mathrm{dm}} \tag{5}$$

The energy imparted ε is the sum of all the energy entering the volume of interest minus all the energy leaving the volume, taking into account any mass-energy conversion within the volume. Electrons travel in the medium and deposit energy along their tracks and this absorption of energy does not take place at the same location as the transfer of energy described by KERMA.

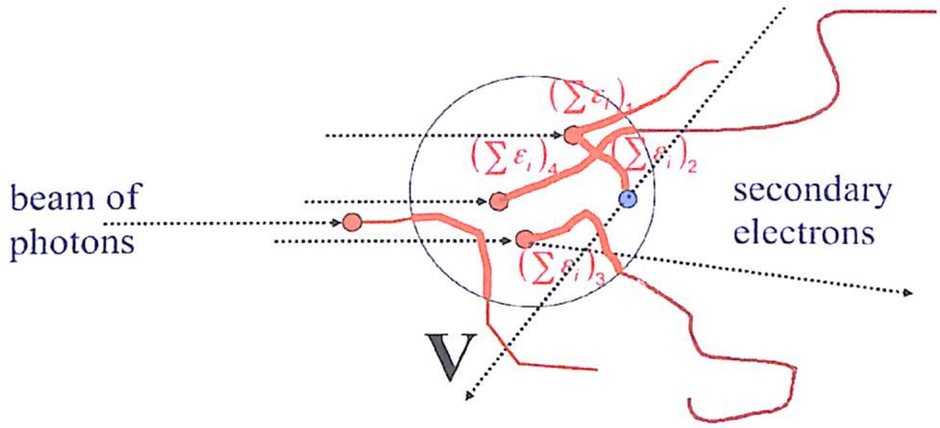

Figure 3: Absorbed energy and dose process within a given volume of matter.
Source: Hartmann, 2015

The energy absorbed in the volume is given by $(\sum \varepsilon_i)$ as:

$$(\varepsilon_i)_1 + (\varepsilon_i)_2 + (\varepsilon_i)_3 + (\varepsilon_i)_4 \tag{6}$$

$(\sum \varepsilon_i)$ is the sum of energy lost by collision along the track of the secondary particles within the volume V.

For mono-energetic X-rays and gamma radiation yields:

$$D = \Phi E\, \mu_{en}/\rho \tag{7}$$

where Φ (m^{-2}) is the photon fluence; E is the photon energy (J); μ_{en}/ρ $(m^2 kg^{-1})$ is the mass energy absorption coefficient.

Phantom

Phantoms are physical or virtual representations of the human body to be used for the determination of absorbed dose to radiosensitive organs and tissues. Phantoms are composed mainly of tissue mimicking materials. It comes in a wide variety of shapes and sizes that mimic the radiological properties of patients. In radiation protection a widely used physical model is the Alderson Rando Anthropomorphic phantom (Alderson et al., 1962; ICRP, 1991), which consists of a human skeleton embedded in tissue-equivalent material, which has the shape of a human body.

Lanzl (1995) studies showed a tissue equivalent female anthropomorphic Rando phantom with height 163 cm and weight 54 kg based on reference values from the International Commission on Radiation Protection [ICRP]. The female anthropomorphic phantom is made up of material density of 0.985 g/cm^3±1.25% and an effective atomic number of 7.30±0.5%. According to the International Commission on Radiation Protection and Measurement Standard Man, the lungs are rigid and moulded into an air-expanded version of the soft tissue material, with the same atomic number and density of 0.3g/cm^3. The right lung is bigger than the left to make room for the heart on the left. The anthropomorphic phantom is sliced transversely with each section of being 2.5 cm thick (Lanzl, 1995). It also has a detachable breast. Figure 4 shows a picture of the Rando phantom.

Figure 4: Picture of Rando (female) anthropomorphic phantom sectioned transversely for dosimetric studies.

Source: Field Survey, 2018

Radiation dose distribution data are generated from water phantom measurements, which closely approximates the radiation absorption and scattering properties of muscle and other soft tissues. The choice of water as a phantom material is that it is universally available with reproducible radiation properties and also a classic tissue equivalent material. However, water phantom presents some practical problems when used in conjunction with ion chambers and other detectors that are affected by water, unless they are designed to be waterproof. Yet, it is not always possible to put radiation detectors in water in most cases. Therefore, solid dry phantoms are developed as substitutes for water.

Ideally, for a given material to be tissue or water equivalent, it must have the same effective atomic number, number of electrons per gram, and mass density. However, since the Compton effect is the most predominant mode of interaction for megavoltage photon beams in the clinical range, the necessary condition for water equivalence for such beams is the same electron density (number of electrons per cubic centimetre) as that of water (Khan, 2009). Other materials for phantoms include agar, glycerine and epoxies to simulate bone. In addition, home based phantoms can be used to test a particular property of the radiation beam by using cheap local materials.

In this study, a tissue equivalent phantom made of perspex which mimics the thoracic part of the female human body was constructed based on the female anthropomorphic phantom and it was used for the absorbed dose measurement. Table 3 shows the physical properties of polystyrene and perspex, with its chemical composition used in the study and other tissue equivalent materials. The polystyrene and perspex used in the phantom construction were evaluated as discussed in chapter three.

Table 3: Physical Properties of various Phantom Materials

Material	Chemical Composition	Mass Density (g/cm^3)	Number of Electrons/g (* 10^{23})	$Z_{eff}^{\#}$
Water	H_2O	1	3.34	7.42
Polystyrene	$(C_8H_8)_n$	1.03 – 1.05	3.24	5.69
Plexiglas (Perspex)	$(C_5O_2H_8)_n$	1.16 – 1.20	3.24	6.48
Polyethylene	$(CH_2)_n$	0.92	3.44	6.16
Paraffin	C_nH_{2n+2}	0.87 – 0.91	3.44	5.42
Solid water	Epoxy resin (based mixture)	1.00	3.34	

where $Z_{eff}^{\#}$ is effective atomic number
Source: Khan, 2003

Breast Composition

It is essential that the constructed breast phantom should depict highly variable human anatomy. The normal female breast consists principally of three tissues, namely, fat, glandular, and the skin. Fibrous and connective tissues are found interspersed throughout the breast, providing shape and structure. Cooper's ligaments are crisscrossing and overlapping bits of fibrous tissue that course between deep and superficial layers of the breast, incompletely compartmentalizing the structures of the breast. They form around and support the variable ductal network of the breast, attaching to the skin with superficial extensions. Fat surrounds and is interspersed throughout the breast by varying amounts (Li Hsu, 2010). The normal breast is shown in Figure 5.

According to Khan (2003), the irradiation of the breast in radiotherapy involves the use of opposed tangential fields (medial and lateral) which travel obliquely across the thorax on the side of the affected breast, encompassing the entire ipsilateral breast and the smallest possible volume of lung and heart, inclusion of 1.5 to 2 cm of underlying lung. The fields in the breast treatment is shown in Figure 6.

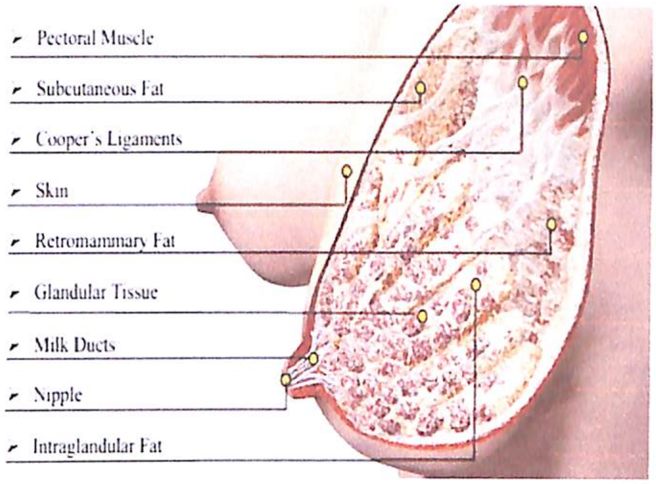

Figure 5: Illustration of the anatomy of the breast.
Source: Medela, 2006

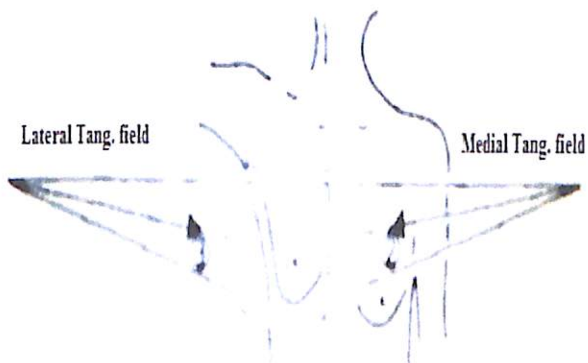

Figure 6: Fields in a breast treatment.
Source: Khan, 2009

Dosimetry Factors

The variation in dose with depth is governed by three effects: inverse square law, exponential attenuation and scattering. The dose to a point located on the central axis of a beam incident on a water phantom varies with the distance from the radiation source, the depth in the phantom and the amount of radiation scattered to the point. Figure 7 shows the geometry of the effect of scatter, depth of attenuation and distance during irradiation.

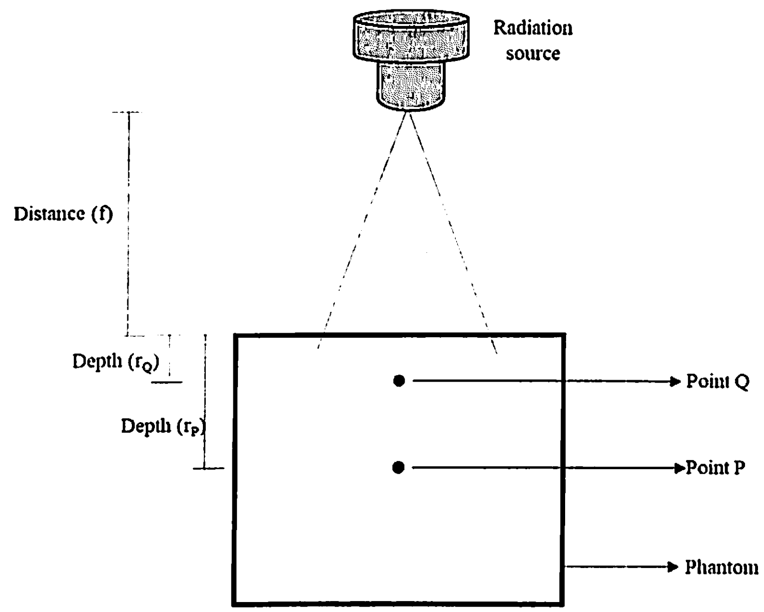

Figure 7: Geometry of distance, depth and scatter.
Source: Adopted from Prado, 2019 and modified

Considering that f is the distance from the source to the surface of the phantom, P and Q are points, dP and dQ are the depths of P and Q respectively, and r_P and r_Q represent the size of the field at P and Q. Therefore, the ratio of the relative doses existing at Q and P can be approximated as a function of $K_s(r)$ that characterizes the effects of scatter as:

$$\left(\frac{D_P}{D_Q}\right) = \left(\frac{K_{s(rP)}}{K_{s(rQ)}}\right)\left(\frac{f+d_Q}{f+d_P}\right)^2 \left(e^{-\mu(d_P-d_Q)}\right) \qquad (8)$$

where $\left(\frac{K_{s(rP)}}{K_{s(rQ)}}\right)$ is scatter, $\left(\frac{f+d_Q}{f+d_P}\right)^2$ is distance and $\left(e^{-\mu(d_P-d_Q)}\right)$ represent the exponential attenuation of the depth, μ is linear attenuation coefficient and K_s accounts for the change in scattered dose.

The radiation intensity is inversely proportional to the square of the distance from the source. Scattered radiation is a significant contributor to the dose at any point. The amount of scatter is related to the amount (volume) of scattering material. Scattering volume is defined by the effective size of the radiation field. The effective field describes the dosimetry of the scatter properties characteristics of the field. Dosimetric quantities are measured by rectangular or specifically square fields. Rectangular fields are approximated by square fields having equivalent attenuation and scattering characteristics. The side, a of the equivalent square of a rectangular field, L and width W can be approximated by:

$$a = \left(\frac{2 \, x \, L \, x \, W}{L+W}\right) \tag{9}$$

This study used a square field size of $10 \, x \, 10$ for the dosimetric phantom measurements. The absorbed dose in the phantom varies with depth. Percentage depth dose (PDD) is used to characterize the variation. Figure 8 gives the illustration of the percentage depth dose.

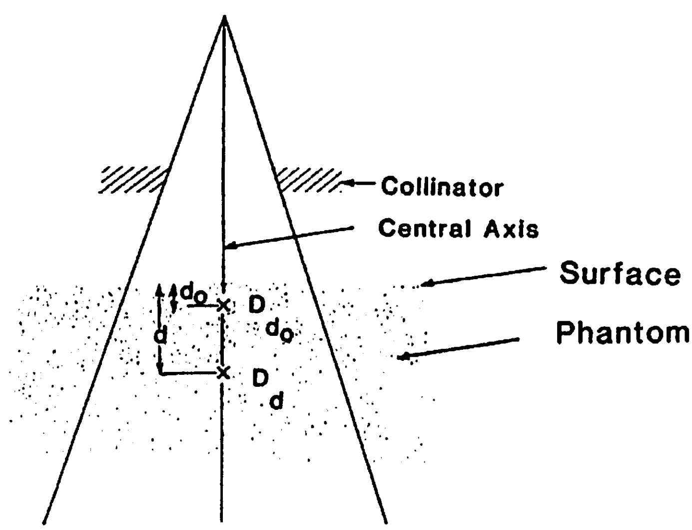

Figure 8: Illustration of percentage depth dose.
Source: Khan, 2009

$$PDD = (D_d/D_{do}) * 100 \tag{10}$$

where D_d is any depth and D_{do} is the reference depth of maximum dose. The PDD is used for fixed source-to-surface distance (SSD) treatments in most situations. The PDD is dependent upon the beam quality or energy, the depth, the field size and the source to surface distance.

Dosimetry Protocols

Absorbed dose to water is the quantity that closely relates to the biological effects of radiation. The recommended protocols used for the determination of absorbed dose to water for high energy photon radiotherapy beams is the code of practice of the International Atomic Energy Agency [IAEA] TRS 398 (Technical Report Series) and American Association of Physicists in Medicine [AAPM] Task Group TG-51. The protocols are based on very simple physics implementation and there is no need of calculating any theoretical dosimetry factors (Roger, 2018). It is emphasized that the formalisms of the protocols have very similar uncertainties when the same criteria are used for both procedures. The difference between the two protocols in the absolute dose is either due to a close similarity in basic data or to a fortuitous cancellation of the discrepancies in data and type of chamber calibration. In the study, the TRS-398 protocol was employed for the radiotherapy dosimetry and this was based on standards of absorbed dose to water (as shown in Appendix A).

Dosimetric Verification

Dose distributions are verified with treatment plans generated with computer applications. The verification is conducted by placing detectors in a patient (phantom). Therefore, an indirect dosimetric verification method is adopted by irradiating a phantom and comparing the resultant dose distribution in the phantom to the distribution calculated by the TPS for that particular phantom (Jursinic & Nelms, 2003). The choice of the dose measurement tools such as ion chambers, thermoluminescent dosimeters (TLDs), diodes and radiographic film forms an important part to the dosimetric verification. According to Duggan and Coffey (1998), ion chambers are standard handheld survey instruments in radiotherapy for point measurements of radiation dose, consisting of a gas filled enclosure between two conducting electrodes (Podgorsak, 2005). This instrument has a relatively low applied voltage from anode to cathode; as a result, there is no avalanche effect and no dead time problem. Ionization chambers typically are useful at exposure rates ranging from 0.1 mR to 100 R. An ionization chamber was used as a dose calibrator for this study. Radiographic films are also used to verify the dose in radiotherapy treatment. In this study both ion chamber and radiochromic films were used for the dose verification.

Dosimeter Characteristics

A detector used for dose verification must be accurately calibrated to measure and determine the doses from exposure. Calibration determines the absolute dose in *Gy* at one reference point in the beam. Calibration can be performed either; by ionization chamber only or by both the ionization chamber and electrometer. In this study, absorbed dose to water calibration using the IAEA TRS398 protocol was performed using a water phantom.

Again, the most important feature of any dosimeter is its ability to correctly measure the dose. The precision of a dosimeter measurement can be estimated from the data obtained in repeated measurements, and is usually stated in terms of the standard deviation. High precision is associated with a small standard deviation (Izewska & Rajan, 2005). Also, the accuracy of a dosimeter measurement is the proximity of their expectation value to the true value of the quantity being measured (Attix, 1986). It is therefore, impossible to evaluate the accuracy of data from the data itself, as is done to assess their precision. Accuracy is a measure of the collective effect of the errors in all the parameters that influence the measurements. It depends on the type of radiation being measured.

Several studies have formulated the accuracy in the delivery of absorbed dose during radiotherapy. Based on a review of the relative steepness of dose - response curves for local tumour control and normal tissue damage, a combined uncertainty of 5% (ICRU, 1976), 3.5% (Mijnheer et al., 1987), 3% (Brahme et al., 1988) was proposed in dose delivery. Considering the complexity of the dose delivery process, it is difficult to achieve 3% or 3.5% accuracy in practice (Dutriex, 1984) and it is common to refer to the ICRU 24 recommended (Ahnesjö & Aspradakis, 1999). Therefore, the overall accuracy level of 5% as the correction action level as recommended by ICRU 24 is referred to on the dose given to the patient at the end of all steps in dose delivery.

Moreover, the uncertainties in this study were evaluated as a standard deviation relative to the measurements. It is a statistical method that describes the dispersion of the measured values of a quantity, and it is assumed to be symmetrical. If a measurement of x quantity is repeated N times, the mean value ($\bar{x}$) for all measurements x_i is given as:

$$\bar{x} = \frac{1}{N}\sum_{i=1}^{N} x_i \tag{11}$$

The standard deviation, σ_x characterizes the average uncertainty for an individual result x_i and is given as:

$$\sigma_x = \sqrt{\frac{1}{N-1}\sum_{i=1}^{N}(x_i - \bar{x})^2} \tag{12}$$

$$\sigma_{\bar{x}} = \frac{1}{\sqrt{N}}\sigma_x = \sqrt{\frac{1}{N(N-1)}\sum_{i=1}^{N}(x_i - \overline{x})^2} \tag{13}$$

Equation (13) represents the standard deviation of the mean value. The uncertainty can be reduced by increasing the number of measurements. In therapy, the overall desired uncertainty is 3% and 95% confidence level is required.

Radiochromic Film

Radiochromic film which is a relative dosimeter was used to determine the absorbed dose to the various organs (lungs and heart) within the breast in this study. The film experiences a permanent colour change when irradiated, which is the result of a spectrally dependent change in optical density an advantage over standard radiographic film. GafChromic external beam therapy (EBT) film, is the first type of radiochromic film suitable for dose verification in radiation therapy since 2004. The International Specialty Products (ISP, Wayne, NJ) released a new film generation, EBT3 film (Borca et al., 2013) as the most recent radiochromic film for applications in clinical dosimetry for external beam therapy.

It is a colourless film with a nearly tissue equivalent composition (H- 9.0%, C- 60.6%, N- 11.2%, O- 19.2%) that develops a blue colour upon radiation exposure. The film contains a special dye that is polymerized upon exposure to radiation. The polymer absorbs light and the transmission of light through the film could be measured with a suitable densitometer. Radiochromic film is self-developing, needs neither developer nor fixer and it also has a very high resolution used in high dose gradient regions for dosimetry (Izewska & Rajan, 2005). It covers a wide dosimetric range from doses as low as 0.1 up to

10 Gy (Butson et al., 2003).

The most important EBT3 characteristics investigated, is its response at high dose levels, sensitivity to scanner orientation and post-irradiation colouration, energy and dose rate dependence, and orientation dependence with respect to film side. EBT3 exhibits highest sensitivity (higher absorbance) at 636 nm; therefore, if the film is scanned for dose evaluation, the maximum sensitivity is obtained by using the red channel. According to the manufacturer, the red channel is recommended for dose evaluations up to 8 Gy, while the green channel can be used for doses from 8 to 40 Gy. The blue channel provides a response signal to automatically correct for the non-uniformity of the film by incorporating a special marker dye in the active layer of the EBT3 films.

The principal concern with using film as a dosimeter is the fragility of the relationship between dose and optical density. This relationship can also be expressed as the sensitivity of the film to dose. It is possible to achieve the precision better than 3%, if proper care is taken of its calibration and with the environmental conditions. In this study, the EBT3 GafChromic film was used for dose verifications due to its excellent spatial resolution, extended dose response and self-developing features.

Optical Density Spectrum

Optical density is used to describe the darkness of a transparency film. The radiochromic film, when exposed to ionizing radiation, colouration occurs. This colouration is due to an attenuation of some of the visible light coming through the developed film, resulting in a 'greying' of its appearance. The reduction in light passing through the film is a measure of its 'blackness' or 'optical density' (OD). The dose to the film is reflected in the resulting optical density of that film and this relationship can be expressed as:

$$OD = log_{10}\left(\frac{I_0}{I}\right) \tag{14}$$

where I_0 is the light intensity with no film present and I is the light intensity transmitted through the film. Optical density is appropriately linear with dose since $^{I_0}/_{I}$ has an exponential relationship to the dose. The advantages offered by the film to other dosimeters include the mapping ability whereby an area of dose can be analyzed as compared to a point measurement in most other types of detectors (Butson et al., 2003). Equation (14) was used to calculate the pixel values of the film dosimeters used.

Film Characteristic Curve

Film is an image converter which converts radiation, typically light, into various shades of gray or optical density values. An important characteristic of film is that it records, or retains, an image. The amount of exposure required to produce an image depends on the sensitivity, or speed of the film being used. A film with a high sensitivity requires less exposure than a film with a lower sensitivity. The film's photo-sensitive layer is composed of three dyes that respond to three different light spectrums. These curves show the spectral sensitivity of each of these dyes across the visible light spectrum (390-700 nm). The colour response curves of colour film emulsions are not linear across colour channels and the response curve anomalies of each emulsion are idiosyncratic.

Film characteristic curves are used to relate the film exposure to the resultant optical density where the exposure refers to the amount of photons that reach the film and is dependent upon the intensity of the radiation and the time that the film is exposed (NDT Resource Center, 2001-2014). The characteristic curve is also referred to as the H&D curve, named after Hurter and Driffield who developed it in 1890. A plot of optical density (OD) versus log exposure yields a characteristic S-curve for each type of film to determine its sensitivity with three regions of importance: the toe, gradient, and shoulder as shown in Figure 9. Change in the exposure will move along the curve, helping to determine what exposure is needed for a given film.

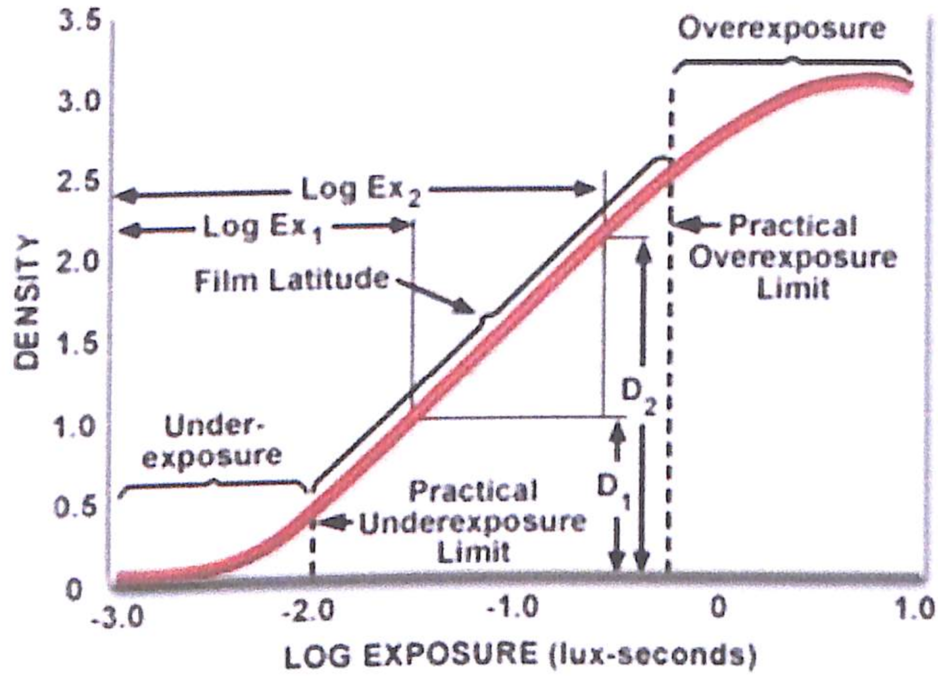

Figure 9: Characteristic curve of film density versus log exposure.
Source: Davidson, 1998

However, in terms of radiation dosimetry, the dose versus optical density is most commonly used and is referred to as the sensitometric curve. In this case, the OD is a function of radiation dose, dose rate, energy, type of primary radiation, depth of measurement, field size, and processor conditions (Durham, 2015). In Figure 9, the film used for the study was in the overexposure range since it was being used in therapy dose assessment of higher doses. Figure 10 shows the various types of plots for film response.

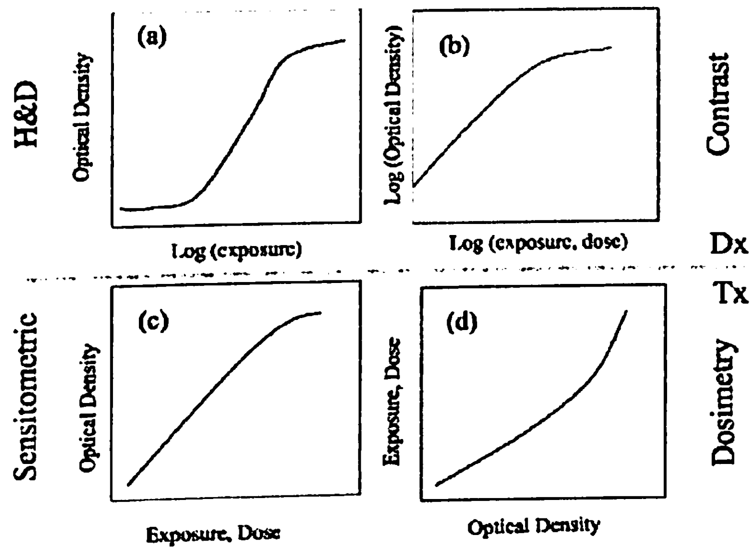

Figure 10: Plots of film response curves of optical density versus log exposure: (a) H&D curve; (b) H&D curve with contrast; (c) Sensitometric; (d) Dosimetry.

Source: Pai et al., 2007

Figure 10 shows the different representation of the film response and radiation dose. The upper panel (a) and (b) is used in diagnostic radiology while the lower panel (c) and (d) are useful in radiotherapy. The H&D curve is the film response curve of a film where the log exposure is plotted on the x -axis and the optical density on the y-axis. H&D curves are important for quantifying contrast and dynamic range of a radiographic film. The characteristics of film response could be plotted in various ways such as dose versus optical density (OD), log (dose) versus OD, or log (dose) versus log (OD) as shown in Figure 10. There are advantages to each of these plots, but in radiation oncology the dose versus OD is most often used and called the sensitometric curve (Pai et al., 2007). In the study plot (c) and (d) from Figure 10 is expected for the relationship between the optical density and dose for the sensitometric curves and dosimetry measurement respectively.

Photon Dose Algorithm

In radiation therapy, the dose to be delivered to patients needs to be determined before the treatment. Therefore, it is necessary to have an accurate method for predicting the dose distribution. In the past, planning computers were used to calculate the radiation dose using data obtained by measurement in a water phantom, and this leads to about 3% to 10% error in the situations where inhomogeneity and lateral electron disequilibrium occur, especially in small field sizes (Jones & Das, 2005). Clinically, Monte Carlo (MC) simulation was proposed to give the most accurate solution and it was used to model the dose distribution in a medium by simulating the photon transport (Rogers et al., 1995; Verhaegen & Seuntjens, 2003; Andero, 1992; Purdy & Starkschall, 1999). The first available MC code for treatment planning was developed in the early 90s by the National Research Council of Canada and the University of Wisconsin in Madison.

Alternatively, the convolution algorithm was developed for treatment planning since MC technique had a limited application in radiotherapy due its high demands for computing power in the 90's. The convolution algorithm calculates the dose delivered to a volume by convolving the interaction sites with the dose deposition kernel derived from the output spectrum of the linear accelerator. Convolution algorithm has improved dose calculation accuracy but it still has limitation of breaking down when there is a high atomic number material present.

Nowadays, fast computers and variance reduction techniques to speed up the MCS calculation for radiotherapy treatment planning is feasible for use. Monte Carlo takes into account the applicable physical interactions for calculating dose, allowing one to calculate dose even in the regions not well accommodated by other dose algorithms (Sauer, 1995; Yu et al., 1995; Arnfield et al., 2000; Neuenschwander et al., 1995).

The Monte Carlo algorithm samples randomly from known cross sections of photon interactions by simulating the stochastic nature of the photon interactions (Andero, 1991; Mackie et al., 1996). The trajectory of the photon is simulated until the photon leaves the volume of interest or falls below its energy threshold. Firstly, the beam output of the radiotherapy is modelled, and the dose distribution is calculated by using the beam model created. Monte Carlo depends primarily on the correctness of the information about the starting condition of the radiation transport, the materials used and the geometry of the setup. In this study, the Monte Carlo software was used for dose calculations in certain regions of the phantom by simulating the transport of photon and recording the interactions of each particle until it reaches the pre-set threshold energy.

Radiotherapy Technology

Advances in imaging technology in terms of computerized tomography (CT), magnetic resonance imaging (MRI), positron-emission tomography (PET) and fusion PET/CT have improved the accurate targeting of tumours (Vikram, 2009). Fundamentally, the processes of targeting the tumour with maximal sparing of normal tissues and therapy planning have changed as a result of the new developments in advanced technology in computers. The targeted dose is delivered with the help of the teletherapy treatment machines. The treatment machines incorporated gamma ray sources. They are often mounted isocentrically allowing the beam to rotate about the patient at a fixed source-to-axis-distance (SAD) of 80 cm or 100 cm. The primary part of the external beam therapy machine used are, a radioactive source, a source housing, gantry, patient support assembly and console (Podgorsak, 2005). In this study CT, Co-60 and linear accelerator were used in the planning of the target tumour and delivery of radiation doses.

Cobalt Teletherapy Machine

Cobalt-60 isotope is used widely for external beam radiotherapy, considering the energy of emitted photons, half-life, specific activity and means of production. The source activity a_c is inversely proportional to the half-life, $t_{1/2}$ as:

$$a_c = \frac{A}{m} = \frac{N_A ln2}{t_{1/2}A} \tag{15}$$

where A is the atomic mass number, m is the mass of the radioactive nuclide and N_A is the Avagadro's number. The Co-60 source used decays over time with a half-life of 5.26 years with a mean energy of 1.25 MeV. It emits two gamma radiation of 1.17 MeV and 1.33 MeV. It disintegrates by beta minus emissions to excited levels of Ni-60 (as shown in Figure 11).

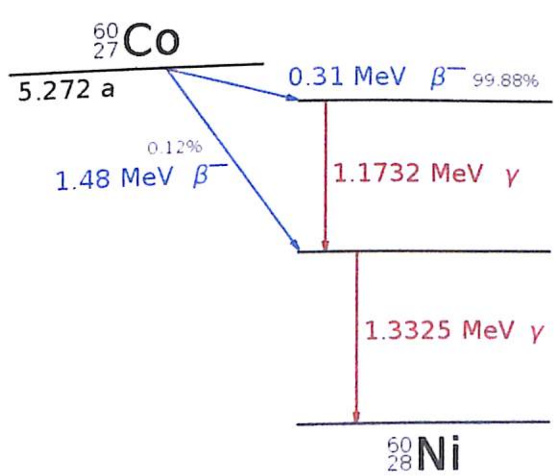

Figure 11: Decay scheme of Co-60.
Source: Lieser, 1991; Helmer, 2006

The γ-rays constitute the beam absorbed in the cobalt source or the source capsule, where they produce relatively low energy and essentially negligible bremsstrahlung X-rays and characteristic X-rays. The relatively high penetrability of Co-60 makes it a good isotope for teletherapy. Like the higher energy X-ray beam from a linear accelerator, there is also a skin sparing benefit with Co-60 treatment; the maximum dose is beneath the skin surface.

In this work, the Theratron Equinox 100 Co-60 manufactured by Best Theratronics with a 1.25 MeV nominal photon energy was used. The source activity within the treatment head of the teletherapy machine at the time of the study was 399.0 TBq. Figure 12 shows a picture of the Cobalt treatment machine.

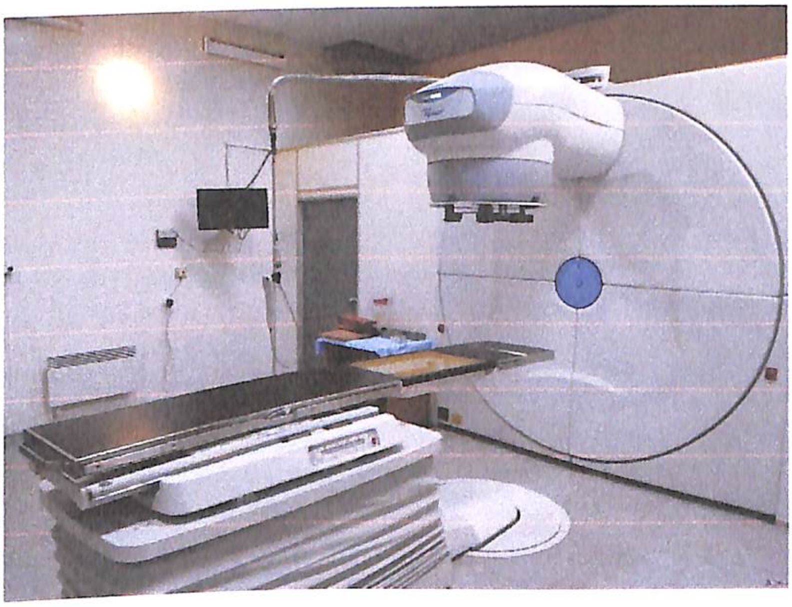

Figure 12: Theratron equinox 100 Co-60 machine at National Centre of Radiotherapy and Nuclear Medicine, Korle-Bu, Accra, Ghana.

Source: Fieldwork, 2018

Linear Accelerator

Linear accelerators (LINAC) are external beam radiotherapy machines that use high frequency electromagnetic waves in the frequency range from 103 MHz to 104 MHz to accelerate electrons to kinetic energies from 4 to 25 MeV.

The electrons are accelerated following straight trajectories in accelerating waveguides, the evacuated structures in a high power radiofrequency fields produced through the process of decelerating electrons in retarding potentials in special evacuated devices. A removable target is used to produce high-energy X-ray photons for photon radiation where the electrons can be scattered using an electron scattering foil.

Electron gun and X-ray target form part of the accelerating waveguide and are aligned directly with the accelerator isocenter, preclusive the need for a beam transport system. A photon beam is produced and the RF power source is mounted in the gantry. The beam traverses two independent ionization chambers that constantly monitor the beam output and shut down the accelerator if discrepancies are detected. The ionization chambers are used to measure the monitor units (MU) of the linear accelerator (Greene & Williams, 1997; Metcalfe et al., 1997; Podgorsak, 2005). A schematic diagram of a typical linear accelerator is shown in Figure 13.

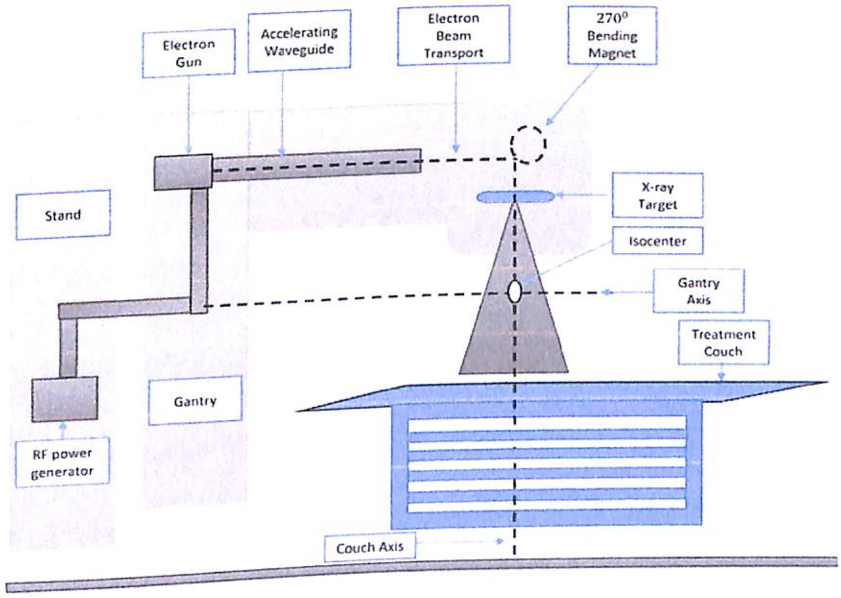

Figure 13: Schematic diagram of a typical linear accelerator.
Source: Saeed (2015)

Linear accelerators are available for clinical use in various types with some providing X-rays only in the low MeV range and others providing both X-ray and electrons at various MV energies. A typical modern high energy accelerator provides two photon energies and several electron energies. There is an increased flexibility with linear accelerator where lower energy electrons can be used to treat superficial skin tumours and higher energy X-rays used to treat deeper tumours with a lower dose to the skin (Forrest, 2003).

In this study, the linear accelerator treatment unit, manufactured by Elekta Synergy 11 platform, with a 6 MV and 15 MV nominal photon energy was used. Figure 14 shows a picture of the linear accelerator used for the study.

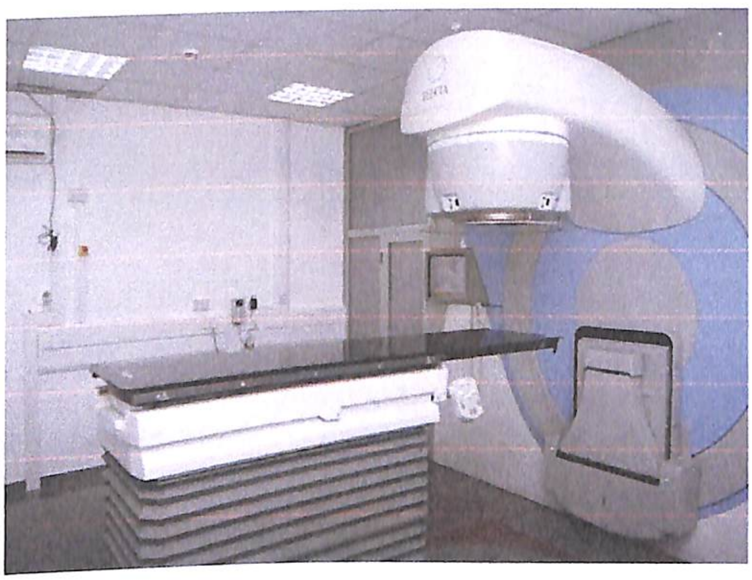

Figure 14: Elekta synergy linear accelerator machine at Sweden Ghana Medical Centre, Accra, Ghana.

Source: Fieldwork, 2018

Computed Tomography

The use of computerized tomography (CT) introduced in clinics in 1971, for a wide range of applications and for radiotherapy planning has increased the accuracy both for geometric volume definitions (Goiten 1982; Dobbs et al., 1983) and for dose calculations. Image-based treatment planning has become the standard for external beam radiotherapy. Patient data for treatment planning need to be acquired from a computed tomography (CT) scanner. The data is transferred into the treatment planning system (TPS) for contouring and treatment. The CT image acquisition process involves the measurement of X-ray transmission profiles through a patient for a large number of views by using a detector, generally consisting of 800–900 detector elements referred to as a detector row. Figure 15 shows the acquired transmission profiles to reconstruct the CT image, composed of a matrix of picture elements (pixels).

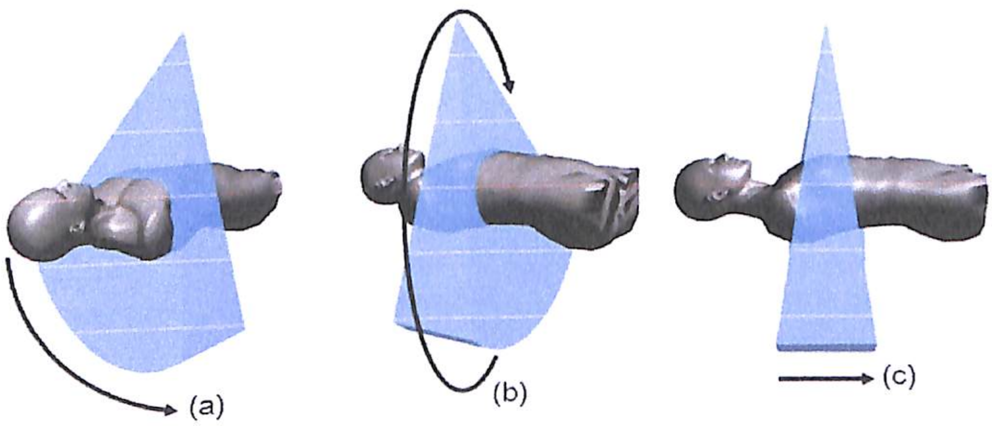

Figure 15: CT image acquisition showing the transmission of x-rays through the patient by using (a) detector row, (b) with rotation of the X-ray tube and detector and (c) by multiple detector.

Source: Dance et al., 2014

The values that are assigned to the pixels in a CT image are associated with the attenuation of the corresponding tissue, or, linear attenuation coefficient $\mu(m^{-1})$. The linear attenuation coefficient depends on the composition of the material, the density of the material and the photon energy, as seen in Lambert beer's law:

$$I(x) = I_0 e^{-\mu x} \tag{16}$$

where $I(x)$ is the intensity of the attenuated X-ray beam, I_0 is the unattenuated

X-ray beam and x is the thickness of the material. Image reconstruction techniques can then be applied to derive the matrix of linear attenuation coefficients, which is the basis of the CT image.

CT scanners use CT numbers (in Hounsfield Units) to account for tissue inhomogeneities within the human body, which are different from the parameters required by the TPS. This enables the dose computation algorithm of the TPS account for tissue heterogeneities in the dose computation process by reading the CT images of the pixels.

Computed Tomography Numbers

The dimensions of the X-ray attenuation quantifier are the CT number. The unit measure for the radio-density or the X-ray attenuation quantifier of the substance scanned is known as the CT number (Hounsfield Unit named after Sir Godfrey Hounsfield). Hounsfield Units is obtained from a linear transformation of the measured attenuation coefficient based on the arbitrary definitions of air and water at standard temperature and pressure. Each pixel is assigned HU scale of tissue density value between -1000 for air and 0 for water.

In the CT image, the matrix of reconstructed linear attenuation coefficients (μ_{tissue}) is transformed into a corresponding matrix of HU, where HU scale is expressed relative to the linear attenuation coefficient of water at room temperature μ_{water}. The linear attenuation coefficients (μ) are dependent on the electron density and the elemental composition. The relation between HU and the linear attenuation coefficient for monoenergetic X-rays of 73 keV and water equivalent tissues (Knöös, 1991) is calculated as:

$$\mu_{tissue} = \mu_{water}\left(1 + \frac{HU}{1000}\right) \tag{17}$$

The range of the Hounsfield Unit for the tissues attenuation coefficient is displayed in the CT window settings for the body part being imaged. Additionally, CT numbers have also been found to be dependent on the individual CT scanner parameters such as kilovoltage peak (kVp) / filtration and reconstruction algorithm (Cheng et al., 2005; Ebert et al., 2008). Table 4 gives the Hounsfield Unit of some tissues and matters in the body.

Table 4: Typical Values and Ranges for Different Tissues and Materials

Substance	Hounsfield Unit
Compact Bone	+1000 (+300 to +2500)
Liver	+60 (+50 to +70)
Blood	+55 (+50 to +60)
Kidneys	+30 (+20 to +40)
Muscle	+25 (+10 to +40)
Brain, Grey Matter	+35 (+30 to +40)
Brain, White Matter	+25 (+20 to +30)
Water	0
Fat	-90 (-100 to -80)
Lungs	-750 (-950 to -600)
Air	-1000

Source: Dance et al., 2014

Table 4 was used to compare values of the HU, which is proportional to the X-ray attenuation of the tissues used in the study. The HU of the CT scan is significant in the pre-assessment evaluation of the tissues before treatments. Therefore, the relationship between the CT numbers and densities in each voxel of the CT images were determined. In view of this, the phantoms were scanned with scan parameters used for scanning patients based on anatomic site.

Electron Density Characterization

In the area of radiotherapy research, there is the need for a fast and reliable technique to quantitatively characterize samples for electron density (Sarapata, 2014). The radiological properties, that is, the electron density of tissue substitutes should be known to a high degree of accuracy (Claude et al., 2013). Thus, the electron density, ρ_Q of a material may be computed from its mass density, ρ_m and its atomic composition according to the formula (Khan, 2003):

$$\rho_Q = \rho_m . N_A . \frac{Z}{A} \tag{18}$$

where

$$\left(\frac{Z}{A}\right) = \sum_i a_i \left(\frac{Z_i}{A_i}\right) \tag{19}$$

N_A is the avogadro's number, a_i is the fraction weight of a constituent element of the material of atomic number Z_i and atomic weight A_i.

Again, the electron density could be obtained from the interaction per unit path length (or linear attenuation coefficient) for a clinical beam in a medium. This is directly proportional to the electron density of the medium through which the clinical beam traverses provided beam hardening and softening effect are minimized (Watanabe, 1999; Khan, 2003). The equation is as follows:

$$\mu = k\rho_Q \tag{20}$$

$$\mu_w = k\rho_{Q,water} \tag{21}$$

where μ and μ_w are the linear attenuation coefficients of a material and water respectively measured using the same clinical beam energy and irradiation geometry, ρ_Q and $\rho_{Q,water}$ are the electron densities of the material and water respectively and k is the proportionality constant. Therefore, from equations (20) and (21), the electron densities of the materials could be calculated as:

$$\rho_Q = \frac{\mu}{\mu_w} \rho_{Q,water} \tag{22}$$

Finally, the electron density can be determined from the CT numbers, which is linked to the tissues found in the human body with radiological properties of water or bone. For soft water like tissues with low atomic number (Z), such that the CT number (in HU), N_{CT} of the tissue is less than 100, the relative electron density was found to be (Thomas, 1999; Battista et al., 1980):

$$\rho_Q = 1.0 + (0.001 \times N_{CT}) \tag{23}$$

For bone like tissues with higher Z values such that N_{CT} is greater than 100, the relative electron density is estimated as:

$$\rho_Q = 1.052 + (0.00048 \times N_{CT}) \tag{24}$$

Therefore,

$$\rho_Q = \frac{\rho_Q}{\rho_{Q,water}} \tag{25}$$

In this study the electron density used was determined from the CT numbers from the CT scans. This procedure was used because the elemental chemical composition of the material substitutes placed in the phantom was not analysed.

ImageJ Software

ImageJ software was used to analyze the exposed san images of the EBT3 film because of its uniqueness to radiological image processing. ImageJ is a Java image processing program designed and inspired by National Institutes of Health (Schneider et al., 2012) for Macintosh for public domain. It runs as an online applet or a downloadable application, on any computer. It is use d to solve radiological image processing problems (Barboriak et al., 2005). ImageJ displays, edits, analyzes, processes, saves, and prints 8-bit, 16-bit and 32-bit colour images, with pixel size of 612 x 842. It can read many image formats files of TIFF, GIF, JPEG, BMP, DICOM, and FITS. It can calculate area and pixel value statistics of defined user selections and intensity. In the study the area was created using the rectangular selection tools of measure which displays the width and height as well.

Again, ImageJ does geometric transformations and supports standard image processing functions of contrast manipulation, sharpening, smooth ing, edge detection and median filtering. All analysis and processing functions are available at any magnification factor. The program supports any number of windows (images) simultaneously, limited only by available memory (ImageJ, 2018a).

The ImageJ window contains a menu bar, tool bar, and status bar. The measurement of results is displayed in the "Results" window. The toolbar tools are used to select, zoom and scroll the images. The status bar displays the pixel coordinates and values. The colours, which reflect genuine colours in RGB images (24-bit), was used to show multi-channel images (ImageJ, 2018b).

Chapter Summary

In summary, the chapter reviewed the literature relevant to the research problem which included the interaction of radiation of matter, dosimetry protocols in radiotherapy, radiometric dosimeter film (EBT3) and phantoms used in measurement of absorbed doses. The technology and dose algorithm of radiation therapy were also introduced in this chapter. The final review was on the ImageJ software to be used in calculating the doses.

CHAPTER THREE

MATERIALS AND METHODS

Introduction

This chapter provides relevant information on the experimental and theoretical framework of this study. The health facilities, dosimetry equipment and methods used to measure, analyse and model the dose distribution are discussed. The chapter describes the calibration, measurement procedures and dosimeter (EBT3 films) that were used. In addition, it includes a discussion on the quality control of the procedures and protocols used for assessing the performance of the machines that were used for the measurement. Furthermore, the standard phantom (anthropomorphic) used for the validation of the *in vivo* dosimetry is discussed. Phantoms construction (named Adelaide A and B), to mimic the thorax of the body of a female, is also discussed. ImageJ software, Microsoft Excel and Minitab statistical tool, used to analyze the experimental data is presented. Also, Monte Carlo software was used to analyze the theoretical simulation of the dose distribution from a Co-60 source.

Health Facility

The study was carried out at a Radiotherapy Unit of the National Centre for Radiotherapy and Nuclear Medicine (NCRNM), Korle-Bu Teaching Hospital and the Sweden Ghana Medical Centre Limited (SGMC) both located in Accra. The NCRNM facility uses Cobalt-60 treatment machine while SGMC used a linear accelerator for radiation treatment. Table 5 shows the equipment specification for the two facilities. Ethical clearance was sought from the University of Cape Coast Institutional Review Board (UCCIRB).

Table 5: Specification of the Machines used for the Study

Machines	Linear Accelerator	Cobalt
Manufacturer	Elekta AB, Stockholm, Sweden	Best Theratronics, Canada
Model	Synergy 11 Platform	Theratron Equinox 100 Cobalt-60
Source Activity	Photons (x-rays)	399 TBq Photons (γ-rays)
Energies	6 MV & 15 MV	1.25 MeV
Treatment Planning System	Ocentra Masterplan	Prowess Panther

Source: Field Data, 2017

Equipment

The study measured, calculated and assessed the ionizing radiation dose absorbed as a result of the interaction of radiation with matter. Therefore, the delivered dose received was measured by the following equipment. They include Cobalt (^{60}Co) machine, linear accelerator (LINAC), one dimensional (1-D) motorized water phantom, solid plate phantom (slabs), ionization chamber, electrometer, barometers, thermometer, and EBT3 film dosimeter.

Water and Solid Phantoms

Water and solid plate phantoms were employed in the study as part of the dosimetric processes, in accordance with the AAPM TG-51 and IAEA TRS-398 protocols, for photon calibration. The water phantom and solid plate phantom were used for the Co-60 and LINAC treatment units for the photon calibration. The phantoms were of the same dimensions which is 30 cm x 30 cm (standard size), and were made from Perspex (also known as poly methyl methacrylate). The measuring depth of the water phantom was adjusted to 20 mm for its use in cylindrical chambers. On one side of the water phantom is a hole provided by the manufacturer to accommodate 0.6 cm^3 farmer type ionization chamber. On its surface is an opening used for filling the phantom with water for the beam output measurement. The solid plate phantom used consists of pile of plates of thicknesses of 0.5 cm, 1 cm, and 5 cm. Figure 16 shows a picture of the water and solid phantoms. Table 6 shows the specification of the solid phantom.

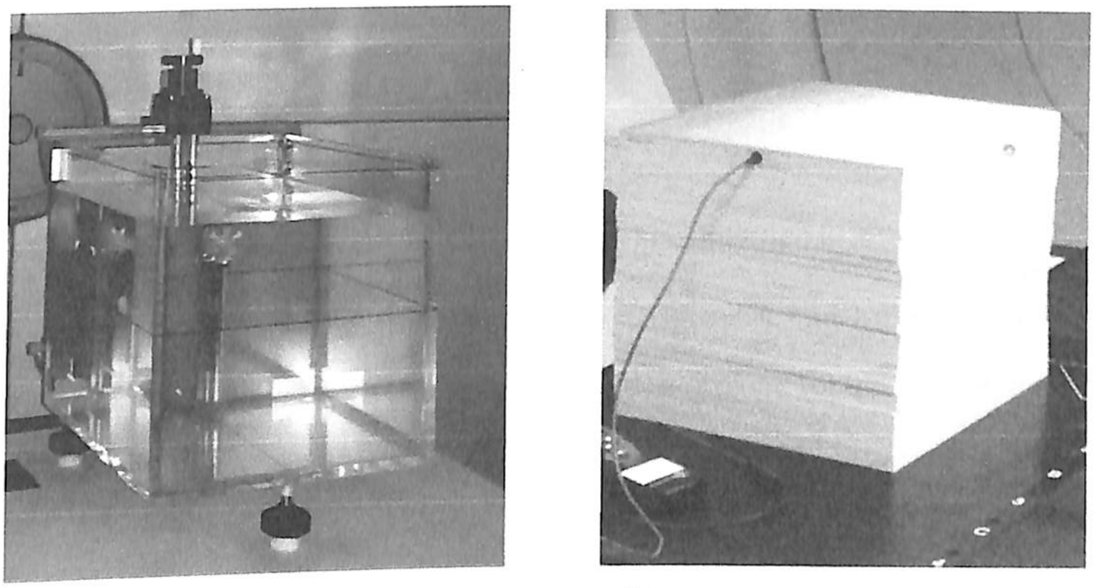

(a) (b)

Figure 16: Phantoms: (a) water phantom filled with water (b) solid plates phantom.

Source: Field Data, 2017

Table 6: Technical Specification of the Solid Phantom used in the Study

Phantoms	Solid Plate
Material	PMMA
Density	1.18 g/cm^3
Measuring depth	18-250 mm (cylindrical chambers)
Adjustment of depth	manually
Energy range	0.1-50 MV, 2-50 MeV
Radiation incidence	Horizontal beam
Exterior dimensions	30 cm (L) X 30 cm (W) x 30 cm (H)

Source: Field Data, 2017

The water phantom was not used with the linear accelerator due to the high electric voltage associated with the linear accelerator making it cumbersome. Therefore, water equivalent solid phantom was available for use with the LINAC. Solid phantoms also eliminate the inconvenience of transporting, setting up and filling water tanks. It scatters and attenuates radiotherapy range X-rays the same way as water without charge storage problems.

Ionization Chamber

The main tool in medical dosimetry is the ionization chamber (Shani, 2001). The ionization chamber used for measurements in the study was the Farmer chamber type, of volume 0.6 cm^3, manufactured by PTW Freiburg, (Germany), and was calibrated at the National Metrology Institute of South Africa. The chamber is water proof. The maximum polarizing voltage used was +400 volt. Table 7 gives the specification of the ion chamber used with the Co-60 and the LINAC beam energies.

Table 7: Ionization Chamber Specifications used in the Study

Type	Famer Type ROOS Chamber 34001
Manufacturer	PTW-Freiburg, Germany
Model	TM30010-1
Serial Number	000821
Detector Calibration Factor, $N_{D,w}$	5.408 x 10^7 Gy/C
Uncertainty	1.1%

Source: Field Data, 2017

The ion chamber was used to detect the individual charged particles created in the water phantom when exposed to the beam energy for therapy. The verification was performed by inserting ion chamber within a tissue equivalent phantom, after which a measurement of the absorbed dose was obtained. The ion chamber was also used in the study to measure the monitor units (MU)

(Greene & Williams, 1997; Metcalfe et al., 1997; Podgorsak, 2005) for the LINAC. Figure 17 shows a picture of the Farmer type ion chamber.

Figure 17: Farmer type ionization chamber.
Source: Field Survey, 2017

Electrometer

The PTW UNIDOS electrometer (model T10021, Freiburg, Germany) with serial number of 000590 was used in the study. The ion chamber and the electrometer were connected together. It is a very sophisticated and accurate measuring device for dose and dose rate measurements in radiation therapy (Elbashir Ali, 2008). The electrometer was used to quantify the charges detected by the ion chamber in units of nanocoulomb (*nC)* in evaluating the absorbed dose to water ($D_{w,5}$). Figure 18 shows a picture of the electrometer used in the study.

Figure 18: PTW UNIDOS electrometer.
Source: Field Survey, 2017

Barometer and Thermometer

A Sensor Type GE Barometer (Druck Pace1000) and an analogue barometer were used with LINAC and cobalt-60 machines respectively. The reference pressure range for the Sensor Type GE Barometer was 99.61 kPa – 101.07 kPa. The temperatures were measured using a thermocouple thermometer (K-Type, Testo 925) for both therapy machines. These measurements were used to to calculate the respective correction factors for each facility.

GafChromic EBT3 Film Dosimeter

The GafChromic EBT3 film (EBT3 film) with product code 828206, from Ashland Speciality Ingredients (NJ, USA) was the dosimeter used in the study. The EBT3 film used has 10 films per box and dimensions of 12.8 x 14.7 inches. The film comprises of a single active layer, nominally 27 μm thick, containing the active component, marker dye, stabilizers and other components giving the film its low energy dependence response. The active layer is in the middle of two, 120 μm transparent polyester component. The EBT3 film's polyester components have a distinct surface treatment containing microscopic silica particles, which maintain a gap between the film surface and the glass window in a flatbed scanner. The active layer incorporates a yellow dye, decreases ultraviolet and light sensitivity that enables multi-channel dosimetry. The recommended protocol for radiometric film dosimetry described by the AAPM TG-55 report 63 (Arjomandy et al., 2010a) was used for the study. Figure 19 shows the configuration of the EBT3 film.

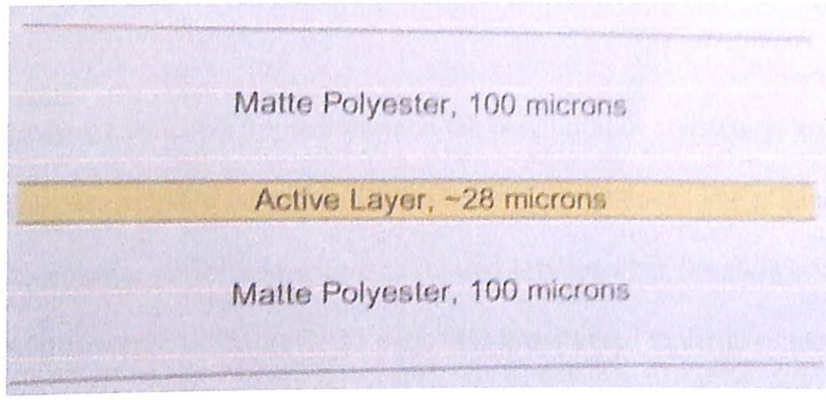

Figure 19: Configuration of EBT3 radiometric film.
Source: GafChromic EBT3 Scan Handling Guide

Performance of Quality Control

Quality Control (QC) on the dosimetry systems were performed, at the facilities of the study, to check the reliability of the operational techniques and equipment used, and to correct the performance of the equipment, if the requirements are not met. The purpose was to verify that the machine characteristics do not deviate significantly from their baseline values, as acquired at the time of their acceptance and commissioning. The quality control tests were performed daily, weekly and monthly as it may be required for the duration of the study. Instrumentation records with respect to calibration certificates and equipment types were recorded for the ionization chamber, electrometer, thermometer and barometer. Safety and mechanical integrity of the LINAC and Cobalt-60 treatment unit were assessed in accordance with the IAEA TRS 398. The quality control checks were classified as dosimetry, mechanical and safety.

Dosimetric Check

The radiation output of the LINAC (1cGy/MU) and Cobalt-60 (1cGy/min) are checked daily, before the first patient is treated. Elekta (2011) recommended that both the LINAC and cobalt machines are warmed up before use. The dosimetric checks performed were on the beam output constancy, and the tolerance was expected to be within ±3% of the reference dose. The photon beam output tests were performed with a calibrated ion chamber (as shown in Figure 17) and a phantom to ensure that 1 cGy/MU is delivered to the isocenter under specific reference conditions. Treatment time of 60 seconds and 100 MU, from dose conversion, were delivered three times by the LINAC and cobalt machines respectively. The beam output constancy was also measured for the LINAC at a depth of 10 cm, and 5 cm for the Cobalt-60 machine at source to surface distance (SSD) of 100 cm. The charged particle readings of the ion chamber were recorded using the electrometer, which is shown in Figure 18. The output factors were normalized to 10 x 10 cm^2 field size at gantry angle of 0 ^{0}. The output in nanocoulomb (nC) was calculated as follows:

$$Output = M_{avg} * K_{T,P} * CF * PCF \quad (26)$$

where M_{avg} is the raw ion chamber readings in coulombs (C), CF is the calibration factor, (K_{Pol}, K_{ele} and K_s) are the collection efficiency factors. The recombination losses were negligible because the chamber polarity was operated near saturation of +400.

The collection efficiency factors could be calculated as:

$$K_{Pol} = \left(\frac{|M_+|+|M_-|}{2M}\right) \quad (27)$$

where M_+ and M_- are the electrometer readings at the voltage $+V_1$ and $-V_1$ respectively, M is the absolute value of M_+ measured in nanocoulomb (nC), K_{ele} is the electrometer calibration factor,

$$K_s = \frac{(V_1/V_2)^2 - 1}{(V_1/V_2)^2 - (M_1/M_2)} \quad (28)$$

where K_s is the recombination correction factor, where V_1 is the normal polarizing voltage and V_2 is the reduced polarizing voltage. $V_1 > V_2$, M_1 and M_2 are the readings at V_1 and V_2 respectively in nanocoulomb.

The temperature and pressure correction factor ($K_{T,P}$) was also calculated based on the formula:

$$K_{T,P} = \left(\frac{273.15+T}{273.15+T_0}\right)\frac{P_0}{P} \tag{29}$$

where P_0 is the reference pressure of value 101.3 kPa and T_0 is the reference temperature of value 20 ^{0}C at reference calibration conditions. T and P are the temperature and pressure readings during the measurement respectively. The phantom correction factor (PCF) was taken as 1.0 for water equivalent phantom.

Mechanical Check

The following mechanical checks were performed on the LINAC and Cobalt-60 treatment units to establish the precision and accuracy of the mechanical motions and the treatment couch. The mechanical check s performed were localizing lasers, treatment couch alignment and verifying optical distance indicator (ODI), gantry/collimator angles, and field sizes.

The localizing lasers were assessed to check that all laser beams were correctly indicated on the isocentre and that the opposing laser beams were congruent. The lateral and sagittal lasers were verified within 1 mm tolerance, Optical distance indicator (ODI) was measured to check that the source-to-surface-distance (SSD) light indicator was same as the mechanical distance. The ODI was measured at several SSD in the range between 80 cm and 100 cm. According to the TG-142 recommendation, the tolerance for ODI is 1 mm, with a resolution of 1 cm (Almond et al., 1999). Measurements of gantry and collimator angles were performed to check the correspondence between the readings at the treatment control panel or the display monitor, the mechanical scale readings and the absolute position. The gantry and collimator were fixed at 0 ^{0}. The field size indicator was carried out to check that the readout of the field size agreed with the measured light field size.

The accuracy and linearity of the treatment table in the lateral, longitudinal and vertical motion were checked by performing the treatment couch position indicator test. For the linearity test for LINAC an integrated treatment time (TT) of 50 MU, 100 MU and 200 MU for 15 MV beam was measured with a field size of 10 x 10 cm^2 and SSD of 100 cm at depth of 10 cm. Using the same field size and source to surface distance for the LINAC, an integrated treatment time of 0.3 min, 0.6 min, 0.9 min, 1.2 min and 1.5 min was measured for the Cobalt treatment unit at a depth of 5 cm.

The light and treatment field coincidence were also conducted to test the congruence of the radiation and light field at various gantry angles by aligning a piece of paper at 100 cm SSD to the crosshairs. The tolerance for the mechanical checks was expected to be within 2 mm.

Safety Check

The safety assessments were performed for door interlocks, warning lights, audio-visual monitors, emergency switches and radiation survey of the control room and the console. The safety checks were also performed for the safety of the staff and the public, in order to avoid undesirable irradiation. The shielding limit for leakage radiation is 0.1 % of the useful beam at 1 m, from the Cobalt-60 source, or the target of the linear accelerator (Hartmann, 2006). These checks should be functional according to the IAEA TRS 398 protocol.

Calibration of Radiometric Films

The radiochromic film dosimeter (GafChromic EBT3) was calibrated in order to assess the doses within an acceptable range. A traceable calibrated ion chamber from the National Metrology Institute of South Africa was used to convert the charged particle readings to mean dose in air, in its sensitive volume. No separate electrometer calibration factor (K_{ele}) was required for calculating the dose assessed by the EBT3 film. The electrometer has the ability to store all correction factors required in the measurements and then compensate the corrected reading.

For the dose range used for calibrating the EBT3 film, rational functions were used. This is because they are simple for inversion and determination of density as a function of dose. It is expected that the increasing exposure would increase the optical density of the film as it progressively becomes darker. The rational functions therefore entail fewer calibration dose points, films and it saves time and close to a constant value at high dose level. In most cases, not more than five to eight dose points, distributed in a geometric sequence are required.

The calibration processes involved cutting of the EBT3 film in to smaller sizes, irradiating them, using both Cobalt and LINAC, scanning and reading of the films and finally determining the optical density of the film.

Cutting of GafChromic EBT3 Film

Each sheet (12.8 x 14.7 inches) of the EBT3 film was cut into rectangular pieces of dimensions 2 cm x 3 cm, for easy orientation, by using a sharp pair of scissor. EBT3 film is orientation dependent of the film. This behaviour results from the needle-like shape of the particles of the active component and their preferential alignment parallel to the short edge of the film (Niroomand-Rad et al., 1998). Figure 20 shows the rectangular pieces of the EBT3 films.

Figure 20: Pieces of EBT3 film.
Source: Field Survey, 2017

Irradiation of GafChromic EBT3 Films

Water and solid plate phantoms, both of PMMA (as shown in Figure 16) were irradiating with Cobalt-60 and LINAC respectively for the calibration of the films. The equipment used for the performance of the quality control were also used for the irradiation (Appendix B). The phantoms were used because of their availability and suitability for photon beam measurements. The field size used for the irradiation of the films was 10 cm x 10 cm at the isocenter and the source to surface distance (SSD) was set at 100 cm for Cobalt-60 and LINAC treatment machines.

For LINAC Irradiation

The film was irradiated perpendicular to the beam central axis at a depth of maximum dose (d_{max}) of 1.5 cm and 2.5 cm for the photon energies of 6 MV and 15 MV respectively. The solid plate phantom with dimension of 30 x 30 cm^2 and 5 cm thickness was used for this measurement following the IAEA

TRS 398 code of practice with reference dose rate of 600 Gy/MU.

One piece of the film at a time was placed on the solid phantom exposed at one of the following dose levels, 0, 20, 40, 80, 160, 240, 320, 400, 500 cGy using the 6 MV X-ray beam of the Elekta Synergy LINAC. This process was repeated for 15 MV and the absorbed dose from the LINAC was measured using a calibrated ion chamber and the electrometer. These dose values were converted to monitor unit (MU). The room temperature and pressure were recorded to be 25.4 °C and 100.27 kPa. Correction and scaling factors were applied for the solid plate phantom.

The monitor unit calculation to the isocenter was:

$$MU = \frac{D}{\dot{D}_0 \times S_c(r_c) \times S_p(r_d) \times TPR(d, r_d) \times WF(d, r_d) \times TF \times ISF} \quad (30)$$

where the dependent variables D is the dose to the calculation point, S_c is in air output ratio, S_p is the phantom scatter factor, TPR is the tissue phantom ratio, WF is the wedge factor, TF is the tray factor and ISF is the inverse square factor given as:

$$ISF = \left(\frac{SSD_0 + d_0}{SAD}\right)^2 \quad (31)$$

SSD_0 is the source to surface distance under normalization conditions, SAD is the source to isocenter (axis) distance, d_0 is the reference depth. The independent variables are defined as, r_c is the field size defined by the collimator jaws, r_d is the field size at the depth of the calculation point, d is the depth to point of calculation. Figure 21 shows the setup of the solid plate phantom.

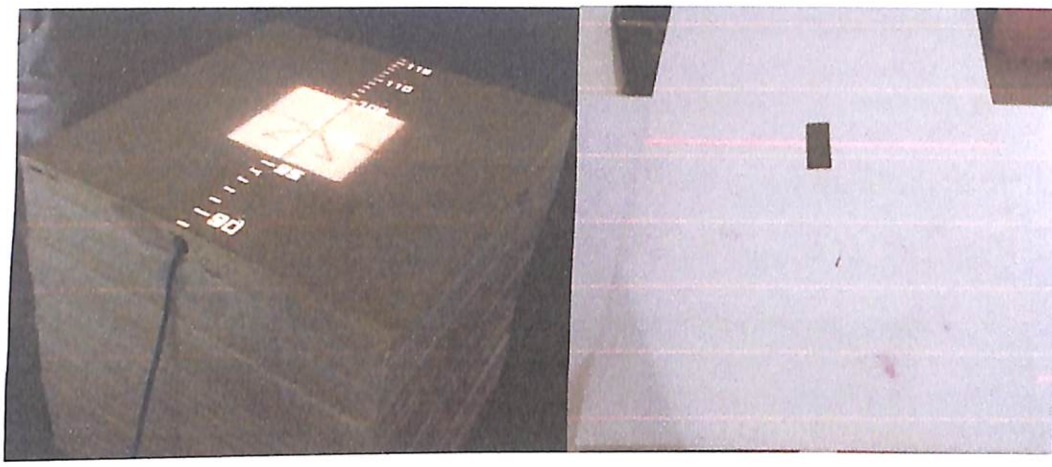

Figure 21: Solid plates phantom setup.
Source: Field Survey, 2017

For Cobalt-60 Irradiation

The EBT3 films irradiations were also performed with the Cobalt-60 unit (Theratron Equinox 100; Best Theratronics). The dose rate and the irradiation time of the Co-60 were determined by performing a dose calibration, following the TRS398 protocol described in Appendix A. The EBT3 films were placed perpendicular to the beam central axis, at a depth of 5 cm in the water phantom for a field size 10 x 10 cm^2. The water phantom was filled with water for the beam output measurement. Correction and scaling factors were corrected for the water phantom. One at a time, the pieces of the film were placed in the water phantom and exposed to doses ranging from 0 - 500 cGy, specifically, the dose levels were 0, 20, 40, 80, 160, 240, 320, 400, 500 cGy. These dose values were calculated and converted to treatment time (TT) as:

$$TT = \frac{Prescribed\ Dose}{Percentage\ Depth\ Dose * Dose\ Rate * Scatter\ factor} \tag{32}$$

where the scatter factor is equal to 1.0. The room temperature was recorded to be 22.8 ^{0}C and 101.15 kPa was recorded for pressure. The relationship between the dose to the film and the optical density was determined as the calibration curve as discussed in chapter four. The uncertainty was analyzed for the measurement as a standard deviation relative to the measurement, by using equation (13). Figure 22 is a diagram of the water phantom with reference field size of 10 x 10 cm^2. The EBT3 films were stored in a dark location until they were scanned.

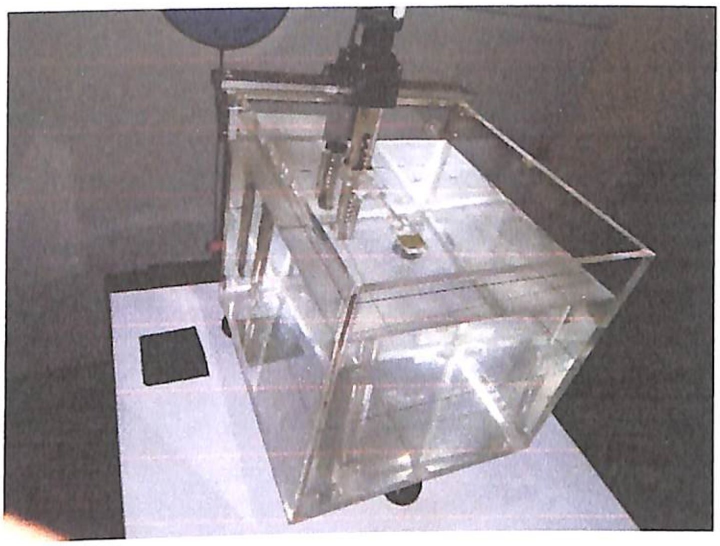

Figure 22: Irradiation setup for Cobalt-60.
Source: Field Survey, 2017

Scanning of GafChromic EBT3 Films

A flatbed scanner, Epson Stylus (CX5900) with 24-bit colour, 612 x 842 pixel, and two other commercial and widely used scanners named Scanner A (Inkjet) and Scanner B (HP ScanJet) were also used for the scanning of the films after irradiation. Although, the RGB (red green blue) scanner is recommended for scanning of the film, it was not available. However, because the dose range readable by Epson Stylus is similar to the recommended scanner, it was therefore used, to read all the films with its scanning parameters in professional mode. It is important to turn off all image adjustments features on the scanner so that the adjustment icons appear gray.

All the films were scanned in the landscape orientation, in order to reduce variations within the film as recommended by the manufacturer, and

Menegotti et al., (2008). The shorter side of the film was oriented parallel to the scan direction to minimize the effect of lateral response artefact. The films were positioned in the center of the scanner in the direction perpendicular to the scan direction. GafChromic EBT3 film is posterior-anterior symmetrical, therefore it can be scanned with either side facing the light source on the scanner. Uniformity test at a reproducible central location on the scan surface was checked. This was checked by placing the unexposed films on the scanner and scanned. To identify which film was exposed to which dose, the exposed films were labelled at the bottom left corner. This labels A, B, C, D, E, F, G, and H corresponded to the doses of 20, 40, 80, 160, 240, 320, 400, 500 cGy respectively for each of the photon of energies of 1.25 MeV, 6 MV and 15 MV. Figure 23 shows pictures of the exposed and unexposed films.

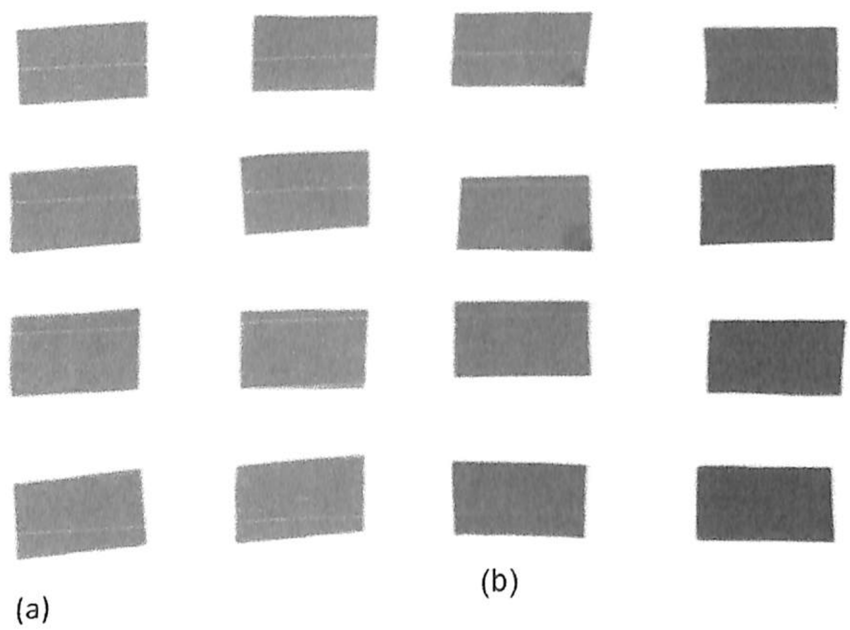

Figure 23: Scanned EBT3 Films of 2 cm x 3 cm dimensions: (a) unexposed films; (b) exposed to 6 MV beam energy.

Source: Field Survey (2017

Reading of GafChromic EBT3 Films

The scanned images of the exposed EBT3 films were imported into the image processing software, ImageJ1.46r/Java1.6.0_20 (64 bit) (National Institute of Health, Bethesda). The film image data, which was saved in tagged image file format (TIFF), were splitted into colour channels of red, green and blue shown in Figure 24. The first of the reading was to measure the mean gray value of the unexposed film (background). A rectangular selection of 40 mm x 60 mm was chosen for each scanned image and colour channel. The region of interest (ROI) when measured with the ImageJ, gives the mean pixel value, representing three images of the same size corresponding to each colour channel (red green blue) colours. The pixel value is a measure of the amount of light that is transmitted through the film during scanning. The pixel values were in gray level units, and in the range 0-255, and after calibration, the pixel values of 612 x 842, were converted to optical density.

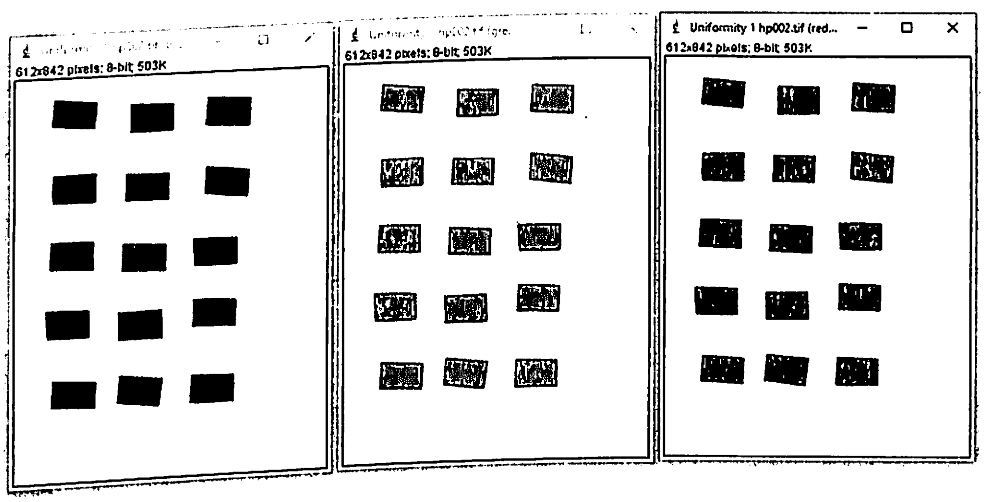

Figure 24: Splitting of channel into RGB colours.
Source: Field Data, 2017

The response values corresponding to each channel determined, from the pixel readings at different dose values were recorded. The sensitometric curve data were fitted with a fourth order polynomial equation. The sensitometric curve equation was used to convert the pixel values recorded to dose. The same procedure was conducted for all the photon beam energies used in the study (1.25 MeV, 6 MV and 15 MV). Equation (14) was adopted and used to calculate the optical density of the film. The pixel value exposed is equivalent to the light intensity transmitted through the exposed film and the unexposed pixel value represents the light intensity of unexposed film indicated in Equation (14). The optical density (OD) of the film scanner colour channel was calculated using equation (33) as:

$$OD = -log_{10}\left(\frac{Mean\ Pixel\ Value_{exposed}}{Mean\ Pixel\ Value\ _{unexposed}}\right) \tag{33}$$

Figure 25 shows the images of the EBT3 films and its corresponding scanning data for analysis using the red channel.

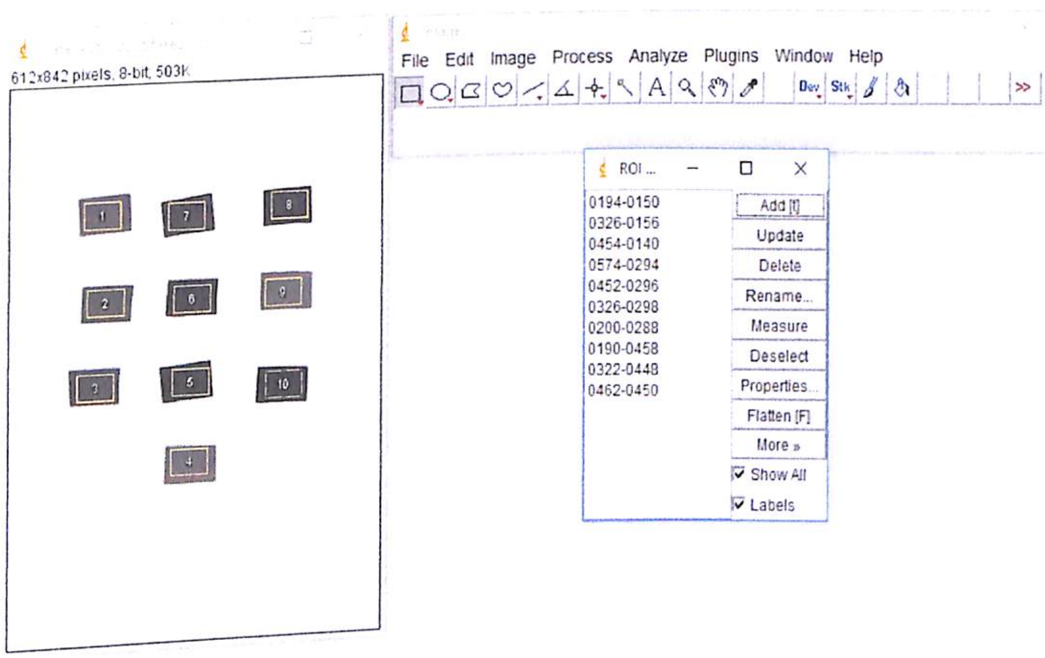

Figure 25: Images of EBT3 films and scanning process using the red channel.
Source: Field Data, 2017

Phantom Design

Two phantoms named Adelaide phantom A and Adelaide phantom B were designed and constructed based on the scan images of the standard anthropomorphic phantom (as shown in Figure 4) and a patient CT scan images respectively to provide optimization and standardization. Therefore, in this section the materials and methods used for the construction of the Adelaide phantom A and B, and the attenuation coefficients of the tissues within the thoracic region of the breast are presented. The materials used for the construction of the Adelaide phantom A and B were mainly Perspex and polystyrene.

Perspex

Perspex sheets of thicknesses 10 mm and 20 mm, and of density 1.19 g/cm^3 were used to construct the Adelaide phantom A and B respectively. The perspex, also known as PMMA, Lucite, or Plexiglas, has a chemical composition of $(C_5O_2H_8)_n$ with densities of 0.08 g/cm^3 for hydrogen, 0.5998 g/cm^3 for carbon and 0.3196 g/cm^3 for oxygen, with effective atomic number of 6.48. The perspex material was used because of its reliability, robustness and low-cost. It is easy to cut, shape and modify by adding some materials after fabrication. It does not deform over a long period of time, and homogenous slabs can be obtained. The phantoms were fabricated to mimic the thorax (trunk) of a standard female adult human with detachable breast.

The Association of Official Analytical Chemists (AOAC) method was employed in this study (Jorhem,1993; Jorhem & Engman, 2000) to analyse the elemental composition of the perspex. The elements C, Sn, K, Fe, Zn, Cd, Mg, Mn, Ca, H, O, N were determined by wet acid digestion using Milestone laboratory protocol (1996-2000). Specifically, about 6 mL of HNO_3 (65%) and 1 mL of H_2O_2 (30%) were added to 0.10 g of the powered Perspex sample. The sample and acid mixture was kept in a programmed microwave oven to achieve the desired digestion. After digestion, the remaining digestate was allowed to cool. Subsequently, the digestate was transferred into a 20 mL volumetric flask of distilled water. The metal ion compositions of the standard and sample solutions were determined using flame atomic absorption spectrometry (FAAS) in an air acetylene flame using a fast sequential Atomic Absorption Spectrometer (Varian AA240 FS) at the Ecological Laboratory (Ecolab), University of Ghana. A calibration curve showing a plot of the absorbance of each element versus the element concentration was utilized to determine the concentration of each element in the Perspex samples shown in Table 8.

Table 8: Elemental Composition of Perspex

Element	Concentration (%)
C	19.5510
Sn	0.784
K	0.45
Fe	0.1804
Zn	0.0036
Cd	0.0057
Mg	0.0772
Mn	0.0158
Ca	0.0165

Source: Field Data, 2017

Polystyrene

Polystyrene, a long chain hydrocarbon with chemical formula of C_8H_8, was used for the phantom construction. Properties of the polystyrene used are shown in Table 9. The polystyrene used for the study was a widely used solid plastic which is hard, brittle and inexpensive.

Table 9: Properties of Polystyrene

Properties	Measure
Density	0.94-1.04 g/cm^3
Melting point	~ 240 ^{0}C*
Solubility in water	insoluble
Solubility	Non soluble in acetone**
Thermal conductivity	0.033 W/ (m.K)

Source: Adopted from *Wunsch, 2000; **Wypych, 2012

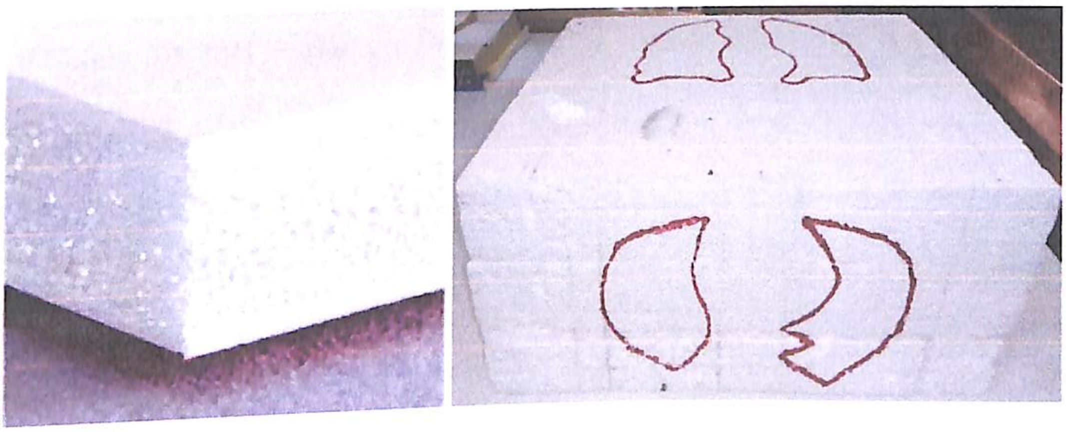

Figure 26: A picture of the polystyrene used in the study.
Source: Field Survey, 2017

Fabrication of Phantoms

In the study phantoms were construction as a physical representation of the female thoracic part of the body's anatomy. Materials that are readily available locally and have physical densities comparable to those of tissues found in the thoracic region of the human body were sought for the study. The materials included a balloon, plastic bottle and polyurethane foam representing the lung tissue, clay, mango seed and cork, representing the muscle and plaster of Paris (POP), cassava stick, polyvinyl chloride (PVC) pipe were used to represent the bone and candle, wax, crushed egg shell and rice were also used for glandular tissues.

Adelaide Phantom A

Two body parts were constructed, namely the thorax (trunk) and the detachable breast component. The exterior dimensions of the moulded part of the trunk was of length 30 cm, width 30 cm and of height 15 cm. The cone shaped breast component of the phantom moulded was of base 12.5 cm, height 8 cm and nipple size of 3.5 cm diameter. The detachable breast was glued to the trunk representing fully the upper part of the average female adult. An opening was created at the posterior of the side of the phantom to enable the placement of materials that make up the phantom. Figure 27 shows a picture of the constructed Adelaide phantom A.

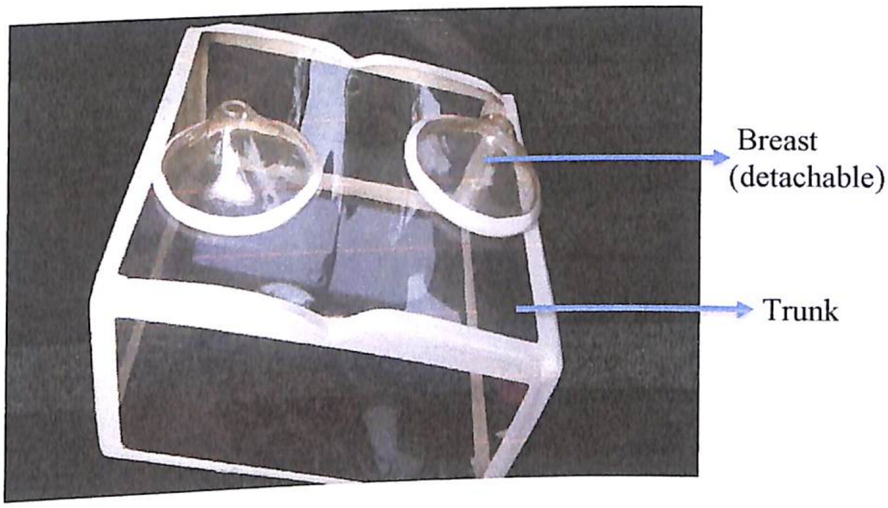

Figure 27: A picture of the Adelaide phantom A.
Source: Fieldwork, 2017

The physical dimensions of the phantom were determined based on the existing anthropomorphic phantom to mimic an average breast cancer female patient. Polystyrene material was used to shape the critical organs located within the female thorax of the body. Local materials of balloons, mango seed and cassava stick were also used to represent the critical organs of the lungs, heart and spinal cord respectively. The images of the scanned anthropomorphic phantom were used to demarcate the depth of the critical organs in the Adelaide phantom as shown in Figure 28.

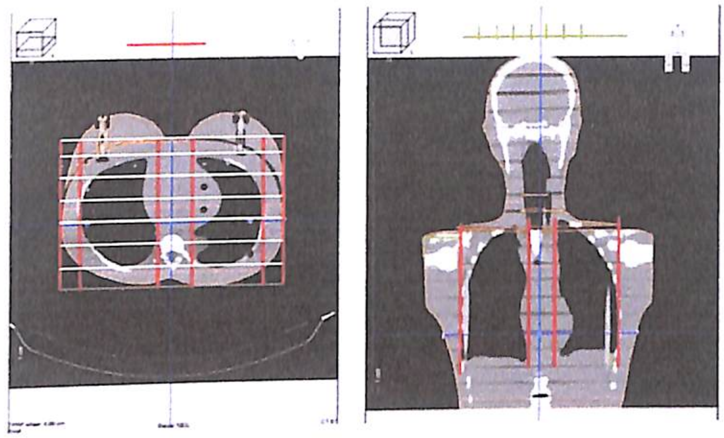

Figure 28: Scan images of the anthropomorphic phantom.

Source: Fieldwork, 2017

Adelaide Phantom B

Adelaide phantom B was constructed based on patient CT scan images of 400 mA and 120 kV. The phantom was made up of perspex sheet of size 8x4 inches. The perspex was cut into eighteen (18) slabs with the image slice thickness of 5 mm, representing the thorax of the female body. Firstly, the CT scan images were projected on a screen with a projector. These recorded images were traced out with a marker on an A3 tracer paper. The tracer paper was later placed on the 20 mm Perspex sheet and the cutting machine was used to cut the paper to the required shapes as shown in Figure 29.

Furthermore, the lungs and heart were shaped out using a drilling machine. Afterwards the slabs were arranged in the ascending order starting from 0 - 17. A stand was made for the phantom, designed with the perspex with holders, to keep the slabs tightened. Adelaide phantom B was smoothened to shape as shown in Figure 30. No attempt was made to simulate the skin layer for the Adelaide phantoms.

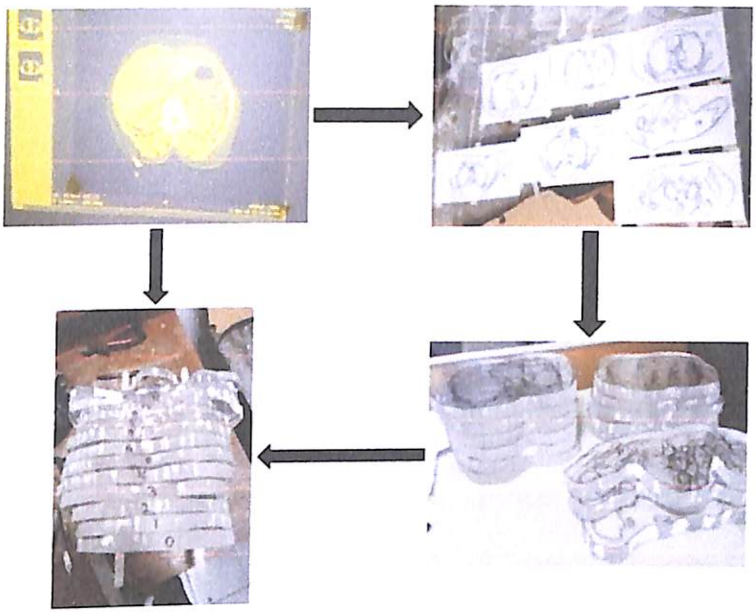

Figure 29: Adelaide phantom B construction processes.

Source: Fieldwork, 2018

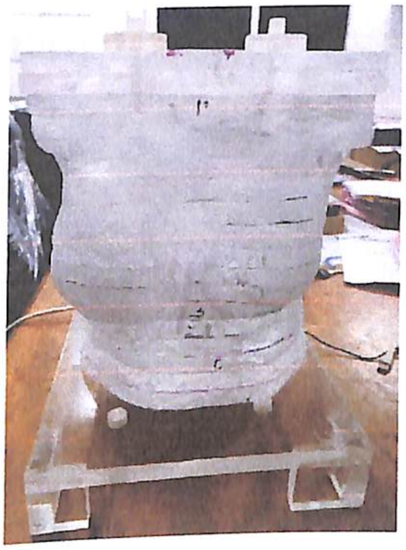

Figure 30: A picture of the Adelaide phantom B.

Source: Fieldwork, 2018

Tissue-Substitutes

The amount of X-ray radiation absorbed by each element in tissue-substitutes and the characterization of the relative density of the substance was determined during the CT scan of the Adelaide phantoms. Materials, with an atomic composition as close as possible to the simulated tissues, were identified and used as tissue-substitutes for the Adelaide phantoms. The materials included *a balloon, plastic bottle and polyurethane foam representing the lung tissue, clay, mango seed and cork, representing the muscle and plaster of Paris (POP),* cassava stick, polyvinyl chloride (PVC) pipe were used to represent the bone. Candle, wax, crushed egg shell and rice were also used for glandular tissues. These were chosen based on their similarity in composition to the human tissues. The Hounsfield Unit (Hounsfield number) was determined using the Emotion CT Scanner (Siemens AG, Munich, Germany) for the tissue densities used for the study. Four tissue-substitutes at a time were placed in a rectangular polystyrene phantom of 30 cm x 15 cm. CT scanning was conducted, under identical conditions as those for radiotherapy patients. The mean Hounsfield numbers were determined in circular regions of diameter 1.3 cm with the centre coinciding with the centre of the tissue equivalent samples. Perturbations on the result from beam hardening were corrected assuming all the tissues were water equivalent, and at various positions in the phantom, the CT values gave the same reading for water samples.

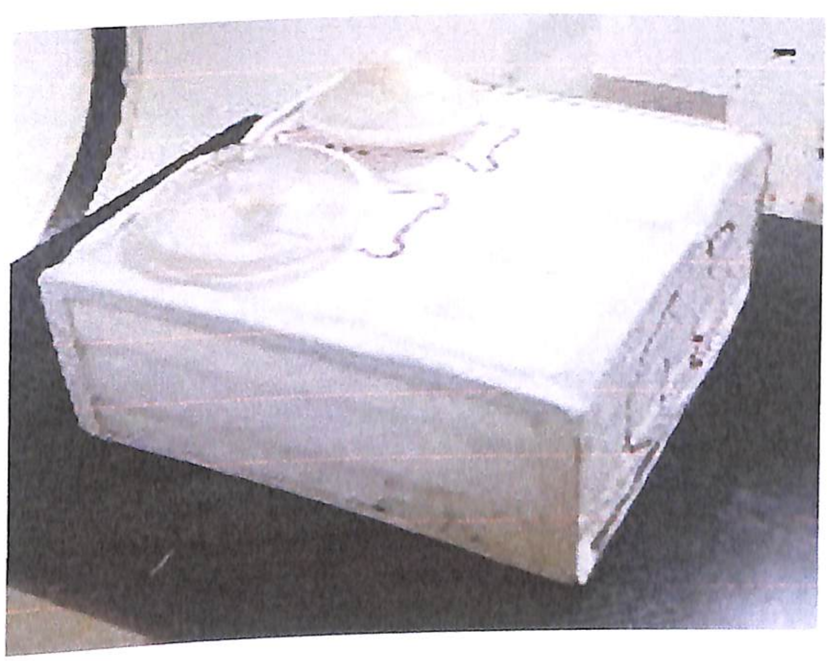

Figure 31: CT scan of the Adelaide phantom A.
Source: Fieldwork, 2017

The tissue-substitutes of the anthropomorphic phantom, for the lung and muscle are well suited to dosimetry according to Knöös (1991). The elemental compositions for muscle, lung, average bone and cortical bone were taken from ICRU (1989) as shown in Appendix C.

CT scans are used to correct for tissue inhomogeneities in radiotherapy treatment planning, it is important to obtain a precise relationship between CT number and electron density. Therefore, the electron densities of the local materials from the CT numbers identified in each voxel of the CT images were calculated from equations (20) and (21).

Experimental Dose Measurement

The experimental and theoretical measurements conducted to determine the absorbed doses to the breast and critical organs, using the phantoms, are described in this section. During treatment at the radiotherapy unit, a patient is made to lie supine on the treatment couch, with the head of the patient toward the gantry. The collimator, gantry and couch angles are set to zero, with the line from the patient's sternal notch to xiphisternum parallel to the gantry axis of rotation with the help of lasers, employing source to surface (SSD) treatment technique. The same setup was used for the phantoms to mimic an actual treatment procedure. Measurements were made for the left breast (mastectomy) and intact breast (both breasts attached) irradiation based on the protocols of the study facilities. Two tangential beams (medial and lateral) were used.

The materials used for the experimental measurements included the anthropomorphic (standard) and Adelaide phantoms, CT Scanner, Treatment Planning Systems (TPS), the linear accelerator and cobalt machine to assess the doses to the critical organs. The methods for the measurements included the acquisition of CT data, treatment planning implementation and treatment delivery.

The phantoms (anthropomorphic and Adelaide) were scanned separately with the Emotion CT scanner at the Sweden Ghana Medical Centre (SGMC) with 5 mm slice width. The scanned images from the CT were imported to Oncentra Master Treatment Planning System version 4.3 for three-dimensional (3-D) conformal external beam planning for the LINAC machine, and Prowess Panther TPS for the Cobalt machine. The TPS generated the beam shapes, and used them to perform the dose distribution of the phantoms as shown in Figure 32.

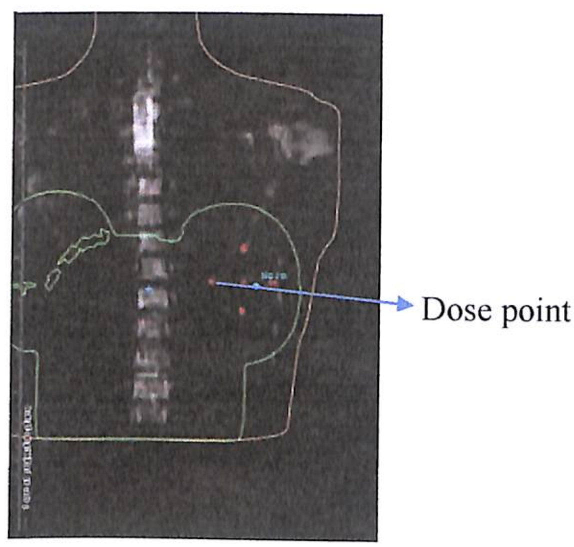

Figure 32: Representation of dose point information.
Source: Fieldwork, 2017

The anthropomorphic phantom was placed on the treatment couch to match the set up for the CT scan. EBT3 film of rectangular size of 2 cm x 3 cm were placed at different locations on the left breast and beneath the left breast of the phantom. In order to easily identify the positions, the EBT3 films were numbered as 1T, 2T, 3T, 4T and 5T for measurements on top of the left breast.

The dose measurement beneath the phantom was numbered 2B, 3B, 4B and 5B. An absolute dose prescription of 50 Gy at 2 Gy in 25 fractions was given in medial and lateral tangential for 6 MV photon beam. Figure 33 shows the irradiation of the anthropomorphic phantom and the positions of the EBT3 films.

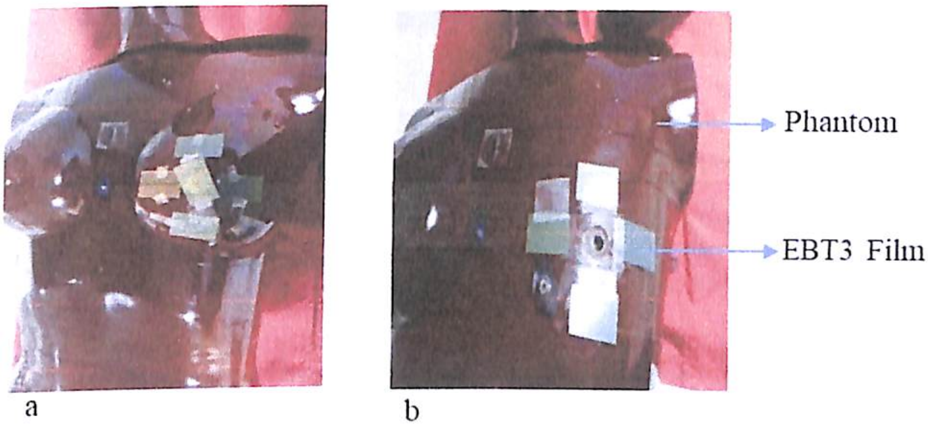

Figure 33: Setup of the irradiation of the anthropomorphic phantom with EBT3 Films: (a) intact breast; (b) mastectomy.

Source: Field Data, 2017

The experimental method used for the anthropomorphic phantom was also used for the Adelaide phantoms. Balloon, clay, plaster of Paris and wax were inserted into the Adelaide phantom A to mimic the lung, heart, spinal cord and glandular tissues respectively. Figure 34 shows the irradiation setup.

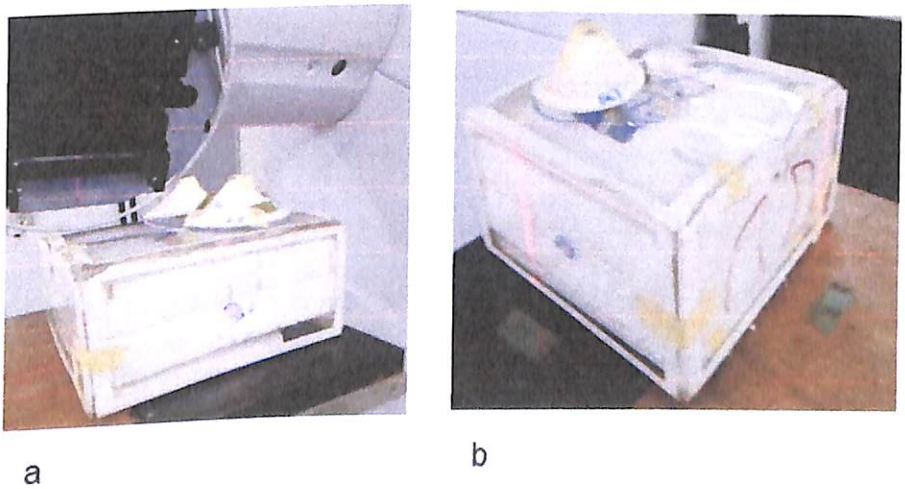

Figure 34: Setup of the irradiation of the Adelaide phantom A with EBT3 Films: (a) intact breast; (b) mastectomy.

Source: Fieldwork, 2018

The Adelaide phantom B went through all the planning stages including CT scanning and simulation same as the anthropomorphic and Adelaide A phantoms. For the Adelaide phantom B, only the left breast and the critical organs were measured using the EBT3 film. For this phantom, mastectomy measurement was not assessed, because the breast component was embedded in the construction, therefore it made it difficult to measure without the left breast (mastectomy).

The gantry and collimator angles and SSD were kept constant in all the measurements. The beam information is shown in Appendix D. After irradiation the EBT3 films were scanned in the landscape orientation. The scanning was done with Epson Stylus scanner 72 hours after irradiation. The scanned images were read with the ImageJ v1.46r in the red channel with area of 40 mm x 60 mm. The dose response values were calculated using the sensitometric curve equation, generated from the EBT3 film calibration. The same procedure was carried out at the Cobalt-60 treatment unit.

Theoretical Dose Measurement

In the study, absorbed dose to water was computed in a virtual phantom with approximate full scatter conditions with gamma photon as the radiation source. Monte Carlo Neutral Photon (MCNP) code system was used to simulate the properties of the system geometry of the phantom following the International Atomic Energy Agency [IAEA] Technical Report Series 398 protocol. The theoretical measurements of the study were limited to the use of virtual simulation of water phantom for the Cobalt-60 treatment unit.

Monte Carlo Geometry

A gamma source of mean energy 1.25 MeV (^{60}Co) was used as the radiation source in the Monte Carlo simulation. A water (H_2O) phantom was used as the reference medium for measurement of absorbed dose for photon beams as recommended by the IAEA code of practice (IAEA, 2000). As the beam incident on the phantom, the absorbed dose varies. This variation is dependent on the beam energy, depth, field size, and distance from the source and beam collimation system (Khan, 1994). Thus, the modelling of the dose in the phantom considered the variations that affect dose distribution.

According to the IAEA TRS398, the absorbed dose to water at the reference depth z_{ref} in water, for ^{60}Co beam and in the absence of the chamber, is given as:

$$D_w = MN_{D,w}, \tag{34}$$

where, M is the dosimeter reading and $N_{D,w}$, calibration factor for the chamber. The reference point of the chamber is positioned at z_{ref} in accordance with the reference conditions for the determination of absorbed dose to water in ^{60}Co gamma ray beams as shown in Table 10.

Table 10: Reference Conditions for the Determination of Absorbed Dose to Water in ^{60}Co Gamma Ray Beams

Influence quantity	Reference value
Phantom material	Water
Chamber type	Cylindrical
Measurement depth	5 cm
Reference point of the chamber	Cylindrical chambers on the central axis at the centre of the cavity volume.
Position of the reference point of the chamber	Cylindrical chambers at the measurement depth z_{ref}
SSD or SAD	100 cm
Field size	10 cm x 10 cm

Source: Adopted from IAEA, 2000 and modified

Temperature and pressure, electrometer calibration, and ion recombination factors were corrected. The procedure adopted by IAEA TRS398 enables the use of peripheral dose measurement with other detectors in the radiation field. Figure 35 shows the experimental setup of the irradiation geometry used for the determination of absorbed dose to water.

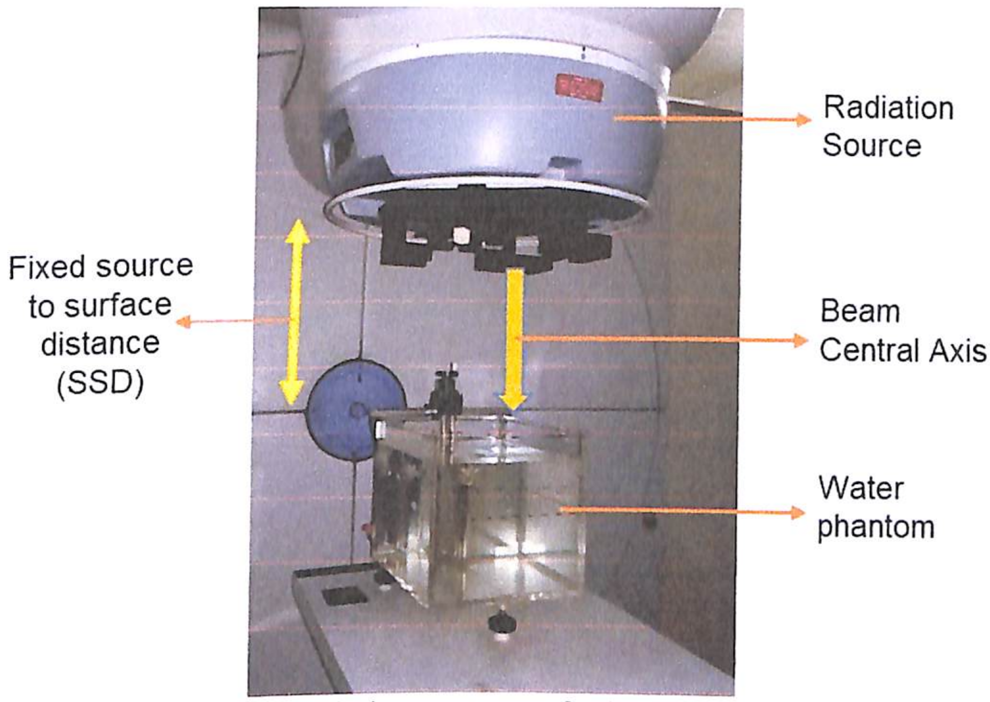

Figure 35: Setup for irradiation geometry for beam calibration.
Source: Fieldwork, 2017

A photon virtual source was used for simulating the arbitrary beam distribution using Monte Carlo code. A virtual detector of tally F5 was placed at a considering point inside the virtual phantom to calculate the dose absorbed using MCNP code. The MCNP code was used because of its ability to simulate any 3D geometry with precision. The simulated virtual phantom used has the same absorption and scatter properties as water. The code sectioned or meshed the 1000 cm^3 water phantom into 25,000 smaller volumes for which the dose for every volume element (i.e. voxel) could be calculated. The meshing of the phantom was 50x50x10 in x, y and z planes respectively. The results of the dose in the z plane were plotted using MATLAB. Figures 36 and 37 shows the 3D and 2D geometric view of the water phantom and the source respectively.

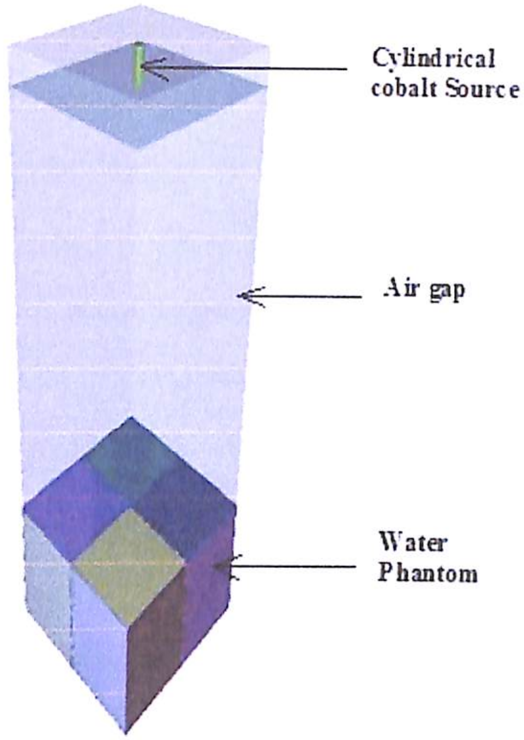

Figure 36: MCNP 3D geometric view of simulated virtual phantom.

Source: Fieldwork, 2017

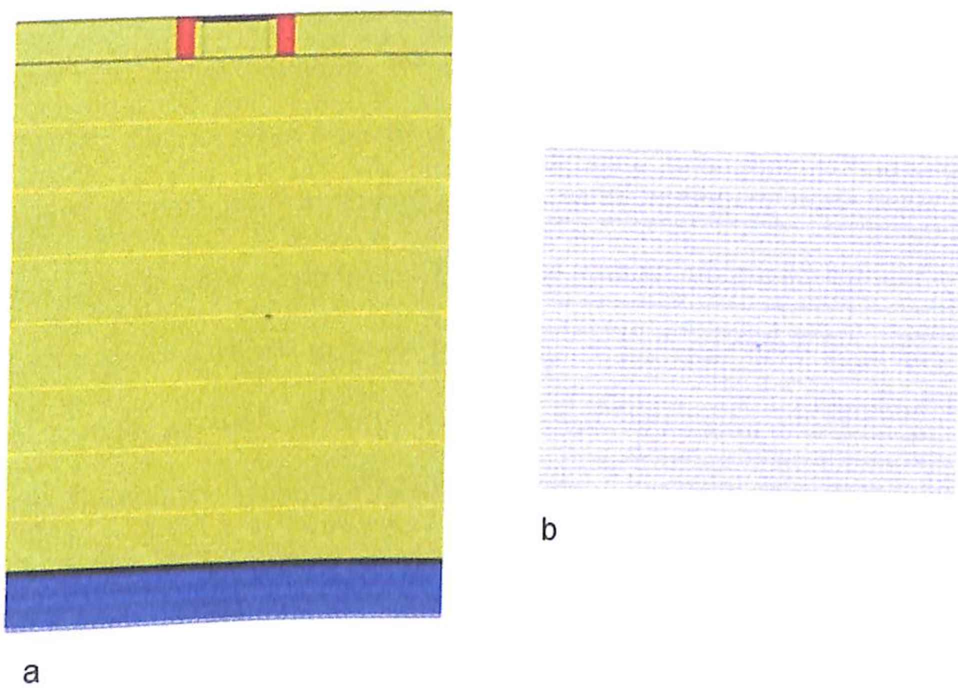

Figure 37: MCNP 2D Geometric View of Simulated Virtual Water Phantom: (a) 50x10 simulated tissue meshing in x-z plane (b) Cross sectional view of 50x50 simulated tissue meshing in x-y plane.

Source: Fieldwork, 2017

In each quadrant the cells in the direction into the plane are numbered, followed by the cells out of the plane. Each quadrant gives two layers. In the first quadrant, cells 1-64 are numbered in the direction into the plane, and cells 65-128 are numbered in the direction out of the plane. In the second quadrant, cells 129-192 are numbered in the direction into the plane and cells 193-256 are numbered in the direction out of the plane. The same numbering is carried out for the third and fourth quadrants that result in 257-320; 321-384 and 385-448; 449-512 respectively (Appendix E). The labelling places the first and third quadrant on the surface close to the photon beam and quadrants two and four below first and third quadrants respectively.

Cylindrical geometries were employed for modelling of the source holders, while planer geometries were used for the virtual water phantom. The gamma source was specified as surface source, collimated beam and mono-energetic source energies with uniform distribution of radioactivity. The gamma source was modelled to emit photons perpendicular to the phantom, parallel in direction of cylinders containing the source in direction of z plane. These hypothetical source energies were assumed as a disc, with a diameter of 1.5 cm and parallel to x-y plane. The typical diameter of the cylindrical teletherapy source is between 1 and 2 cm and the height of the cylinder is about 2.5 cm. The smaller the source diameter, the smaller is its physical penumbra and the more expensive is the source. A diameter of 1.5 cm was chosen as a compromise between the cost and penumbra (Podgorsak, 2005).

The materials constituting the geometric setup were stainless steel, water and air. This is because Co-60 radionuclides are contained inside a cylindrical stainless steel capsule, sealed for shielding purposes, and a mechanism for bringing the source in front of the collimator opening to produce the clinical γ-ray beam. Therefore, the elemental composition of the source holder was stainless steel 316L. Whilst that of the water in the phantom constituted hydrogen and oxygen (H_2O) and air was used to fill the gaps in the geometry.

Monte Carlo Simulation

In the MCNP input file the F6 tally was used for the absorbed dose contribution from the photon radiation and F4 tally (electron flux averaged over a cell) was used for the electron contribution from secondary electron. The F6 tally was the energy deposition card in MeV and it was applicable to photons and neutron radiation. The Co-60 source strength at the time of the experimental measurement was used to determine the number of photons emitted by the source per second. The strength of the source and its associated photons, together with dose conversion tables in reference according to IAEA TRS398 was used to calculate the dose per each cell.

The decay factor of the source was calculated using the formula:

$$DF = e^{\frac{-0.693\times t}{5.27}} \qquad (35)$$

where t is the time difference in years between the date of commissioning and the current time of the study, 5.27 in years is the half-life of Co-60.

Statistical Analysis

The experimental analysis involved the use of Microsoft Excel and Mintab statistical software tool version 17 to calculate and analyze the research data of the measured parameters. The software tools were used to model the relationship between the optical densities, calculated from the pixel values measured with ImageJ, and the dose. This was done for the calibration and exposure of the EBT3 film dosimeter.

Regression analysis was used to model the relationships between linear predictor functions, whose unknown model parameters were estimated from the data. The relationship between the dose to the film and the response when the film was exposed was determined as the calibration curve, using regression analysis. Additionally, invariable regression (only one independent variable) approach was also used to predict the relationship between the response variable (relative absorbed dose) and the predicator (layer number) representing the tissues within the body from the MCNP simulation.

The Analysis of Variance (ANOVA) was used to analyse the differences among the mean of the various doses and scanner variations and their associated procedures. The ANOVA, correlation and regression analyses were performed by comparing the mean and p-values. The confidence level was set at 95% ($p = 0.05$) to make a decision based on the analysis of the data for the various models.

ImageJ software as described in chapter two was used to read and analysis all the scanned images of the EBT3 films exposed with doses ranging from 0-500 cGy. ImageJ was used to split the scan images into the RGB (red green blue) colours. All the images in the study were read and saved in the TIFF format. The software was used to select the area (region of interest) and pixel coordinates (width and height). The ImageJ software also calculated the pixel values and intensity of the selected image. ImageJ software calculates the standard deviation associated with the average dose reported for each image scanned. Each time, measurements were obtained from a scanned image, the standard deviation was noted for each image. The standard deviation is determined as the square root of the variance of each individual observation.

Statistically, various estimated parameters were presented as the average or mean values of the various parameters plus the standard deviation, σ. The percentage error (δ) was also estimated for the measured dose and the expected doses of the various parameters used. The percentage error δ between the measured dose $D_{measured}$ and the expected dose $D_{expected}$ was calculated according to the relation:

$$|\delta| = \frac{D_{expected} - D_{measured}}{D_{measured}} \times 100 \qquad (36)$$

δ was calculated for each measurement to estimate the difference between the actually measured, and the calculated dose at the central beam.

Chapter Summary

This chapter provides detailed information on the experimental and theoretical framework targeted for female breast cancers. It described the dosimetry equipment and methods used to measure, analyse and model the dose distribution for verification of breast cancer treatment using the linear accelerator and Cobalt-60. The chapter also gave description of the calibration procedures of the EBT3 films dosimeters. In addition, it included the method for the construction of the Adelaide phantoms with local materi als. Furthermore, MCNP geometry simulation of the Cobalt-60 machine was also described. The chapter concluded with the statistical analysis of the research data.

CHAPTER FOUR

RESULTS AND DISCUSSION

Introduction

In this chapter, the results are presented in four groups. Firstly, the dosimetry parameters, which include the correction factors, beam output factor used in the study, are presented in tables and discussed. The quality control on the equipment and the radiation safety survey are also discussed. Secondly, results from the EBT3 dosimetry specifically of the calibration curves, optical densities, area, scanner orientation and energy dependence on dose are discussed, with tables and graphical representation. Thirdly, the results of the geometrical simulation of the Cobalt-60 and experimental results using MCNP, and its significance on dose and depth are presented and discussed. Finally, experimental measured results of absorbed dose using the standard anthropomorphic and the Adelaide phantoms are presented and discussed as well as the tissue substitute components. Regression analysis used to determine the relationship between planned and delivered doses to breast therapy is also discussed.

Results of Dosimetric Checks

Quality Control measurements on the treatment unit systems were evaluated at the facilities of the study to check the reliability of the operational techniques used. This is because radiotherapy involves delivering large amounts of radiation to specific targets within the human body and therefore a high degree of accuracy, reliability and reproducibility is necessary for safe and effective radiation treatment of cancer patients. This also ensures confidence in both the dose delivered to the tumour, as well as to the nearby healthy organs and tissues, thereby maximizing tumour control and minimizing adverse radiation effects.

Also the dosimetry results conducted on the beam output for the treatments unit are presented in this section.

Ionization Chamber Correction Factors

The charged particles measured from the calibrated ionization chamber depended on the type of gas and on the mass in the chamber. The polarity effect K_{Pol} was corrected during the output beam measurement to be 1.000 with the chamber voltage of +400 V. The polarity effect is necessary in dosimetry because it varies with the beam quality and the cable position (Dyk & MacDonald, 1972; Aget & Rosenwald, 1991; Klevenhagen, 1993). The values were deduced with equation (27) to correct for the ion chamber readings.

The electrometer correction factor K_{ele} was 1.000 because the electrometer and the ion chamber were calibrated as a unit. The electrometer calibration factor corrected the electrometer readings. The ion recombination correction factor K_s, is a function of the dose per pulse in accelerator beams, which changes with a dose rate was also corrected. The correction factor K_s has a value of 1.001. The ion collection efficiency was corrected to 100% at the time of the chamber calibration, and this was done at the calibration laboratory. The uncertainty of the ion chamber used in the study was 1.1%.

Temperature-Pressure Correction Factors

In radiotherapy, the temperature and pressure in the room housing the equipment depend on the environmental conditions during irradiation. These were measured and used to estimate the effect of pressure and temperature on the measurement of beam output. From equation (29), the ambient pressure and the ion chamber volume temperature were calculated. Table 11 shows the measured temperature and pressure, as well as, the calculated values for the correction factors ($K_{T,P}$) for LINAC and Cobalt machines.

Table 11: Temperature and Pressure Correction Factors for LINAC and 60Co Machines

Machine(s)	Linear Accelerator (Measured)	Cobalt-60 (Measured)	Acceptable Range
Temperature (°C)	24.60	22.80	21±3
Pressure (kPa)	100.27	101.15	100.0±5
$K_{T,P}$	1.0194	1.0044	

Source: Field Data, 2017

The correction factor for temperature and pressure used in this study were 1.0194 for LINAC and 1.0044 for Cobalt-60 machines, based on the recorded temperature and pressure from Table 11. The standard reference conditions in current use adopted from AAPM TG51 protocol, (Almond et al., 1999) for temperature, T_0 and pressure, P_0 are 22 °C and 101.325 kPa respectively. The measured temperature and pressure should be within ±3°C and ±5 kPa respectively, to allow enough time for temperature equilibrium with its surroundings to be reached after the chamber is placed in position. Tailor et al., (1998) stated that the temperature is assumed to have reached equilibrium after 5 to 10 minutes inside the ion chamber. The temperature and pressure measured were within acceptable range of 21±3 °C and 1000±50 hPa respectively from the ionization chamber calibration certificate (PTW-Freiburg).

Humidity Factor

The relative humidity should be in the range of 20% to 80% according to AAPM TG 51 protocol. According to Roger and Ross (1988), the error introduced by relative humidity, in ignoring variations, is in the range of ±0.15%. Therefore, the humidity of air was not used in the study because it might cause condensation inside the ion chamber volume affecting the response for the nylon wall chamber (Mijnheer, 1985).

Radiation Beam Output Factor

The radiation beam output was calculated for the linear accelerator and the Cobalt-60 unit from equation (26). The beam output factors increase with the field size and also the collimator opening. The beam output calculated for the linear accelerator was 126.30 cGy for 100 MU treatment time. The beam output calculated for the Cobalt-60 units was 130.56 cGy for 60 seconds treatment time. Table 12 shows the mean weekly measurements of the beam output with its percentage deviation.

Table 12: Beam Output Results from Dosimetric Data

Machine	Beam output (Gy)	Frequency	Tolerance (%)
LINAC	1.263±0.007	weekly	±3
Co-60	1.306±0.013	weekly	±2

Source: Field Data, 2017

For Cobalt-60 machine, the source was moved into position to start the treatment and returned to its safe position at the end of the treatment. Therefore, the shutter correction time was 1.0 second with a net time greater than the set time used to deliver accurately the prescribed dose during the output calibration. This is a result of switching the beam ON and OFF. The calibration factor $N_{D,W}$ for the LINAC and Cobalt-60 was 5.408 x 10^7 Gy/C because the same ion chamber was used for the dosimetry measurements. The machine characteristics did not deviate significantly from their baseline values of ±2% and ±3% acquired at the time of acceptance and commissioning of the

Cobalt-60 and LINAC systems respectively.

The outcome of radiation treatment could be said to be directly related to the precision in the delivered dose and is dependent on the accuracy of the beam data used.

Output with Gantry Angle

A field size of 10 x 10 cm^2 and SSD of 100 cm at gantry angles of 0°, 90°, 180° and 270° for an integrated treatment time of 100 MU and 60 seconds in air measurement with build-up cap for LINAC and Cobalt machines respectively are presented. All error calculations were normalized to measurement at gantry angle of 0°. Table 13 shows the beam output readings with the gantry angles used in the therapy measurements. Table 14 shows the linearity output check on the treatment units.

Table 13: Results of Output Constancy with Gantry Angle

	Treatment Unit			
	LINAC		Cobalt	
Gantry angle (°)	Beam output (nC)	Deviation (nC)	Beam output (nC)	Deviation (nC)
0	15.46	0.00	23.01	0.00
90	15.51	0.05	23.01	0.00
180	15.52	0.06	23.16	0.15
270	15.48	0.02	23.17	0.16

Source: Field Data, 2017

From Table 14, it was realized that the beam output consistency with gantry angle and linearity measured for both treatment units were consistent and was within the tolerance of ±3%.

Table 14: Results of the Output Linearity Test

	Linear Accelerator	
TT (MU)	Charges (nC)	Q/t (nC/MU)
50 MU	7.288	0.1457
100 MU	14.58	0.1458
200 MU	29.15	0.1457
	Cobalt-60	
TT (min)	Charges (nC)	Q/t (nC/min)
0.3	5.95	19.83
0.6	11.70	19.50
0.9	17.46	19.40
1.2	23.22	19.35
1.5	28.92	19.28

Source: Field Data, 2017

Results of Mechanical Checks

The mechanical checks were conducted as part of the quality control requirements. Table 15 shows the quality control measured for the mechanical checks for the Cobalt machine. The largest deviation in the collimator and gantry angles was 0.5°, which was lower than the 1° tolerance level recommended. The couch movements' deviations along the longitudinal, lateral and vertical axes was 0.1 cm which is less than 0.2 cm tolerance level. The laser alignment was verified within 0.2 cm tolerance. For the field sizes of 20 x 20 cm^2 and 30 x 30 cm^2 the deviations were found to be 20.1 x 20.2 cm^2 and 30.2 x 30.2 cm^2 respectively. All laser beams were correctly indicated in the isocentre, the smallest sphere through which the axes of the radiation beam pass in all condition. The approximate laser beam position was checked by the mechanical method to be congruent. Table 16 shows the quality control measured for the mechanical checks for LINAC.

Table 15: Results from Mechanical Data for Cobalt-60 Machine

Test	Set	Measured	Deviation	Tolerance
SSD Indicators (cm)	100	100	0.0	
	115	115	0.0	0.2
	90	89.9	0.1	
Collimator Rotation (°)	0	0.5	0. 5	1
	90	90.5	0.5	
Gantry Rotation (°)	0	0	0.0	
	90	90.1	0.1	
	180	180	0.0	1
	270	270.1	0.1	
Table Rotation (°)	0	359.5	0.5	0.5
	90°	91°	0.1	
Table Movement				
Longitudinal (cm)	10	10	0.0	
Lateral (cm)	10	10	0.0	0.2
Vertical (cm)	5	4.9	0.1	
Collimator Isocenter (cm)	0°	Within 0.2	Passed	
	90°	Within 0.2	Passed	0.2
	270°	Within 0.2	Passed	
Table Isocenter	0°	Within 0.2	Passed	
	90°	Within 0.2	Passed	0.2
	270°	-	-	
Laser Alignment				
Isocenter (cm)		Within 0.2	Passed	0.2
Congruent (cm)		Within 0.2	Passed	
Field Size (cm^2)	10x10	10.0x10.0	Passed	
	20x20	20.1x20.2	Passed	
	20x10	20.1x10.0	Passed	0.2
	20x30	30.2x30.2	Passed	

Source: Field Data, 2017

Table 16: Results from Mechanical Data for Linear Accelerator Machine

Test	Comment	Frequency	Tolerance
Optical SSD Indicators	Passed (0.1 cm deviation)	Monthly	0.2 cm
Collimator Rotation	Passed	Monthly	0.5^{0}
Gantry Rotation	Passed	Monthly	0.5^{0}
Table Rotation	Passed ($90^{0} = 91^{0}$, but within the tolerance)	Monthly	1^{0}
Treatment Table Movement Scales	Passed (table lateral) Passed (0.1 cm deviation for longitudinal and vertical readout)	Monthly	0.2 cm

Source: Field Data, 2017

From Table 16, the largest deviation in the SSD indicator was 0.1 cm which was lower than the 0.2 cm tolerance level. The couch movements' deviations along the longitudinal, and vertical axes was 0.1 cm which is less than 0.2 cm tolerance level recommended. The table rotation had a deviation of 0.1° at the 90° position. The mechanical parameters were checked to guarantee an accurate irradiation treatment and also give an impression of long term changes due to wear of mechanical points.

Radiation Safety Survey

Radiation surveys were conducted around the premises of the treatment unit for safety of the patient and staff. Tables 17 and 18 show the result of the safety and survey of radiation at the study facilities.

From Tables 17 and 18, it was observed that the safety of the patient and staff was protected. The mechanical, geometrical, safety and radiation beam output checks carried out were within the stated tolerance levels specified for testing procedures. Also, these results agree with Brahme et al., (1988), that if

Table 16: Results from Mechanical Data for Linear Accelerator Machine

Test	Comment	Frequency	Tolerance
Optical SSD Indicators	Passed (0.1 cm deviation)	Monthly	0.2 cm
Collimator Rotation	Passed	Monthly	0.5^0
Gantry Rotation	Passed	Monthly	0.5^0
Table Rotation	Passed ($90^0 = 91^0$, but within the tolerance)	Monthly	1^0
Treatment Table Movement Scales	Passed (table lateral) Passed (0.1 cm deviation for longitudinal and vertical readout)	Monthly	0.2 cm

Source: Field Data, 2017

From Table 16, the largest deviation in the SSD indicator was 0.1 cm which was lower than the 0.2 cm tolerance level. The couch movements' deviations along the longitudinal, and vertical axes was 0.1 cm which is less than 0.2 cm tolerance level recommended. The table rotation had a deviation of 0.1° at the 90° position. The mechanical parameters were checked to guarantee an accurate irradiation treatment and also give an impression of long term changes due to wear of mechanical points.

Radiation Safety Survey

Radiation surveys were conducted around the premises of the treatment unit for safety of the patient and staff. Tables 17 and 18 show the result of the safety and survey of radiation at the study facilities.

From Tables 17 and 18, it was observed that the safety of the patient and staff was protected. The mechanical, geometrical, safety and radiation beam output checks carried out were within the stated tolerance levels specified for testing procedures. Also, these results agree with Brahme et al., (1988), that if a parameter is in the range below the tolerance level, then the equipment is suitable for high quality radiation therapy,

Table 17: Results of Radiation Safety Checks

Test	Tolerance	LINAC Remarks	Co-60 Remarks
Room Entrance Interlocks	Functional	Passed	Passed
Audio Visual Monitor	Functional	Passed	Passed
Beam ON Indicators	Functional	Passed	Passed
Table Locking Brakes	Functional	Passed	Passed
Backup Dose Monitor Check	Functional	Passed	Not Applicable
Emergency Off Switches	Functional	Passed	Passed

Source: Field Data, 2017

Table 18: Radiation Survey for Treatment Room

Readings	Expected Dose (Gy)	Measured Dose (Gy)	Deviation (Gy)
1	0.90	0.89	0.01
2	0.81	0.81	0.00
3	0.89	0.88	0.01
Reception to treatment		0.13 $\mu Sv/h$	
Console		0.04 $\mu Sv/h$	

Source: Field Data, 2017

In summary, the dosimetry parameter checks were all within the appropriate limits set for each machine's performance and testing procedures. Therefore, the facilities could be said to be working self consistently.

Evaluation of GafChromic EBT3 Film Dosimetry

The scanned images of the GafChromic film were imported into the image processing software, ImageJ. These colour images, which were saved in tagged image file format (TIFF) in RGB mode, represent three images of the same size corresponding to each colour channel. This section presents the ca libration and sensitivity results of the EBT3 films, energy response of the film, results of the area selected, film orientation, uniformity and the response of the EBT3 film with different scanners.

Film Calibration and Sensitivity

A film characteristic curve (sensitometric curve) described in chapter two, was determined to establish the relationship between the applied exposure and the resulting film density. This was established for each film before using it for the dosimetry work. The corresponding optical densities for each colour channel were calculated from the pixel readings using ImageJ, and employing equation (33) as described in chapter three. The sensitometric curves data were fitted with a third order polynomial. According to Marroquin et al. (2016), the response curves of the EBT3 film do not accurately define the dynamic ranges for each colour channel, therefore, the response sensitivity of the film defined as the slope of the response curve was analysed for each dose value. Figures 38, 39 and 40, show the dose response characteristics curves for the three (RGB) colour channels as a function of the delivered dose which were used to define the dose regions of maximum sensitivity for a particular colour channel.

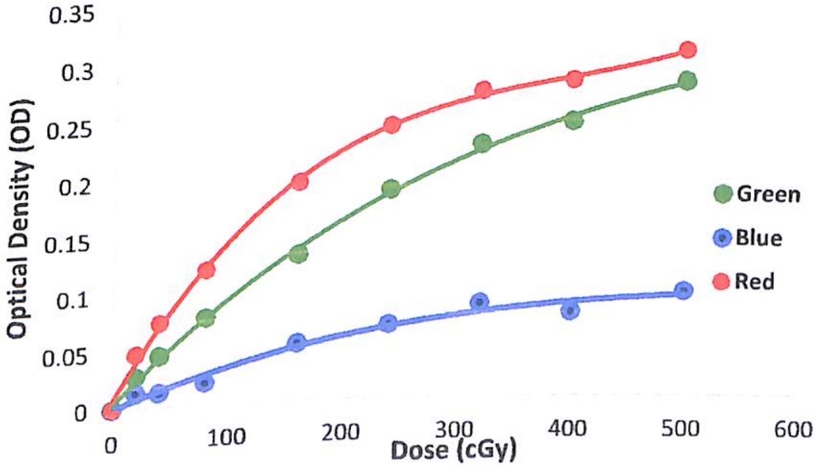

Figure 38: Characteristic curve of EBT3 Film for 1.25 MeV beam energy from cobalt machine.

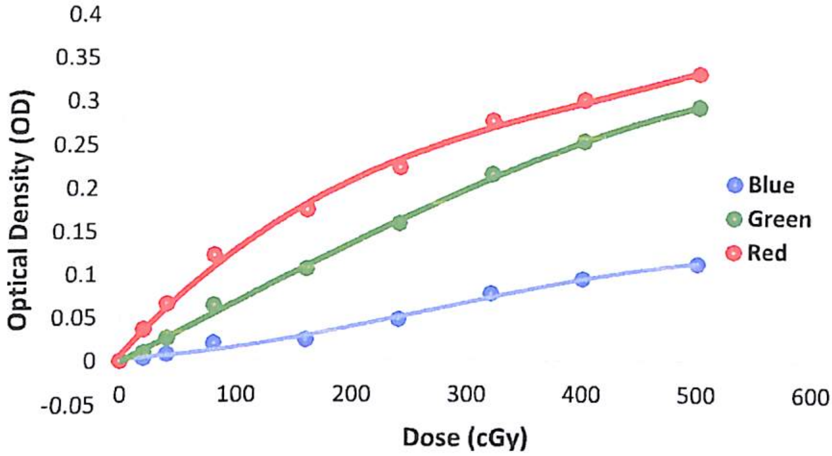

Figure 39: Characteristic curve of EBT3 Film for 6 MV beam energy of linear accelerator.

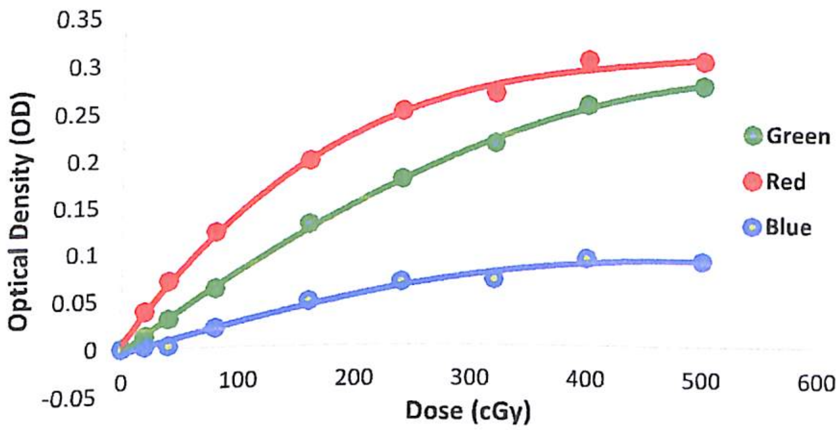

Figure 40: Characteristic Curve of EBT3 Film for 15 MV beam energy of linear accelerator.

The relationship between the dose and optical density in Figures 38 - 40, showed a non-linear curve and that each curve of the response curves was different in colour, with each signal comprising of dose-dependent and dose-independent portion. It was observed from Figures 38 - 40, that the sensitometric curves for the beam energies of 1.25 MeV, 6 MV and 15 MV of the EBT3 radiochromic film scanned in the red and green channels are above the response curve of the films scanned in the blue channel. These results are consistent with those obtained for the EBT radiochromic film experiment by Devic et al. (2009).

The sensitometric curves for the red channel showed a higher sensitivity and a more rapid saturation than the blue and green channels. The response behaviour of the EBT3 film to radiation could be attributed to the absorption spectrum of the active layer, which exhibits maximum absorption at approximately 635 nm, that is the red spectrum of visible light. Additionally, the green visible spectrum falls within a lower absorption peak centred at approximately 583 nm. Also, the response of the EBT3 film in the blue channel was below the response of the red and green channels. This was because the absorption peaks found in the blue part of the visible spectrum are very small (Devic et al., 2007; Devic et al., 2010; Marroquin et al., 2016). Therefore, X-ray radiation produces a change in its visible light absorption spectrum and optical properties, making the films suitable for dosimetric applications.

It should be noted that the response curves depend on the dosimetry system which includes the type of radiochromic film, a flatbed scanner, and a dosimetry protocol. Additionally, the sensitivity depends on the colour channel with which the films are scanned. Consequently, the red channel pixel values obtained from the calibration curves were used for further image analysis, because it showed a higher sensitivity and response.

Optical Density and Dose

Figure 41, shows the correlation graph for dose and optical density for the three energy beams used in the study. The 4^{th} order polynomial was used to interpolate the dose for each piece of the film. These curves represent the film response as a function of the dose delivered to the film. Table 19 also, shows the regression analysis of the plots. The graphs in Figure 41 agrees with the graphs of film response curves by Pai et al. 2007 in Figure 10 (Chapter Two).

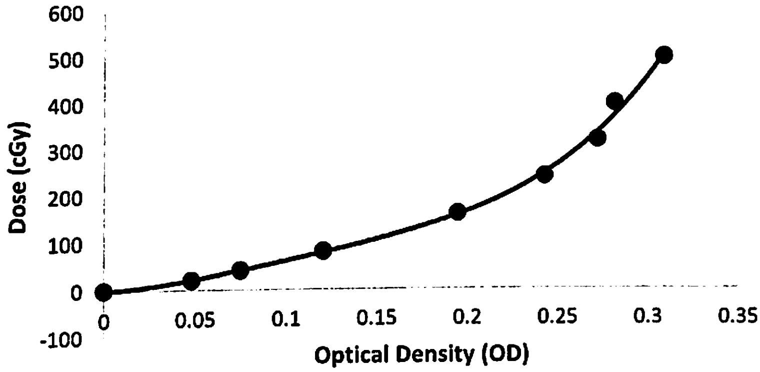

(a)

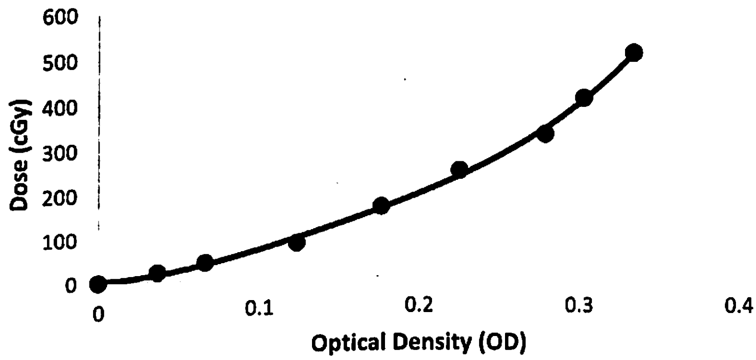

(b)

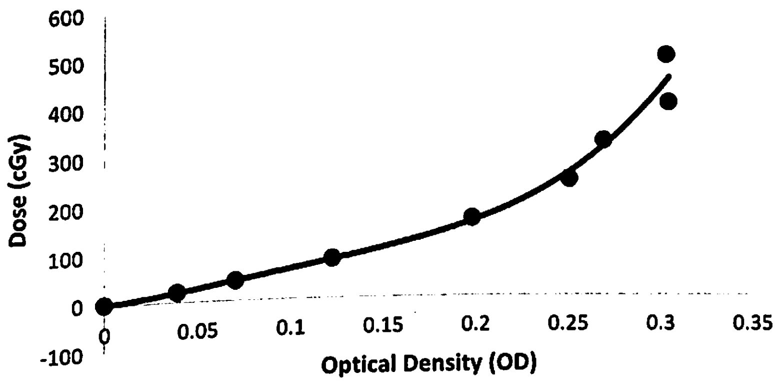

(c)

Figure 41: Relationship between optical density and dose from different energy sources: (a) 1.25 MeV, (b) 6 MV, (c) 15 MV.

Table 19: Summary of the Polynomial Regression Analysis for the RGB Channels

	1.25 MeV		
Characteristic	Red	Green	Blue
Coefficient of Determinant, R^2	99.8%	99.8%	97.5%
Standard Error, σ	0.0057	0.0052	0.0071
p-value	1.0164E-04	1.7215E-06	3.4500E-05
	6 MV		
Coefficient of Determinant, R^2	99.6%	99.8%	99.1%
Standard Error, σ	0.0096	0.0056	0.0051
p-value	1.0975E-05	1.5489E-08	1.3900E-07
	15 MV		
Coefficient of Determinant, R^2	99.8%	99.9%	98.4%
Standard Error, σ	0.0069	0.0039	0.0061
p-value	1.4173E-04	1.1212E-06	2.0496E-05

Source: Field Data, 2018

These values shown in Table 19 indicate that, the regression curve fits the data perfectly. The R^2 indicates variation of the RGB channels, and the higher R^2 values describes that the data fits model. The estimated standard deviation, of the error in the precidition was almost zero for all the channels. Additionally, the probability of obtaining the actual calculated value denoted as the p-value was zero, which is in the cut off value of 0.05. The estimated regression of the relationship between the response variable (dose) and the predicator (OD) were given as:

For 1.25MeV

$$D = 127229x^4 - 51326x^3 + 8585.9x^2 + 142.98x - 0.5286 \tag{37}$$

For 6 MV

$$D = 60363x^4 - 32980x^3 + 8518.4x^2 + 65.397x + 2.8946 \tag{38}$$

For 15 MV

$$D = 103240x^4 - 37335x^3 + 5583.7x^2 + 339.86x - 0.0754 \quad (39)$$

where D is the absorbed dose and x is the measured optical density. Equation (37), (38) and (39) were used to calculate the absorbed doses delivered to the phantoms from the measured optical densities of the film.

In summary, the optical densities increase with increasing dose of the irradiated films. Therefore, the number of photons reaching the film determines how dense the film becomes and is a function of the intensity of the radiation and the length of time that the film is exposed to the radiation.

Energy and Film Response

The variation in the film response due to different dose values was studied with the three photon energies of 1.25 MeV, 6 MV and 15 MV. A graph of correlation was plotted for the beam energies with their respective red channels. Figure 42 shows the energy dependence on the EBT3 film.

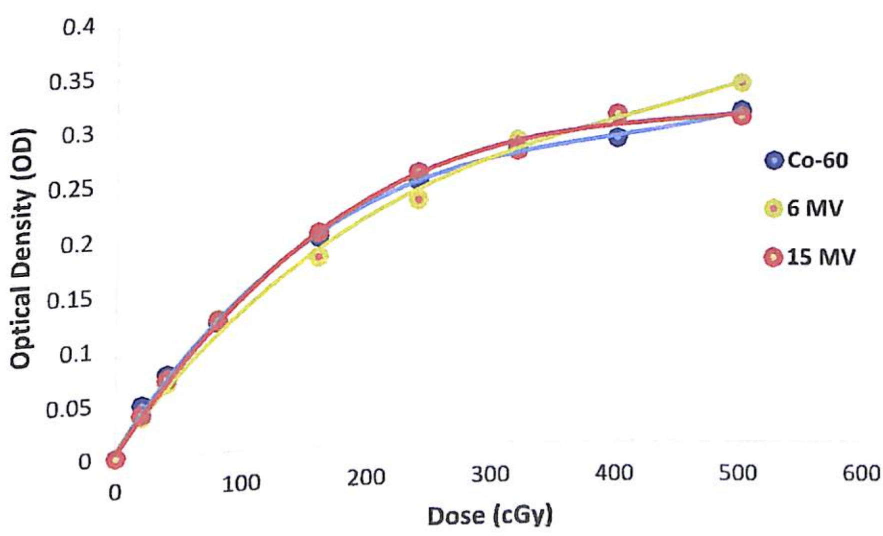

Figure 42: Energy dependence of EBT3 film.

The coefficient of determination (R^2) value for 1.25 MeV, 6 MV and 15 MV were 0.9978, 0.9962 and 0.9984 respectively. The EBT3 film showed the same dosimetric response to the photon energies used. According to Reinhardt

(2012), EBT3 films have no dependence on the radiation type for photon except for protons in the proximity of the Bragg peak. Based on the graph it is confirmed that EBT3 film has low energy dependence as specified by the manufacturer. Additionally, Figure 42 showed a small energy dependence over a range of the beam energies used as described by Butson et al., 2006; Chiu-Tsao et al., 2005; Lindsay et al., 2010; Arjomandy et al., 2010b; Kirby et al., 2010. The optical densities of the different beam energies in relation to the doses exposed to the EBT3 films are shown in Appendix F. Also, in Figure 43, it was observed that the optical densities increased with increasing doses.

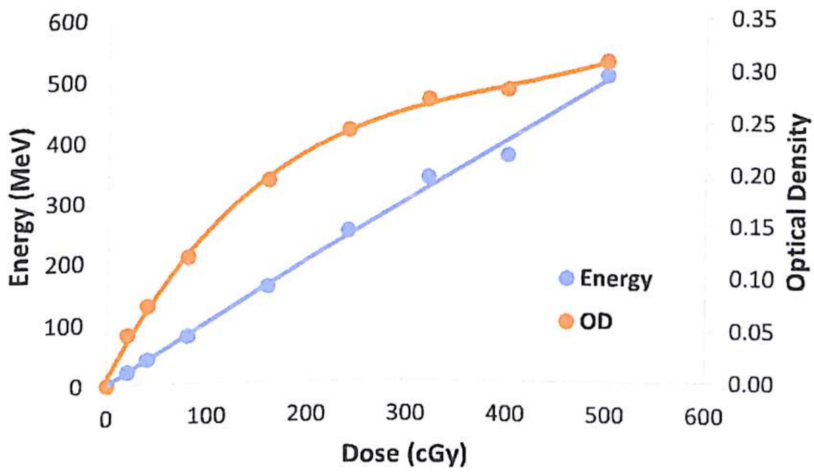

(a)

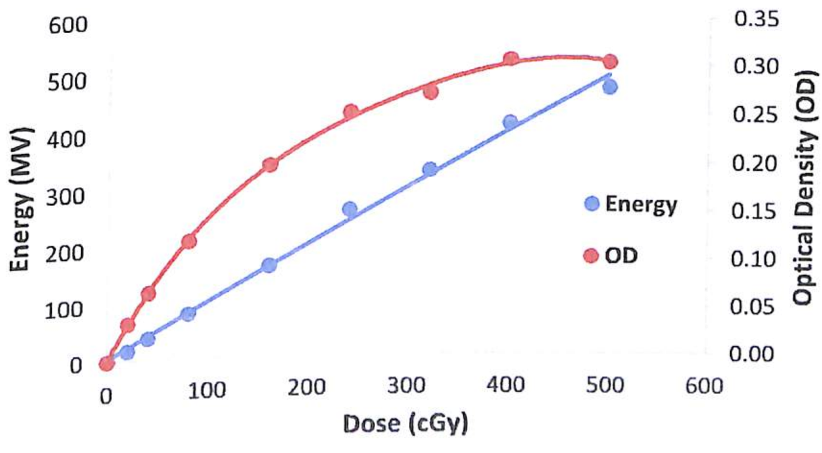

(b)

Figure 43: Relationship between dose, optical density and energy: (a) MeV; (b) MV.

The highest optical density was achieved (Figure 43) when the EBT3 film was exposed at a higher dose of 500 cGy for the various beam energies used. According to Borca et al., (2013), optical density of EBT3 films changes stability rapidly of two hours waiting time, and the dose response should be within 1.5% uniformity (Reinhardt et al., 2012). Again, Brown et al., (2012), in their investigation in the dose response curves of radiochromic films of EBT, EBT2 and EBT3 stated that EBT3 showed a weak energy dependence over an energy range of 25 keV–4 MV.

In summary, the EBT3 film showed almost the same dosimetric response to the photon energies used in this study. The energy beams used for this study are independent on the radiochromic film as shown in Figure 44.

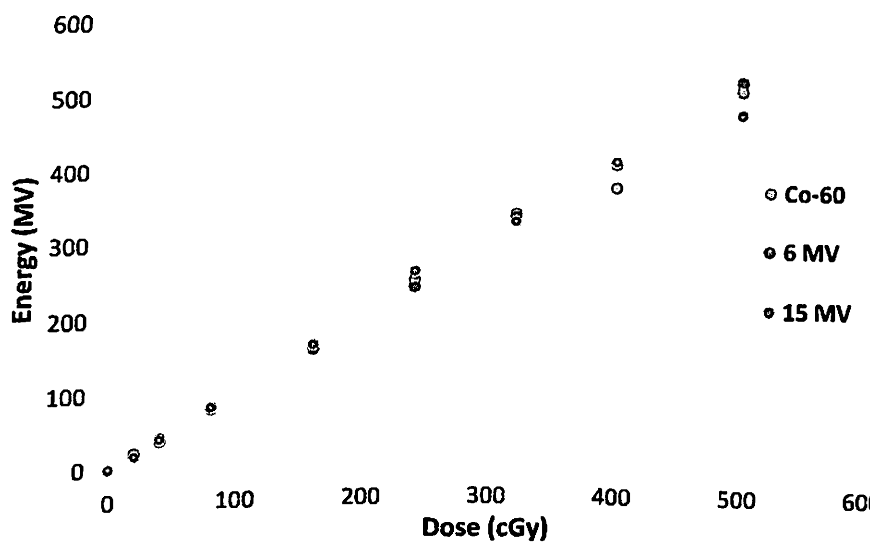

Figure 44: Relationship between energy and dose.

In addition, it was observed from Figure 44 that, the doses for the various energies were almost the same for dose values up to 200 cGy, until there were slight differences as the doses increased. However, the energies were dependent on the doses delivered.

Dose and Film Area

The optical density and the selected area of the EBT3 film were assessed. These were done to measure the scanning region of the EBT3 film.

The mean pixel value in the central area of 10 x 30 mm^2, 20 x 40 mm^2, 30 x 50 mm^2, 40 x 60 mm^2 and 50 x 70 mm^2 regions were measured. Table 20 shows the relationship between the dose and the area of each of five irradiated regions.

Table 20: Relationship between Dose and Area of the Different Film Sizes

Measured Dose (cGy)	Calculated Dose (cGy) for Area (mm^2)				
	10 x 30	20 x 40	30 x 50	40 x 60	50 x 70
0	0	0	0	0	0
20	23.5422	21.3652	20.1264	19.9750	17.2018
40	39.9473	39.3407	39.3655	38.1183	37.2729
80	79.6650	80.4149	80.2144	77.5904	74.6033
140	152.8622	156.0895	154.7339	154.8076	108.9704
160	152.3647	157.5844	159.7078	157.4514	155.8887
320	303.1923	329.2890	333.8496	331.2030	294.8027
400	370.8863	375.2948	371.7493	371.7213	313.4481
500	504.6336	499.1611	509.1430	486.6558	488.9696

Source: Field Data, 2018

From Table 20, the area of 40 x 60 mm^2 of the film was selected from the five measurements regions. This was because the area selected was within the exposed region, and large enough to give a good statistical representation. Penumbra effects were also avoided near the edges of the irradiated squares (Matney et al., 2010) based on the area selection. The percentage error δ, was calculated for the area selected for the measurements. Table 21 shows the percentage error of 40 x 60 mm^2 region of interest.

The error δ between the measured dose $D_{measured}$ and the expected dose $D_{expected}$ was calculated using equation (36) from Chapter Three. δ was calculated for each measurement to estimate the difference between the actually measured, and the calculated dose at the central beam. The highest and lowest mean dose discrepancy (δ_{mean}) calculated was 0. 13% and 4.94% respectively, which were within the tolerance of ±5%.

Table 21: Error of Measured and Calculated Doses for ROI

Expected Dose (cGy)	Measured Dose (cGy)	% Error ($\|\delta\|$)
0	0.0000	0.0000
20	19.9750	0. 1252
40	38.1183	4.9363
80	77.5904	3.1055
140	154.8076	3.3200
160	247.4514	1.6187
320	331.2030	3.3825
400	371.7213	4.7885
500	486.6558	2.7420

Source: Field Data, 2018

GafChromic EBT3 Film Orientation

The optical properties due to scanning orientation of GafChromic EBT3 film, was assessed. This was done to test for variations in measured relative optical density, due to the films orientation relative to the scanner direction. Therefore, the effect of the film orientation on the scanner output for a given dose of eight dose levels were estimated in this study. The film pieces scanned in landscape and portrait orientations were extracted from an area of 40 mm x 60 mm ROI at the centre of each image. Figure 45 shows a plot of the scanning values for each orientation.

The effect of the film orientation was expressed as a percentage difference from portrait and landscape orientation given as:

$$\% \text{ diff} = \frac{\mu_L - \mu_P}{\mu_P} \quad (44)$$

where μ_L and μ_P are the optical densities of the EBT3 film responses at each dose region in landscape and portrait orientation respectively. Table 22 shows the percentage difference of the film orientations.

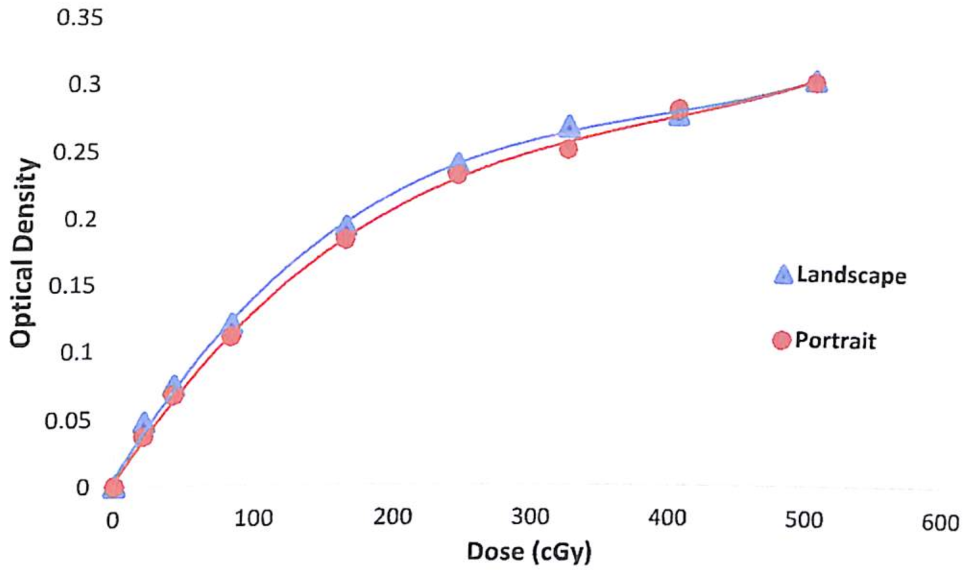

Figure 45: Scanning orientation of EBT3 Films.

Table 22: Percentage Difference of Film Response between Landscape and Portrait Orientations

Measured Dose (cGy)	Calculated Dose (cGy)		
	Landscape	Portrait	% Difference of Film Orientation
20	21.0964	14.2261	0.4829
40	40.7122	35.1003	0.1599
80	78.3936	70.0283	0.1195
160	156.8162	143.6018	0.0920
240	247.5115	227.5382	0.0878
320	336.4911	278.5127	0.2082
400	390.6080	373.3774	0.0461
500	506.1412	496.3996	0.0196

Source: Field Data, 2018

The measured largest difference with the Epson Stylus scanner was 0.4829, while the smallest percentage difference observed was 0.0461. From Table 22, it was realized that the scan response of the EBT3 films was sensitive to the orientation of the film on the scanner. The EBT3 film showed a different response between portrait and landscape orientation. The landscape doses calculated were closer to the measured doses, compared to the portrait orientation. This behaviour results from the anisotropic scattering of the photons emitted by the scanner when passing through the polymer network, and the polarization of the transmit light by the needle-like shape particles of film active component. The landscape orientation, preferentially recommended by the manufacturer was used throughout the study. This was done by aligning the film parallel to the direction in which the film was coated.

It was observed that EBT3 film showed a difference of 0.48 % between portrait and landscape orientation. The study results also showed a lower dependence to those published for EBT2 by Andres et al. (2010) of range approximately 7%–9%, which is greater than that of what Desroches et al. (2010) published to be approximately 2%. The differences in film face-up and face-down scan orientation were negligible in the study because of the symmetric structure of the EBT3 film.

In summary, the EBT3 film could be scanned with either side facing the light source. In the measurement and analysis of calibration of EBT3 films, one choice of orientation should be used for the dose assessment.

Scanners of GafChromic EBT3 Films

The study quantified the performance and evaluated a flatbed scanner, Epson Stylus CX5900 used for scanning the radiochromic EBT3 film dosimetry and two other widely used commercial scanners (Scanner A and Scanner B). The performance of each scanner was based on constancy and uniformity. The scanners were tested using films irradiated with doses ranging from 0 - 500 cGy. Image J software was used for analysing the scanners. Figure 46 shows a graph plots of the three scanners used in the study.

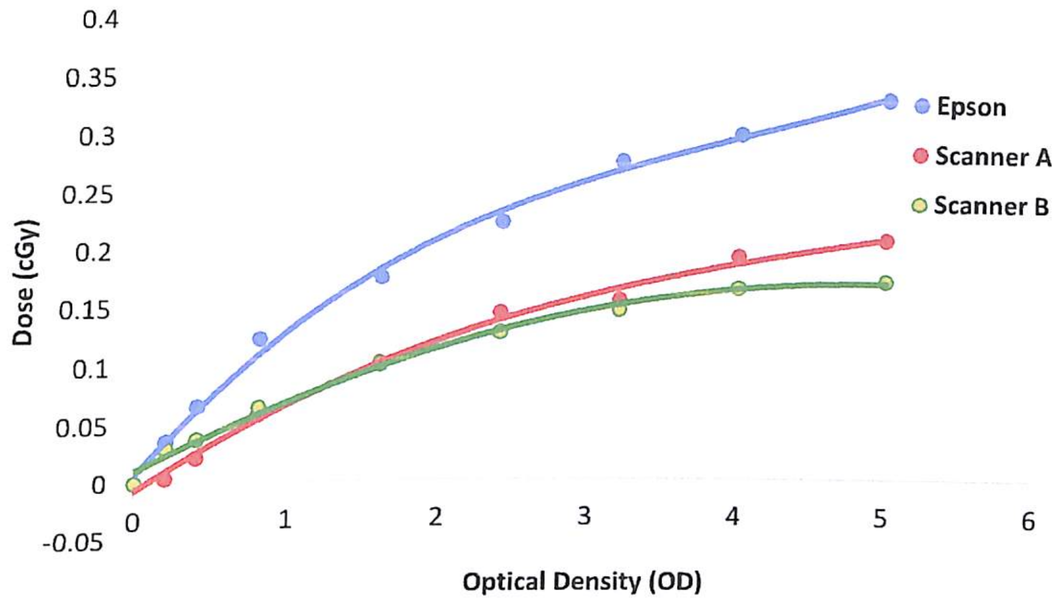

Figure 46: Different types of scanners and dose.

It was observed from Figure 46 that, the Epson Stylus CX5900 used for the study showed the greatest response, while Scanner B showed a relatively lower response. Currently, the suggested film scanner of EBT3 by manufacturers is a flatbed RGB scanner, because of its ability to produce data response in three colour channels. Furthermore, studies conducted by Paelinck et al., (2007) and Wilcox & Daskalov (2007) has also been suggested by the manufacturer of radiochromic film that a high quality flatbed document scanner might even be superior to the traditional scanners. Although the RGB scanner is recommended for scanning, the dose range by the Epson Stylus used was similar to the RGB scanner. Table 23 shows a comparison of the scanners used in the study.

Epson scanner was used for the image analysis, because of its inherent features and its similarity to that of the RGB scanner its better. Table 23 was compared with studies performed by Farah et al. (2014) They performed an experiment with the Varian TrueBeam 1.6 accelerator using flatbed EPSON

10000 XL and HP Scanjet 4850 in reflection mode to compare the EBT3 film responses of doses up to 500 cGy for both photons and electrons (Farah et al., 2014). They concluded that, the reflective scanning method could be used on EBT3 as an economic alternative. In addition, the behavior for doses ranging from 0 to 40 Gy corroborated the results reported by Borca et al. (2013) for EBT3 film.

Table 23: EBT3 Film Scanning Parameters

Scanners	Epson Stylus Scanner (this study)	Scanner A	Flatbed RGB Scanner (Recommended)
Image Type	24 bit Colour	48bit colour	48 bit colour
Resolution	72 dpi	600x600dpi	75 dpi
Colour Corrections	None	Colour	None
Auto Exposure Type	Photo	Photo	---
Document Type	Reflective	No Transparency	Transparency
Scan Mode	Professional	Professional	Professional

Source: Field Data, 2017

The percentage error (δ) was estimated for the measured dose and the expected doses for Epson Stylus CX5900 Scanner. Table 24 shows the results of the measured doses for repeated (three times) scanning using the same film for the measurement.

The results of the consistency for the Epson Stylus CX5900 scanner, shows a standard deviation expressed as a percentage of the different measured film responses of mean doses. The average dose discrepancy (δ_{avg}) calculated was 0.65% and its standard deviation (σ) of 0.92. The percentage error calculated was between 0. 13% and 3.32%. The standard deviation ranged from 0.02 to 3.40. This value might be as a result of lack of uniformity in the scan area, the scanner stability, and the response of the film on orientation dependence (Devic et al., 2009; Bouchard et al., 2009; Renade et al., 2008; Martisikova et al., 2008; Paelinck et al., 2007). The average percentage error for the study measurement was within 1% uniformity as reported by Borca et al. (2013).

Table 24: Epson Scanner Response to Doses

Expected Dose (cGy)	Measured Dose (cGy)	% Error ($\lvert\delta\rvert$)	Standard deviation (σ)
0	0	0	0
20	19.9750	0. 1252	0.0177
40	39.1183	2.2538	0.6234
80	77.5904	3.1055	1.7038
140	144.8076	3.3200	3.3995
160	157.4514	1.6187	1.8021
320	321.2030	0.3745	0.8506
400	395.7213	1.0812	3.0255
500	496.6558	0.6733	2.3647

Source: Field Data, 2018

In summary, the Epson Stylus scanner used for the study was appropriate in scanning EBT3 films. The scanner used proved to be reliable and accurate for film dosimetry. Therefore, the type of scanners to be used in reading the EBT3 films is important because different scanners used might not be sensitive to the EBT3 films and might introduce errors in the measurements of low doses. The scanner should be warmed-up in order for it to reach an invariable temperature and avoid scanner fluctuations (Xu, 2009). Th is could be attained by turning on the scanner and performing several blank scans.

Scanner Uniformity

A uniformity test was conducted on the Epson flatbed scanner used in scanning the EBT3 films. The films used were scanned at fifteen different positions on the scanner. It was measured by evaluating the horizontal and vertical positions through the central axis of an unexposed EBT3 film. Table 25 shows the film variation in the different positions on the scanner. Where the mean is the average pixel values generated by the ImageJ software for each film scanned, the integrated density (IntDen) is the product of area and mean gray value, and raw integrated density (RawIntDen) is the sum of the values of the pixels in the image or selection. IntDen and RawIntDen values are the same for un-calibrated image.

Table 25: The Mean Pixel Values and Standard Deviations of the EBT3 film at Different Positions on the Scanner of Area 2400 mm^2

Position	Mean	Standard Deviation	Integrated Density	Raw Integrated Density
1	89.675	0.807	215221	215221
2	86.230	1.156	206952	206952
3	85.693	1.142	205663	205663
4	86.161	1.099	206786	206786
5	88.840	1.029	213217	213217
6	85.504	0.698	205209	205209
7	88.118	0.836	211483	211483
8	89.095	0.824	213827	213827
9	87.119	0.816	209086	209086
10	87.508	1.194	210020	210020
11	90.096	1.004	216231	216231
12	85.974	1.304	206338	206338
13	87.547	1.039	210113	210113
14	85.841	1.112	206019	206019
15	86.056	0.934	206535	206535

Source: Field Data, 2018

The different scanning positions had different optical densities as shown in Table 25. Position 11 measured the highest mean pixel value of 90.10, with standard deviation of 1.00, while position 6 measured the lowest mean pixel value of 85.50 of 0.70 standard deviation. The average pixel values and standard deviations of the fifteen scanner position measured were 87.30 and 0.99 respectively. The measurement of the mean pixel values obtained in Table 25, shows a non-uniformity across the film scanner. This confirms the film non-uniformity as per the manufacturers specifications. Figure 47 shows a plot of the optical densities of each of the fifteen positions.

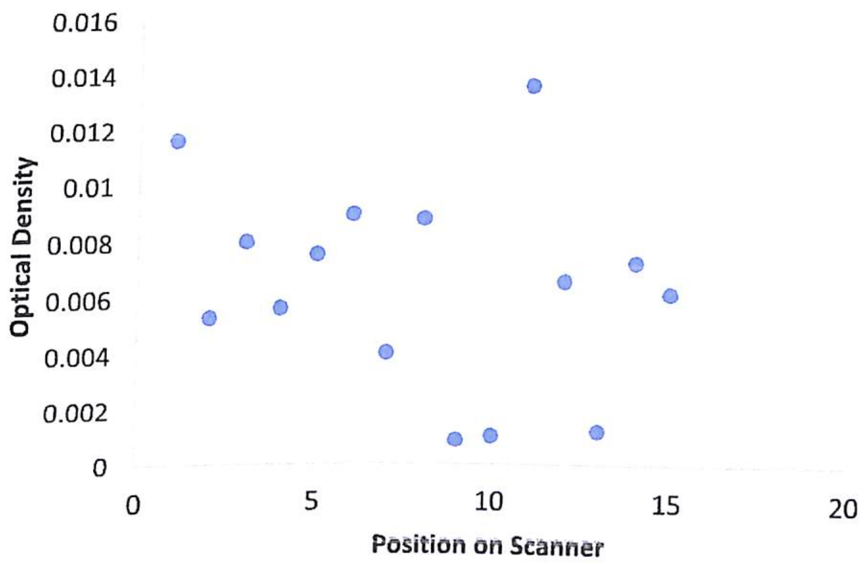

Figure 47: Scatter plot of optical density and scanner position of the EBT3 films.

The optical densities values ranged from 0.0012 to 0.0137 with standard deviation of 0.004. From Figure 47, it was observed that position 11 had the highest optical density, while position 9 had the lowest. Position 9, 10 and 13 were below 0.002. Most of the optical densities were within 0.004 and 0.010. Only two films had their optical density greater than 0.010. The Epson Stylus CX5900 scanner showed a non-uniformity.

In summary, it is recommended that the EBT3 films are positioned in the centre of the scanner in the direction perpendicular to the scan direction to minimize effect of lateral response artefact.

Results of Virtual Simulation

The results of the Cobalt-60 geometry simulation described in chapter three is presented in this section. The energy distribution within the vir tual phantom is presented. Figure 48 - 50 show the results of the spatial distribution per photon in the z plane using MATLAB which was sectioned into ten layers representing the different distances from the surface with each layer having 25,000 voxels (tissues).

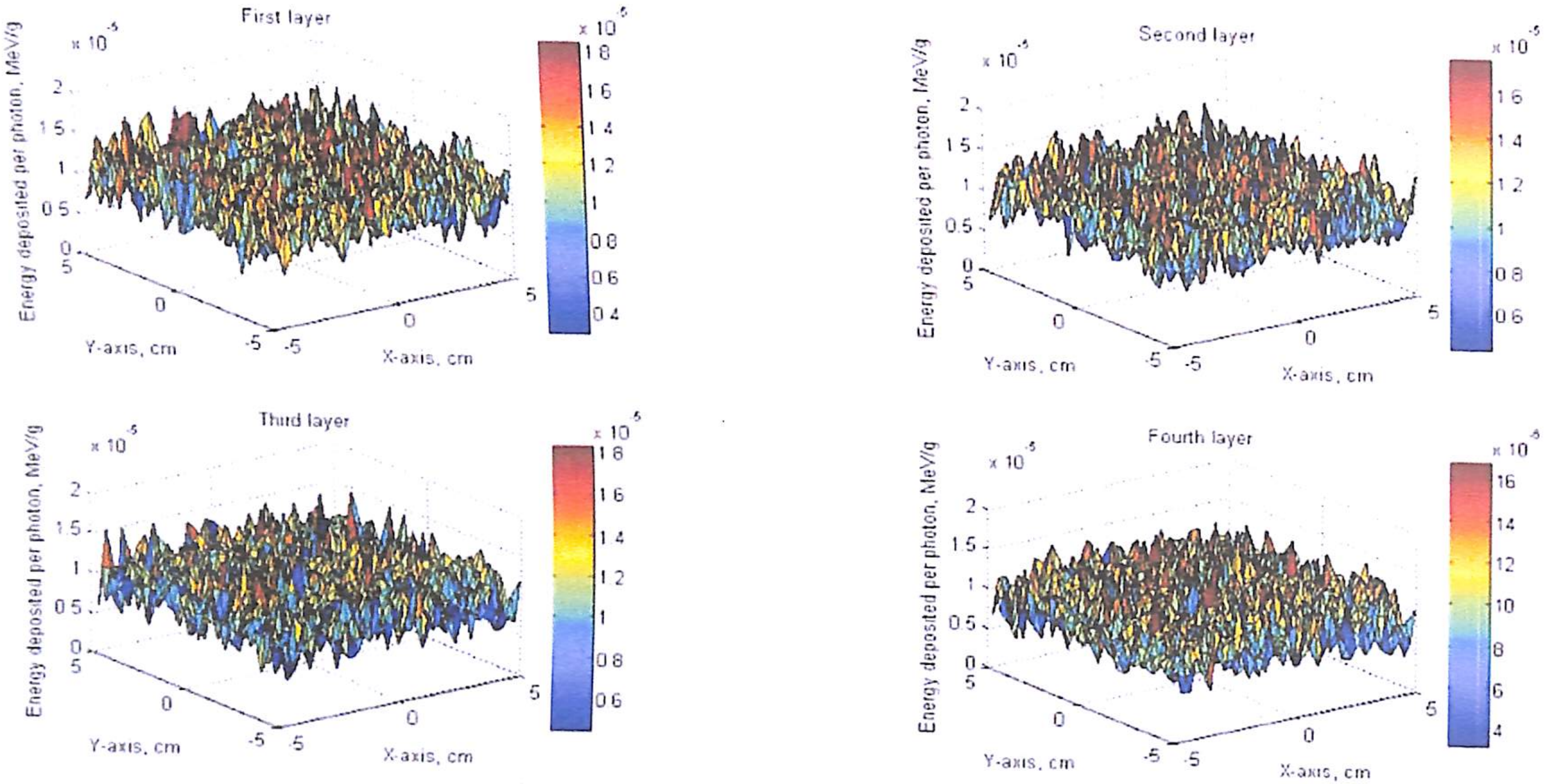

Figure 48: Energy deposition at the first to fourth layers.

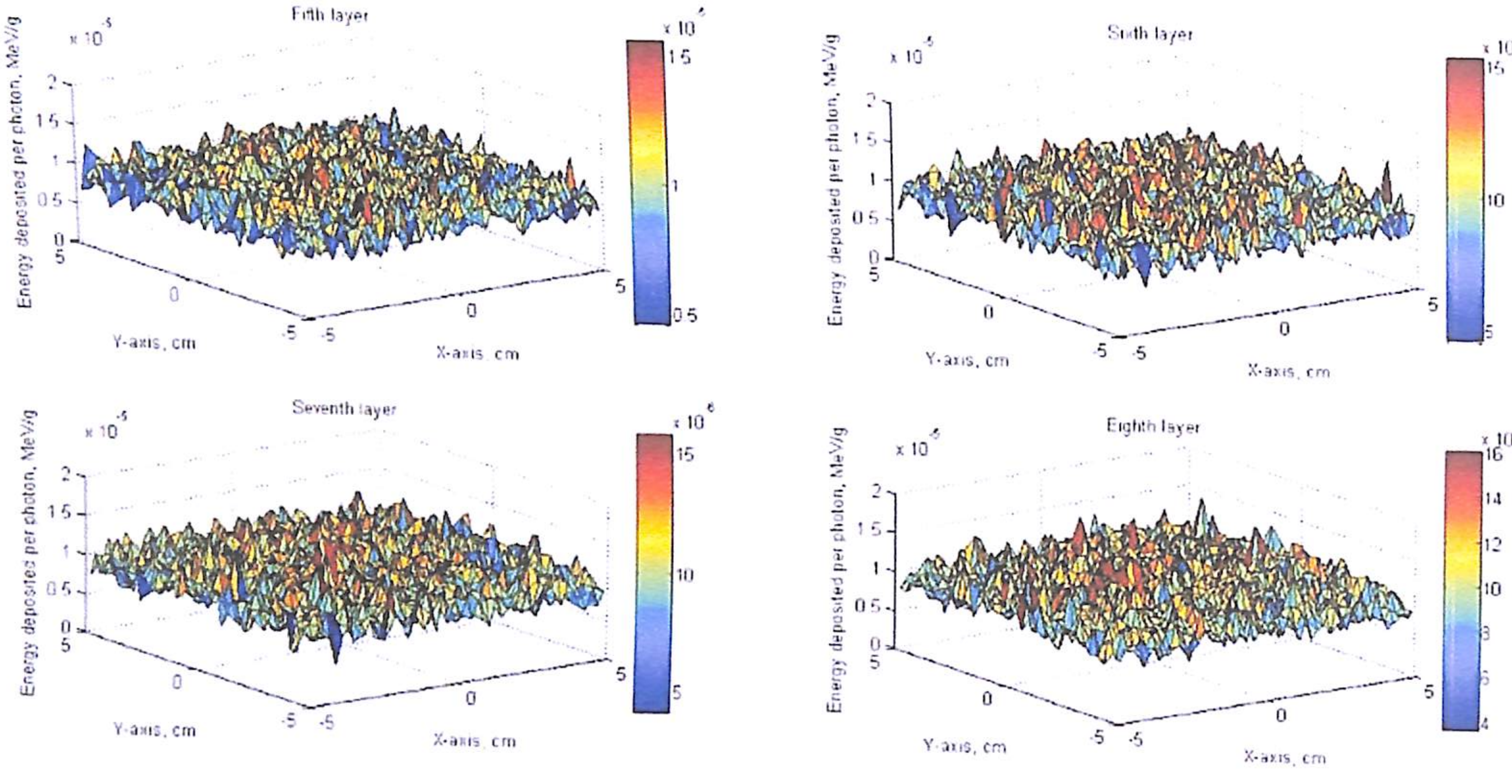

Figure 49: Energy deposition at the fifth to eighth layers.

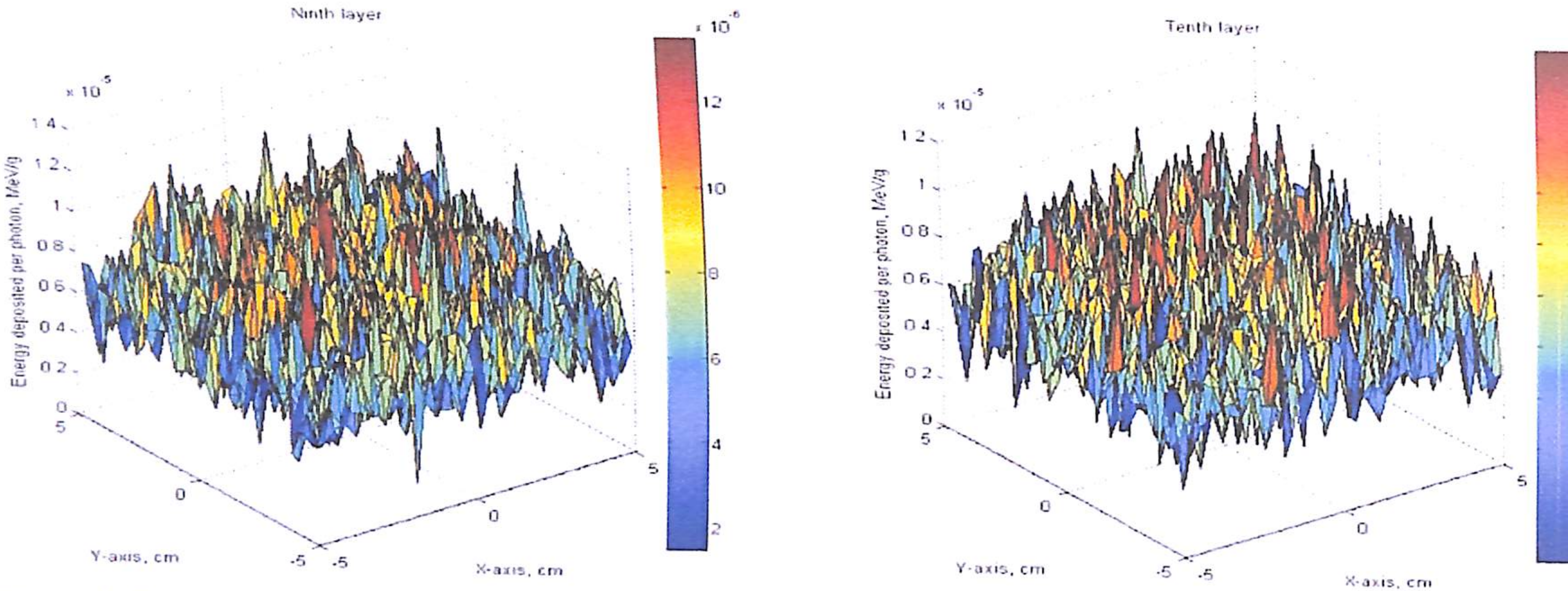

Figure 50: Energy deposition at the ninth and tenth layers.

From the results it was observed that the first layer in the MCNP corresponded to the energy deposited per photon in the tenth meshed layers using MATLAB. The highest peaks in each of the layers show where the maximum dose was absorbed and achieved. The model computed the dose in each voxel in each layer by transporting several millions of particles based upon probability theory of interaction with the virtual phantom mimicking the patient. This is because radiotherapy involves finding the precise location of a tumour and optimizing the intensity of the radiation and the orientations of the beams shaped to match the plan delineation of the tumour.

Based on the results from the simulation, a non-linear response equation was generated of which it was used to deduce the radiation dose. Figure 51 shows a correlation graph which indicates the non-linear relationship between the response variable (relative absorbed dose) and the predicator (layer number) representing the different distance from the surface within the virtual phantom.

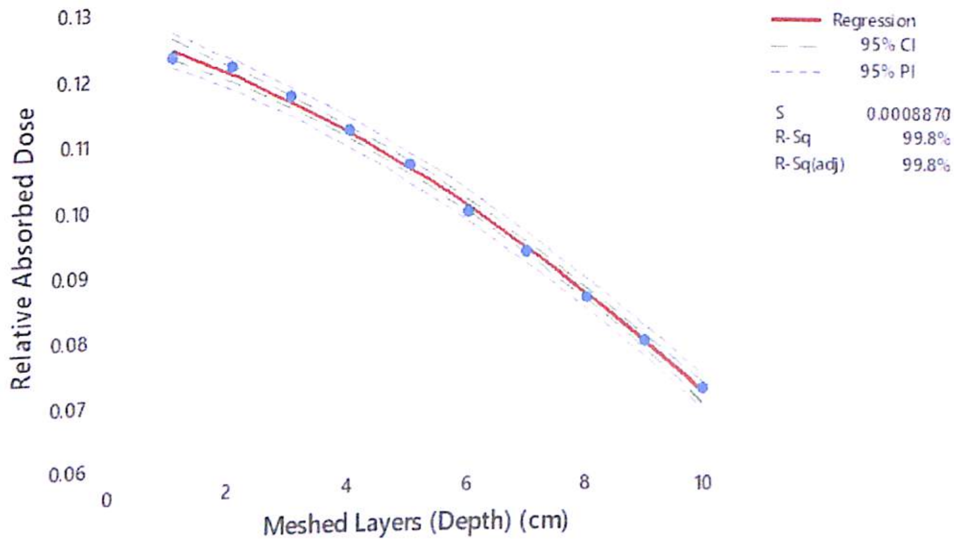

Figure 51: Relative absorbed dose in each meshed layer.

In Figure 51, the graph gives information on the goodness of the model. The coefficient of determination (R^2) value of 99.8% indicates that the regression line fits the data with the significance value ($p < 0.050$) less than indicating strong evidence of the model as shown in Table 26.

Table 26: ANOVA for the MCNP Model

	Degree of freedom (DF)	Sum of Squares (SS)	Mean Square (MS)	F	p-value
Regression	2	0.0030695	0.0015348	1950.61	3.928E-09
Residual	7	0.0000055	0.0000008		
Total	9	0.0030750			

Source: Field Data, 2018

Table 26 was used to partition the variation in the observed values. The significant p-value of 0.000 indicates that, there exists significant relationship between meshed layer (distance) and relative absorbed dose. Again, the graph shows the estimated regression model of the relationship between the relative absorbed dose in each layer within the virtual phantom using Co-60 teletherapy machine. Equation (40) shows the estimated regression model of the relationship between the relative absorbed dose and the meshed layers. The equation is given as:

$$Relative\ Absorbed\ Dose = -0.002x^2 - 0.0035x + 0.1283 \tag{40}$$

where x is the distance from the source to the phantom for the irradiation for therapy. The layers represent the summation of all the different points located in the different direction within a particular section of the phantom.

The standard deviation, σ, was 0.0009, which is considered reliable for dose calculation because it is below 5%. For this study the transport of 10^7 photons sources was simulated in order to get a reliable estimation of the absorbed dose.

From Figure 51, the first layer received the highest/maximum absorbed dose while the tenth layer received the lowest dose signifying that, as the photon energy with shorter wavelength passes through the material, the doses at different distances from the surface also change. The different layers did not absorb the same dose. The non-uniformity of radiation distribution within the virtual phantom might have resulted in the size, location, and composition variations. The absorbed dose was greater at the entrance surface than those deeper within the phantom. Therefore, it could be stated that for a given photon, it absorption is dependent on the penetration ability, on the density of material to be used and the size of the exposed area.

Additionally, the simulation model was able to calculate the set of radiation intensities that pass through the phantom for a desired dose distribution mimicking exactly what happens to patient during treatment. This was verified through experimental measurements. The experimental results obtained with the same setup (as shown in Figure 35), showed a non-uniformity of the doses at different depth, as the depth increase the dose recorded was lower with standard deviation of 0.0075. Figure 52 shows the correlation graph of the absorbed dose with depth.

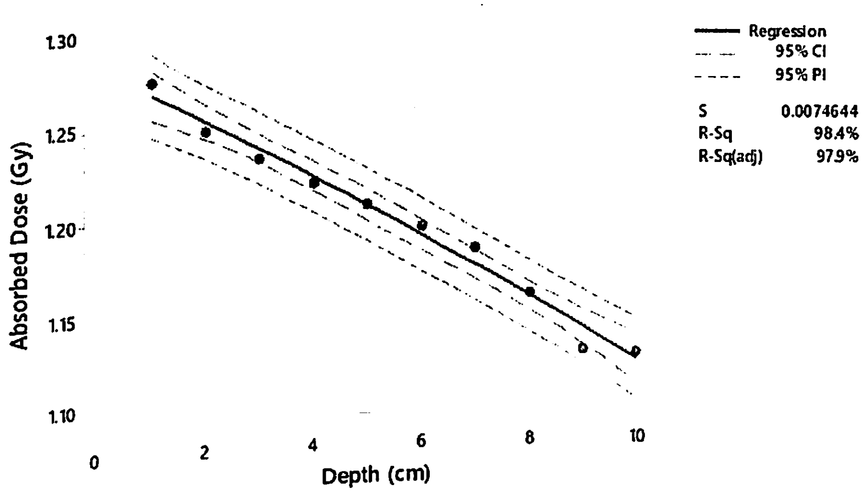

Figure 52: A graph of absorbed dose and depth.

In summary, the dose distribution estimated to the various layers within the phantom (virtual) is useful for predicting the therapeutic value in determining the safety treatment outcome for the patient represented by the virtual phantom. It is therefore necessary to precisely know the dose deposited at any point within the body of a patient during radiation therapy as part of dose optimization. The Monte Carlo used for the simulation ensured the estimated dose precision in the therapy of cancer with radionuclides as reported by Sonia and his colleagues (Sonia et al., 2006).

Dose Validation

This section discusses the measured absorbed doses and the expected doses for the verification. Its includes the Hounsfield Units determined for the local materials, ionization chamber measurements, the results of the anthropomorphic and the Adelaide phantoms measurements.

Tissue Characterization

Tissue mimicking materials play a key role in dose caculations for TPS and for absorbed dose estimates in radiographic imaging studies. Therefore, the study investigated the relationship between the linear attenuation coefficient and the HU for the materials used for the tissue substitutes for the phantom. The quantitative data of Hounsfield Unit determined using the Emotion CT Scanner for the tissue densities is presented in Table 27.

From Table 27, balloons, mango seed, candle and cassava stick were used to represent and mimic the lung, muscle, fat and bone respectively in the thoracic region of the Adelaide phantom. The HU of these materials selected were compared to HU determined by Dance et al. (2014), Buzug (2008), Heymsfield (2005), Prokop (2003). It was observed that, most of the HU values were within the tissue density range except mango seed which had an HU of +50.3, which could be a factor of temperature or tube voltage from the CT scanner. According to Dance et al., (2014), the actual value of the Hounsfield unit (shown in Table 4) is depended on the temperature, composition of the tissue and the tube voltage.

Table 27: Hounsfield Units of Local Materials used in the Study in Comparison with HU for Human Tissues

Tissue substitutes	HU*	HU**	HU***
	Lung Tissue		
Balloon	-999.7	-1000	-1000
Bottle	-1001.1		
Foam	-980.4		
	Muscle Tissue		
Clay	+1345.0	+10 to +50	---
Mango seed	+50.3		
Cork	+683.0		
	Bone		
Plaster of Paris (POP)	+430.0	+1000 to +2500	+700 to +3000
Cassava Stick	+801.5		
Polyvinyl Chloride (PVC) Pipe + Cotton	-737.9		
	Glandular Tissue		
Candle	-78.5	-100 to -80	-100 to -50
Wax	-124.8		
Egg Shell	-188.4		
Rice	-115.65		

Source: *This study; **Dance et al., 2014; ***Buzug, 2008; ***Heymsfield, 2005; ***Prokop, 2003

Also, from the definition of the HU, it follows that for all substances except water and air, variations of the HU values occur when they are determined at different tube voltages. The different variations in the HU values might be due to the dependence of the various HU values on the following parameters such as reconstruction filter, the size of the scanned field of view (FOV), and the position within the scanned FOV.

The physical densities, linear attenuation coefficients and electron densities derived for the materials inserted in the constructed phantoms are shown in Table 28. The linear attenuation and electron densities were computed using equations (17) and (22) respectively.

Table 28: Radiological Properties of Selected Materials

Materials		Hounsfield Units	Linear attenuation coefficient, $\mu_m(cm^{-1})$	Electron Density/g $\rho_Q = \frac{\mu}{\mu_w}\rho_{Q,water}$
Tissues	Mimicking			
Lung	Balloon	-999.7	0.00002	1.019×10^{20}
Heart	Mango Seed	50.3	0.06879	3.507×10^{23}
Glandular	Candle	-78.5	0.06036	3.078×10^{23}
Bone	Cassava Stick	801.5	0.01300	6.629×10^{22}

where μ_{water} is 0.0655 and $\rho_{Q,water}$ is 3.340×10^{23} per gram
Source: Calculation formula adopted from Claude et al., 2013; Khan, 2003

Different substances exhibit a non-linear relationship of their linear attenuation coefficient relative to that of water as a function of photon energy. The Adelaide phantoms were constructed for the acquisition of patient data for radiotherapy planning. Therefore, the HU and electron density conversions are required by TPS to enable effective correction for tissue heterogeneities in the dose computation within the CT images of the human body. This would also minimize cost of purchasing a commercial phantom.

Validation of Ionization Chamber Measurements

This section presents the measurements results of the ionization chamber, showing the doses from each beam energy used in Table 29. Appendix G, shows the different energies with their irradiation times and doses given.

Table 29: Results of Farmer Type Ionization Chamber Measurement

Dose (Gy) Measured	1.25 MeV	6 MV Calculated	15 MV
0.2	0.1766	0.1883	0.2149
0.4	0.3708	0.3767	0.3981
0.8	0.7504	0.7536	0.7958
1.6	1.4316	1.5086	1.5918
2.4	2.2167	2.2735	2.3887
3.2	2.9767	3.0301	3.1859
4.0	3.6128	3.7856	3.9825
5.0	4.6450	4.7320	4.9862

Source: Field Data, 2018

It was observed from Table 29 that, as the beam energy increases, the dose also increases in the measurements. The absorbed dose delivered varies with the beam energy as well as depth, field size, distance from the source and the beam collimation on the phantom. Therefore, depending on the beam energy the doses also vary. Figures 53 – 55 shows a plot of the measured dose values with the expected dose values. Table 30 also shows the regression statistics of the plot for the beam energies used in this study.

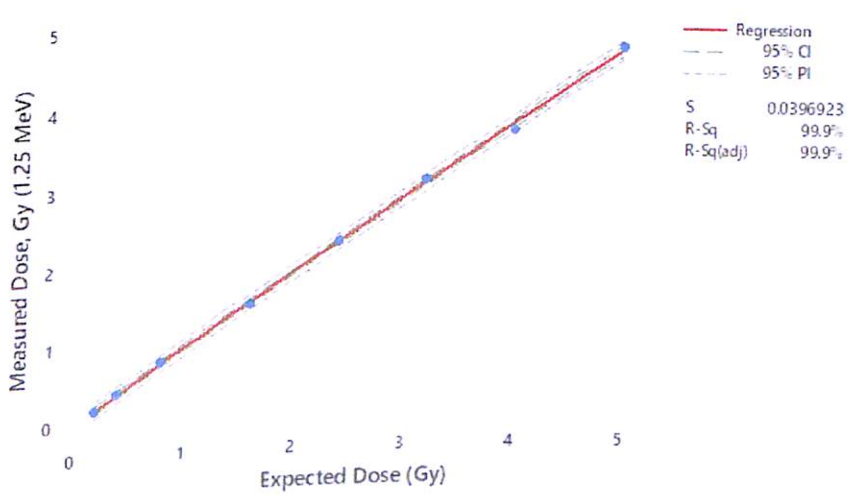

Figure 53: Plot for measured dose versus expected dose for 1.25 MeV.

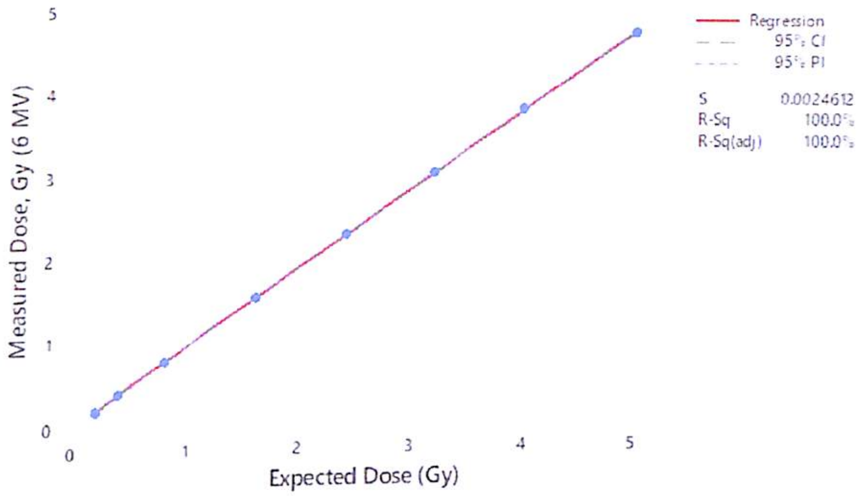

Figure 54: Plot for measured dose versus expected dose for 6 MV.

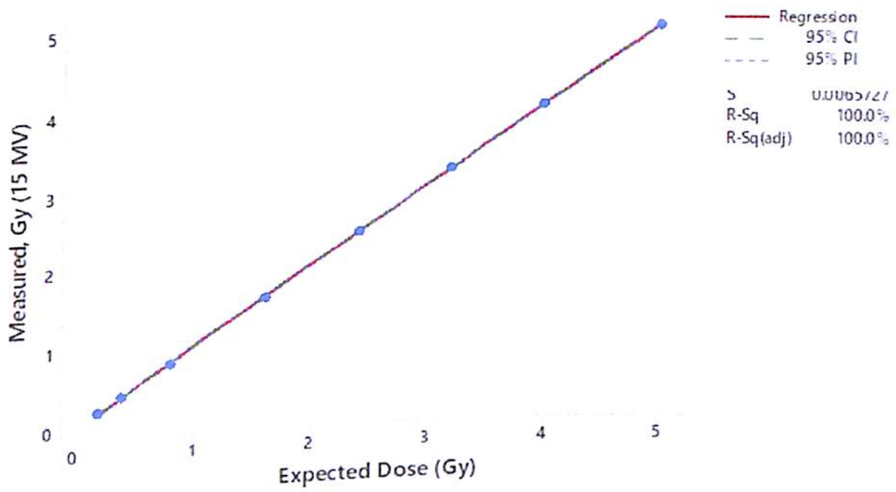

Figure 55: Plot for measured dose versus expected dose for 15 MV.

Table 30: ANOVA of Ionization Chamber Measurements

Energies	1.25 MeV	6 MV	15 MV
Coefficient of determination (R^2)	99.9%	100%	100%
Standard deviation (σ)	0.0397	0.0025	0.0066
p-value	4.1985E-11	2.0394E-18	5.4938E-16

Source: Field Data, 2018

Table 30 shows the significant value of the regression model at a significance level of 0.000 for the three energy beams. The significant value of 0.000 is less than 0.050, which indicates that, there is no difference in the planned (expected) dose and the delivered (measured) doses. The standard deviation values of the plots (Figures 50a–50c) were less than 5%, which is considered reliable for dose calculation.

Validation of Phantom Measurements

The total dose prescribed to the phantoms (Anthropomorphic, Adelaide A and Adelaide B) was 50 Gy per 25 fractions. Therefore, a dose of 2 Gy was delivered five times per week for 25 times. The absorbed dose delivered to the phantoms was expected to be approximately as the prescribed doses. Tables 31 and 32 give the results of the deviation of the prescribed and the delivered doses for each of the phantoms used in the study.

Table 31: Phantom Measurement for LINAC Irradiation

Positions	Expected (Gy)/ Fraction	Anthropomorphic Measured (Gy)	Adelaide B Measured (Gy)	Adelaide A Measured (Gy)
Pt 1 Inside (2B)	2.06	1.17	1.11	1.09
Pt 2 Inside (3B)	2.06	2.14	2.14	2.09
Pt 3 Inside (4B)	2.05	2.10	2.08	2.07
Pt 4 Inside (5B)	2.08	2.14	2.13	2.09
Pt 1Ontop (1T)	1.23	1.20	1.19	1.16
Pt 2Ontop (2T)	1.47	1.52	1.48	1.43
Pt 3Ontop (3T)	1.67	1.67	1.66	1.68
Pt 4Ontop (4T)	1.35	1.39	1.37	1.35
Pt 5Ontop (5T)	1.57	1.62	1.63	1.63
Average Dose	1.73	1.66	1.64	1.62

Pt 1 to 4 inside are the point where the left detachable breast was removed and the film placed on the skin of the phantom. Point 1 to 5 ontop are the points, where the films were placed on the left breast.
Source: Field Data, 2018

Table 32: Deviations of Phantom Measurement for LINAC Irradiation

Positions	Expected (Gy)/ Fraction	Deviation(s) (Gy)		
		Anthropomorphic	Adelaide B	Adelaide A
Pt 1 Inside (2B)	2.06	0.89	0.95	0.97
Pt 2 Inside (3B)	2.06	-0.08	-0.08	-0.03
Pt 3 Inside (4B)	2.05	-0.05	-0.03	-0.02
Pt 4 Inside (5B)	2.08	-0.06	-0.05	-0.01
Pt 1Ontop (1T)	1.23	0.03	0.04	0.07
Pt 2Ontop (2T)	1.47	-0.05	-0.01	0.04
Pt 3Ontop (3T)	1.67	0	0.01	-0.01
Pt 4Ontop (4T)	1.35	-0.04	-0.02	0
Pt 5Ontop (5T)	1.57	-0.05	-0.06	-0.06
Average Deviation		0.07	0.08	0.11

Source: Field Data, 2018

The phantoms were irradiated with two tangential fields of medial and lateral at 1.37 min and 1.42 min treatment times respectively at a dose of 50 Gy with the Cobalt machine. Equation (32) was used to convert the prescribed dose in treatment time. Table 33 presents the measurement results of the Cobalt-60 irradiation.

From Table 31a and 32, Points 1T, 2T, 3T, 4T and 5T were positioned on top of the left breast of the phantoms, while 2B, 3B, 4B and 5B were positioned without the left breast (mastectomy). Point 1T was positioned on the centre (nipple) of the breast and the planned dose estimated was lower than delivered dose. Points 2T, 3T, 4T and 5T were positioned anticlockwise on the Cartesian coordinate of North, West, South and East respectively. Points 2B, 3B, 4B and 5B were also positioned anticlockwise on the Cartesian coordinate of North, West, South and East respectively.

Table 33: Phantom Measurement and Deviations for Co-60 Irradiation

Positions	Expected (Gy)/ Fraction	Adelaide B		Adelaide A	
		Measured (Gy)	Deviation (Gy)	Measured (Gy)	Deviation (Gy)
Pt 1 Inside (2B)	2.06	1.13	0.93	1.16	0.90
Pt 2 Inside (3B)	2.06	2.19	-0.13	2.15	-0.09
Pt 3 Inside (4B)	2.05	2.17	-0.12	2.10	-0.05
Pt 4 Inside (5B)	2.08	2.14	-0.06	2.13	-0.05
Pt 1Ontop (1T)	1.23	1.37	-0.14	1.31	-0.08
Pt 2Ontop (2T)	1.47	1.57	-0.10	1.49	-0.02
Pt 3Ontop (3T)	1.67	1.72	-0.05	1.69	-0.02
Pt 4Ontop (4T)	1.35	1.39	-0.04	1.34	0.01
Pt 5Ontop (5T)	1.57	1.58	-0.01	1.58	-0.01
Average Deviation			0.03		0.07

Source: Field Data, 2018

Each position had different measured dose readings. The measured (planned) doses for positon 3B to 5B and 2T to 5T were higher than their expected (delivered) dose values. The estimated dose for position 1 (2B) was lower than what was expected to be given. The maximum delivered dose was measured at position 2 (3B). Position 3B was included in the lateral radiation field. Again, the highest deviation of 0.97 from the measurements of the delivered dose of the LINAC was within the tolerance of -5% and +7% according to ICRU 50 and 62.

Validation of Critical Organ Doses

An evaluation of the critical organs namely, lungs, heart and spinal cord for breast cancer irradiation techniques results from the treatment planning system using LINAC and Co-60 treatment machines and the phantoms is presented and discussed. Table 34 shows the results of the average doses over the specific volume for the critical organs of lung, heart and spinal cord within the thoracic region of the female body.

Table 34: Average Doses for Organs Around the Target Left Breast for Intact Breast

Energy	1.25 MeV	6 MV	Dose Constraints*
Organs	Dose (Gy)$\pm\sigma$	Dose (Gy)$\pm\sigma$	Dose (Gy)/fraction
L. Lung	0.7438$\pm$0.0358	0.7771$\pm$0.0101	3
R. Lung	0.09406$\pm$0.0135	0.0862$\pm$0.0618	
Heart	0.3441$\pm$0.0479	0.3726$\pm$0.0971	1.8
Spinal Cord	0.0310$\pm$0.0198	0.0454$\pm$0.0171	2
R. Breast	0.9253$\pm$0.0732	0.7289$\pm$0.1723	---

where σ is standard deviation; * from Radiation Therapy Oncology Group 0617;
Source: Field Data, 2018; RTOG, 2018

From Table 33, the non-target right breast received the highest delivered dose of 0.93$\pm$0.07. Additionally, the left lung also received high absorbed dose during the irradiation because it was within the treatment field. The spinal cord measured the lowest radiation dose of 0.03$\pm$0.02 and 0.05$\pm$0.01 for beam energies of 1.25 MeV and 6 MV respectively. This was because of the organ's distance from the targeted location. The median range for the mean planned dose was 0.45 Gy (0.00–4.61Gy) and 0.25 Gy (0.61–0.54 Gy) to the left and right lungs respectively. The mean expected (planned) dose to be received by the left and right lungs were 0.61$\pm$0.46 and 0.25$\pm$0.05 within a dose volume of 455.1 and 271.6 ccm respectively for the phantoms irradiated. The results for the critical structures were all within the RTOG 0617 for dose constraints. In radiation therapy, the phantoms exposed to ionizing radiation and therefore, the organs as much as possible should be excluded from the treatment volume (Berrington et al., 2010).

According to a research conducted by Duma et al., (2017), on doses to the heart, the median range for the mean dose to the whole heart was 3.6 Gy (2.6–8.9 Gy) and 2.6 Gy (0.8–3.5 Gy) for high dose and low dose respectively. The average dose to the heart was estimated to be 4.0±1.3 Gy and 2.3±0.8 Gy for high dose and low dose respectively.

It is therefore important to minimize the dose distribution to the heart and the lung to reduce the risk of cardiac radiation injury and pulmonary damage. The target volume to the spinal cord should be contoured on every slice of CT simulation. Recommending dose constraints is quite challenging, because there are no clear and consistent thresholds according to Marks et al. (2010), therefore, the acceptable risk level varies with the clinical scenario.

In summary, to reduce and optimize the absorbed dose scattered to the critical organs, the appropriate dosimetric techniques employed for dose constraint should be assessed before their application in treatment.

Chapter Summary

This chapter presented the study results of the measured parameters in graphical and tabular forms. The results provided give answers to the research questions that were asked. It also describes the relationship between the various measurable quantities that were used to calculate the derived quantities in order to draw reasonable conclusions. Moreover, the chapter gives explanation to the MCNP modelling equation derived and its significance on dose verification in radiation therapy.

CHAPTER FIVE

SUMMARY, CONCLUSIONS AND RECOMMENDATIONS

Overview

This research work addressed the verification of planned and delivered doses using standard and constructed phantoms for the assessment and treatment of detected tumour in a breast. This chapter presents the comprehensive summary of the major findings of the measured and calculated parameters of the EBT3 film dosimetry and quality control on the radiotherapy machines used. Also, the chapter draws insightful conclusions on the fabrication of physical phantoms for clinical application of dose assessment of the critical organs located in the thoracic region of the female body. The summary of the theoretical analysis of the MCNP transport is presented. The chapter provides the concluding summary of the study and recommendations of the key findings relevant to the stakeholders.

Summary

The study addressed four broad areas on quality control of the radiation machines, evaluation of EBT3 dosimetry, Cobalt-60 virtual simulation and dose validation of standard and constructed phantoms. The operational techniques assessed on the treatment units at the facilities were the dosimetry of the beam output from the machines, the gantry and collimation angles and linearity. The mechanical check on lasers alignment, gantry rotation, field sizes and table movement as well as the radiation safety checks were assessed. It was observed that the machine characteristics did not deviate significantly from their baseline values of $\pm 2\%$ and $\pm 3\%$ acquired at the time of acceptance and commissioning of the Cobalt-60 and LINAC machines respectively. The safety checks on entrance interlocks, beam ON indicator were all functional for both treatment units.

Secondly, the study also evaluated the radiochromic EBT3 film dosimeter. The following were assessed: calibration and sensitivity of the film, relationship between the optical density and the dose, energy response on the film, the effect of the area selection of the scanned image, effect of film orientation, the scanning response of different scanners and scanner uniformity. It was observed that the beam energy was independent on the EBT3 films. The type of scanners to be used in scanning the EBT3 films is also important, because different scanners used might not be sensitive to the EBT3 films, and therefore, one choice of scanning orientation should be adopted and the EBT3 films should be positioned in the centre of the scanner in the perpendicular direction to the scan.

Thirdly, the MCNP model developed the transport of 10^7 photons sources of the radiation that pass through the phantom for a desired distribution of absorbed dose during breast treatment. The absorbed dose simulated was absorption dependent on the penetration ability based on different layers on the material density used and the size of the exposed area.

Fourthly, the dose was verified for left intact breast and mastectomy by determining the tissue characterization (electron density and linear attenuation coefficient) of the local materials used for the standard and Adelaide phantoms. The ionization chamber and phantom measurements were assessed for absorbed doses from the LINAC and Co-60 treatment units. The doses delivered to the critical organs at the targeted thoracic region were assessed. The dosimetric parameters and appropriate techniques employed to assess the dose verification and constraints of the measured absorbed doses were discussed.

Conclusions

Two phantoms made of Perspex namely Adelaide A and B, were constructed from locally available materials of balloons, mango seed, cassava stick and candle. These materials were used as mimic tissues in the female thoracic body region. Based on its radiological properties, these tissues were simulated using the planned doses in a particular area. The results of the constructed Adelaide phantoms show that the delivered doses measured were slightly higher than the planned doses. Also, it was observed that the left intact breast received lower doses as compared to the doses received when the left breast was removed and irradiated for the beam energies of 1.25 MeV, 6 MV and 15 MV for all the used phantoms. The work has demonstrated that the use of local materials available in Ghana could be used as a good substitute to commercially produced phantoms. Therefore, they serve as relatively cheap but accurate diagnostic and treatment option materials to clinicians, scientist and students.

Again, from the study, the non-target right breast received the highest delivered doses of 0.93 ± 0.07 Gy and 0.73 ± 0.17 Gy for Co-60 and LINAC repectively, due to the direction of the radiation beam. The spinal cord measured the lowest delivered dose to the target organs, while the left lung received the highest doses from the photon beam energies used, because of the supine position of the organ in the thoracic region when being exposed with the beam energies. The doses to the non-target organs were within the acceptance constraint of $\pm 5\%$ of the delivered dose.

The study also considered the outcome of radiation treatment to the precision in the delivered dose, and found to be dependent on the accuracy of the beam data used. The beam output measured was 1.263±0.007 Gy and 1.306±0.013% Gy for the linear accelerator and Co-60 treatment unit respectively. These values did not deviate significantly from their baseline values of ±2% and ±3% acquired at the time of acceptance and commissioning of the Co-60 and LINAC machines respectively. The dosimetric data parameters used on Co-60 and LINAC machines were all within the acceptable limits set for the machine performance and testing procedures. Therefore, the facilities could be said to be working self consistently.

The study provided a theoretical model, to predict the dose distribution at each point of the phantom, mimicking the tissues in the body with virtual phantoms. The results were validated with experimental measurement using Co-60 gamma source. The absorbed dose at the entrance surface was higher compared with the doses deeper within the phantom. The Monte Carlo simulation estimated for absorbed dose was below 5% of the acceptable tolerance. Therefore, the doses absorbed at different depths in layers within the virtual phantom were not uniform, because of the dependency on the penetration ability of the beam on the material density and the field size of the exposed area.

This work through the use of constructed phantoms, and based on the theoretical calculations and experimental dose measurements, has exhibited that the organs and non-target organs were not at risk and other organs could also be assessed. Also, the constructed phantoms provide a significant contribution as it could be used as a stand-in patient, so that repeated and multiple measurements can be performed without adding to any patient exposure.

Recommendations

Based on the study results, the following recommendations were made in order to help improve and increase the beneficial role of radiation therapy of cancer patients especially breast cancers:

(i) The Health Professional

It is recommended for medical physicists and radiotherapists to use the Adelaide phantoms constructed in the clinical training for optimization studies in radiation dosimetry for students because, the standard phantom is readily not available.

Also, the constructed phantoms would assist the health professionals, in the calibration of CT scanners and for the pre-clinical assessment of absorbed dose to organs of patient data for treatment planning.

(ii) To Research Community

It is recommended that this research work should be applied to real life situations of breast cancer patients.

REFERENCES

Aget, H., & Rosenwald, J. C. (1991). Polarity effect for various ionization chambers with multiple irradiation conditions in electron beams. *Medical Physics, 18*, 67-72.

Ahnesjö, A., & Aspradakis, M. (1999). Dose calculation for external photo beams in radiotherapy. *Physics in Medicine and Biology, 44*(11), 99-155.

Alderson, S. W., Lanzl, L. H., Rollins, M., & Spira, J. (1962). An instrumented phantom system for analog computation of treatment plans. *The American Journal of Roentgenology Radium Therapy and Nuclear Medicine, 87*, 185-95.

Allemani, C., Weir, H.K., Carreira, H., Harewood, R., Spika, D., Wang, X.S., Bannon, F., Ahn, J.V., Johnson, C.J., Bonaventure, A., Marcos-Gragera, R., Stiller, C., Azevedo e Silva, G., Chen, W.Q., Ogunbiyi, O.J., Soeberg, M.J., You, H., Matsuda, T., Bielska-Lasota, M., Storm, H., Tucker, T.C., Coleman, M.P., CONCORD Working Group. (2015). Global surveillance of cancer survival 1995-2009: Analysis of individual data for 25,676,887 patients from 279 population-based registries in 67 countries (CONCORD-2). *Lancet, 385*(9972), 977-1010.

Almond, P., Biggs, P., Coursey, B., Hanson, W. F., Saiful Huq, M., Nath, R., & Rogers, D. W. O. (1999). AAPM's TG-51 protocol for clinical reference dosimetry of high-energy photon and electron beams. *Medical Physics, 26*(9), 1847-1870.

American Cancer Society. (2010). *Cancer facts and figures 2010*. Atlanta, Georgia: American Cancer Society.

https://www.cancer.org/research/cancer-facts-statistics/all-cancer-facts-figures/cancer-facts-figures-2010.html.

American Cancer Society. (2016). *Breast cancer facts & figures 2015-2016.* Atlanta, Georgia: American Cancer Society. Retrieved from https://www.cancer.org/content/dam/cancer-org/research/cancer-facts-and-statistics/breast-cancer-facts-and-figures/breast-cancer-facts-and-figures-2015-2016.pdf.

American Cancer Society. (2017). *Global burden of cancer in women: Current status, trends and interventions.* Atlanta, Georgia: American Cancer Society. Retrieved from https://www.cancer.org/content/dam/cancer-org/research/cancer-facts-and-statistics/annual-cancer-facts-and-figures/2017/cancer-facts- and-figures-2017.pdf.

Andreo P. (1991). Monte Carlo Techniques in medical radiation physics. *Physics in Medicine and Biology, 36*, 861–920.

Andreo P. (1992). Monte Carlo techniques in medical radiation physics. *Physics in Medicine and Biology, 37*, 2031–2032.

Andres, C., Del Castillo, A., Tortosa, R., Alonso, D., & Barquero, R. (2010). A comprehensive study of the GafChromic EBT2 radiochromic lm. A comparison with EBT. *Medical Physics, 37*(12), 6271-78. Retrieved June 21, 2018, Retrieved from https://www.researchgate.net/publication/235885273_Dosimetric_characterization_and_use_of_GAFCHROMIC_EBT3_film_for_IMRT_dose_verification.

Arjomandy, B., Tailor, R., Anand, A., Sahoo, N., Gillin, M., Prado, K., & Vicic, M. (2010a). Radiochromic film dosimetry. *Medical Physics Publishing,* *37*, 1942-1947.

Arjomandy, B., Tailor, R., Anand, A., Sahoo, N., Gillin, M., Prado, K., & Vicic, M. (2010b). Energy dependence and dose response of gafchromic ebt2 film over a wide range of photon, electron, and proton beam energies. *Medical Physics, 37*(5), 1942-1947.

Arnfield, M.R., Siantar, C.H., Siebers, J., Garmon, P., Cox L. & Mohan, R. (2000). The impact 113 of electron transport on the accuracy of computed dose. *Medical Physics, 27,* 1266-1274.

Asnaashari, K., Gholami, S., & Khosravi, H. (2014). Lessons learnt from errors in radiotherapy centers. *International Journal of Radiation Research, 12*(4), 365-367.

Attix, F. H. (1986). Introduction to radiological physics and radiation dosimetry. New York: John Wiley & Sons. http://dx.doi.org/10.1002/9783527617135

Baker, G. (2006). Localization: Conventional and CT simulation. *British Journal of Radiology, 79*, 36-49.

Balaji, K., Balaji, S., Yadav, P., Radha, C., & Ramasubramanian, V. (2016). Radiation therapy for breast cancer: Literature review. *Medical Dosimetry, Elsevier Incorporation; American Association of Medical Dosimetrists.* Retrieved July 27, 2017, from http://dx.doi.org/10.1016/j.meddos.2016.06.005.

Barboriak, D., Padua, A., York, G., & Macfall, J. (2005). Creation of DICOM—Aware applications using imageJ. *Journal of Digital Imaging.* 91–99. doi:10.1007/s10278-004-1879-4.

Battista, J. J., Rider, W. D., & Van Dyke, J. (1980). Computed tomography for radiotherapy planning. *International Journal of Radiation Oncology, Biology, Physics, 6*, 99-107.

Berrington, de Gonzalez A., Curtis, R.E., Gilbert E, Berg, C. D., Smith, S. A., Stovall, M., & Ron E. (2010). Second solid cancers after radiotherapy for breast cancer in SEER cancer patients. *British Journal of Cancer. 102*(1), 220–226.

Borca, V. C., Pasquino, M., Russo, G., Grosso, P., Cante, D., Sciacero, P., Girelli, G., La Porta, M.R., & Tofani, S. (2013). Dosimetric characterization and use of GAFCHROMIC EBT3 Film for IMRT dose verification. *Journal of Applied Clinical Medical Physics, 14*(3), 158-159.

Bouchard, H., Lacroix, F., Beaudoin, G., Carrier, J. F., & Kawrakow, I. (2009). On the characterization and uncertainty analysis of radiochromic film dosimetry. *Medical Physics, 36*(6), 1931-1946.

Brahme, A., Chavaudra, J., Landberg, T., McCullough, E. C., Nusslin, F., Rawlinson, J. A., Svensson, H. & Svensson, H. (1988). *Accuracy requirements and quality assurance of external beam therapy with photons and electrons. vol. 15* (Suppl). Foundation Acta Radiologica.

Brown, T. A., Hogstorm, K. R., Alvarez, D., Matthews II, K. L., & Dugas., K. J. (2012, December). Dose-response curve of ebt, ebt2, and ebt3 radiochromic films to synchrotron-produced monochromatic x-ray beams. *Medical Physics, 39*(12), 7412-7417.

Butson, M. J., Yu, P. K., Cheung, T., & Metcalfe, P. (2003). Radiochromic film for medical radiation dosimetry. *Materials Science and Engineering, 14*, 61-120.

Butson, M. J., Cheung, T. & Yu, P. K. (2006). Weak energy dependence of EBT Gafchromic film dose response in the 50 kVp–10 MVp x-ray range. *Applied Radiation and Isotopes, 64,* 60-62.

Buzug, T. (2008). *Computed tomography: from photon statistics to modern cone-beam CT.* Los Angeles: Springer.

Canadian Nuclear Safety Commission. (2012). *Introduction to dosimetry.* Retrieved from. www.*nuclearsafety.gc.ca.*

Cheng, B. S., Alphonse, L., Krishna, K., Tony, C., Saliful, H. & Carol, S. (2005). Determination of CT-to-density conversion relationship for image-based treatment planning systems. *Medical Dosimetry, 30*(3), 145-148.

Cherry, P., & Duxbury, A. (2009). *Practical radiotherapy physics and equipment.* (2nd ed.). Wiley-Blackwell Publication. Retrieved from ssu.ac.ir/cms/fileadmin/user_upload/Mtahghighat/.../Practical_Radiotherapy.pdf.

Chiu-Tsao, S. T., Ho, Y., Schankar, R., Wang, L., & Harrison, L. B. (2005). Energy dependence of response of new high sensitivity radiochromic films for megavoltage and kilovoltage radiation energies. *Medical Physics, 32,* 3350-3354.

Claude, K. P., Tagoe, S. N., Schandorf, I. C., & Amuasi, J. H. (2013). Fabrication of a Tissue characterization phantom from indigenous materials for computed tomography electron density calibration. *The South African Radiographer, 51*(1).

Dance, D. R., Christofides, S., Maidment, A. D., Mclean, I. D., & Ng, K.-N. (2014). *Diagnostic radiology physics: A handbook for teachers and* *students, Chapter 11.* Vienna: International Atomic Energy Agency. https://humanhealth.iaea.org/HHW/MedicalPhysics/TheMedicalPhysicist/Studentscorner/HandbookforTeachersandStudents/Chapter_11.pdf.

Darby, S., McGale, P., Correa, C., Taylor, C., Arriagada, R., Clarke, M., Cutter, D., Davies, C., Ewertz, M., Godwin, J., Gray, R., Pierce, L., Whelan, T., Wang, Y., & Peto, R. (2011). Effect of radiotherapy after breast-conserving surgery on 10-year recurrence and 15-year breast cancer death: Meta-analysis of individual patient data for 10,801 women in 17 Randomised Trials. *Lancet, 378*(9804), 1707-1716. doi:10.1016/S0140-6736(11)61629-2.

Davidson, M. W. (1998). *Fundamentals of film exposure. Molecular expressions: Optical miscroscopy primer: Photomicrography.* 2013. http://micro.magnet.fsu.edu/primer/photomicrography/filmexposure.html. Assessed on July 13, 2018.

Desroches, J., Bouchard, H., & Lacroix, F. (2010). Potential errors in optical density measurements due to scanning side in EBT and EBT2 GafChromic film dosimetry. *Medical Physics, 37*(4), 1565–70. Retrieved June 21, 2018, from https://www.researchgate.net/publication/235885273_Dosimetric_characterization_and_use_of_GAFCHROMIC_EBT3_film_for_IMRT_dose_verification.

Devic, S., Tomic, N., Pang, Z., Seuntjens, J., Podgorsak, E. B., & Soares, C.G. (2007). Absorption spectroscopy of EBT Model GAFCHROMIC Film. *Medical Physics. 34*(1), 112-18.

Devic, S., Tomic, N., Soares, C. G., & Podgorsak, E. B. (2009). Optimizing the dynamic range extension of a radiochromic film dosimetry system. *Medical Physics, 36*(2), 429-437.

Devic S., Aldelaijan S., Mohamed H., Tomic, N., Liang, L. H., DeBlois, F. & Seuntjens J. (2010). Absorption spectra time evolution of EBT-2 Model GAFCHROMIC Film. *Medical Physics, 37*(5), 2207-2214.

DeWerd, L., & Kissick, M. (2014). *The phantoms of medical and health physics*. Berlin: Springer. Retrieved from https://www.springer.com/gp/book/9781461483038, July 13, 2018.

Diacon, B. (2015). *Introduction to gamma detection and pulse height analysis, engineering physics*. Retrieved from engphys.mcmaster.ca/undergrad-studies/ug-courses/eng-phys-3d03/.

Dobbs, H. J., Parker, R. P., Hodson, N. J., Hobday, P., Husband, J. E. (1983). The use of CT in radiotherapy treatment planning. *Radiotherapy and Oncology, 1*, 133-142.

Duggan, D. M., & Coffey, C. W. (1998). Small photon field dosimetry for stereotactic radiosurgery. *Medical. Dosimetry, 23*(3), 153-159.

Duma, M. N., Herr, A.-C., Borm, K. J., Trott, K. R., Molls, M., Oechsner, M., & Combs, S. E. (2017). Tangential field radiotherapy for breast cancer—The dose to the heart and heart subvolumes: What structures must be contoured in future clinical trials. *Frontiers in Oncology, 7*, 130. doi:10.3389/fonc.2017.00130.

Durham, S. (2015). *Longitudinal effects in gafchromic film*. Master of Science in Medical Physics Thesis. Oregon State University. 9.

Dutriex, A. (1984). When and how can we improve precision in radiotherapy? *Radiotherapy and Oncollgy, 2*, 275-292.

Dyk, J. V., & MacDonald, J. C. (1972). Penetration of high energy electrons in water. *Physics in Medicine and Biology, 17*, 52-65.

Ebert, M.A., Lambert, J., & Greer, P.B. (2008). CT-ED conversion on GE light speed RT scanner: Influence of scanner settings. *Australasian Physical & Engineering Sciences in Medicine*, *31*(2), 154-159.

Elbashir Ali, A. M. (2008). *Dose measurements for a radiotherapy Co-60 machine*. Master of Science Degree in Medical Physics Thesis. Sudan Academy of Sciences.

Elekta. (2011). *Elekta updated planned maintenance procedures*. User notice.

Farah, N., Francis, Z., & Abboud, M. (2014). Analysis of the EBT3 GafChromic film irradiated with 6 MV Photons and 6 MeV electrons using reflective mode scanners. *Physica Medica, 30*(6), 708-12. doi:10.1016/j.ejmp.2014.04.010.

Ferlay, J., Soerjomataram, I., Ervik, M., Dikshit, R., Eser, S., Mathers, C., Rebelo, M., Parkin, D.M., Forman, D., & Bray, F. (2013). *GLOBOCAN 2012 v1.0, Cancer incidence and mortality worldwide*. International Agency for Research on Cancer. No. 11. Lyon, Franc. Retrieved July 27, 2017, from http://globocan.iarc.fr.

Forrest, L. (2003). *Radiation therapy. in clinical neurology in small animals - localization, diagnosis and treatment*. (K. Braund, Ed.) New York: International Veterinary Information Service (www.ivis.org), Ithaca.

Gazda, M. J., & Coia, L. R. (2004). *Principles of radiation therapy* (8th ed.). CMP: University of Michigan.

GLOBOCAN. (2012). *Estimated cancer incidence, mortality and prevalence worldwide in 2012*. International Agency for Research on Cancer; World

Health Organization. Retrieved July 27, 2017, from http://globocan.iarc.fr/old/FactSheets/cancers/breast-new.asp.

Goitein, M. (1982). Applications of CT in radiotherapy treatment planning, C. G. Orton (ed.), New York. *Progress in Medical Radiation Physics*, 195-293.

Greene, D. & Williams P.C. (1997). *Linear accelerators for radiation therapy*, (2nd ed.). Bristol: Institute of Physics Publishing, Medical Science Series.

Hartmann, G. H. (2006). *Quality management in radiotherapy*. Heidelberg: Department of Medical Physics in Radiotherapy.

Hartmann, G. (2015). *Dosimetry: Fundamentals, ICTP school on medical physics for radiation therapy: Dosimetry and treatment planning for basic and advanced applications*. Trieste, Italy: Miramare.

Haviland, J., Owen, J., Dewar, J., Agrawal, R., Barrett, J., Barrett-Lee, P., Dobbs, J.H., Hopwood, P., Lawton, A.P., Magee, J.B., Mills, J., Simmons, S., Sydenham, M.A., Venables, K., Bliss, M.J., & Yarnold, J. (2013). The UK Standardisation of Breast Radiotherapy (START) trials of radiotherapy hypofractionation for treatment of early breast cancer: 10-year follow up results of two randomised controlled trials. *Lancet Oncology, 14*(11), 1086-1094. doi:10.1016/S1470-2045(13)70386-3.

Helmer, R. G. (2006). *27 Co 33. 1 decay scheme. Co-60 disintegrates by beta minus emissions to excited*. INEEL 03/02/1998 - 13/01/2006. Scheme page 1/1.

Heymsfield, S. (2005). *Human body - Composition*. Champaign, IL: Human Kinetics Publishers.

IAEA. (2000). Absorbed dose determination in external beam radiotherapy, *Technical report series no. 398: An international code of practice for dosimetry based on standards of absorbed dose to water*. Vienna: International Atomic Energy Commission, Austria. Retrieved https://www-pub.iaea.org/MTCD/publications/PDF/TRS398_scr.pdf.

ICRP. (1991). *Recommendations of the international commission on radiological protection*. Oxford: ICRP Publication. International Commission on Radiological Protection, Pergamon Press.

International Commission on Radiation Units [ICRU]. (1976). *Determination of absorbed dose in a patient irradiated by beams of x or gamma rays in radiotherapy procedures*. Bethesda: ICRU.

International Commission on Radiation Units [ICRU]. (1989). *Tissue substitutes in radiation dosimetry and measurement ICRU Report 44*. Bethesda, MD: International Commission on Radiation Units and Measurements.

International Commission on Radiation Units [ICRU]. (1993). *Prescribing, recording, and reporting photon beam therapy*. Bethesda: International Commission on Radiation Units and Measurements Report No.50.

International Commission on Radiation Units [ICRU]. (1999). *Prescribing, recording, and reporting photon beam therapy*. Bethesda: International Commission on Radiation Units and Measurements Report No.62,

International Commission on Radiation Units [ICRU]. (2010). *Prescribing, recording, and reporting photon-beam Intensity-Modulated Radiation Therapy (IMRT)*. Bethesda: International Commission on Radiation Units and Measurements No.83.

ImageJ. (2018a). Retrieved June 29, 2018, from https://imagej.nih.gov/ij/docs/intro.html.

ImageJ. (2018b). *Colour image processing.* Retrieved June 29, 2018, from https://imagej.net/Colour_Image_Processing.

Izewska, J., & Rajan, G. (2005). Chapter 3: Radiation dosimeters. In Podgorsak, E.B., (Ed.), *Radiation oncology physics: A handbook for teachers and students*. Vienna: International Atomic Energy Agency-IAEA,

Jones, A. O., & Das, I. J. (2005). Comparison of inhomogeneity correction algorithms in small photon fields. *Medical Physics, 32*, 766-276.

Jorhem, L. (1993). Determination of metals in foodstuffs by atomic absorption spectrophotometry after dry ashing. *Journal of AOAC International, 76*, 798–13.

Jorhem, L., & Engman, J. (2000). Determination of lead, cadmium, zinc, copper, and iron in foods by atomic absorption spectrometry after microwave digestion: NMKL collaborative study. *Journal of AOAC International, 83*(5), 1189-203.

Jursinic, P. A., & Nelms, B. E. (2003). A 2-D diode array and analysis software for verification of intensity modulated radiation therapy delivery. *Medical Physics, 30*, 870–879.

Khan, M. (1994). *The physics of radiation therapy* (2nd ed.). London: Williams and Wilkins.

Khan, F. M. (2003). *The physics of radiation therapy*. (3rd ed.). Baltimore: Lippincott Williams & Wilkins.

Khan, F. M. (2009). *The physics of radiation therapy*. (4th ed.). Baltimore: Williams & Wilkins Baltimore.

Kienbock, R. (1906). On the quantimetric method: Archives of the Roentgen Ray. *The British Institute of Radiology*, *11*(1), 17-20. Retrieved from https://doi.org/10.1259/arr.1906.0005.

Kirby, D., Green, S., Palmans, H., Hugtenburg, R., Wojnecki, C., & Parker, D. (2010). LET dependence of GafChromic films and an ion chamber in low-energy proton dosimetry. *Physics in Medicine and Biology, 55*, 417-433.

Klevenhagen, S. C. (1993). *Physics and dosimetry of therapy electron beams. Madison, WI: Medical Physics Publishing.*

Knoll, G. F. (1989). *Radiation detection and measurement* (2nd ed.). Canada: John Wiley & Sons.

Knöös, T. T. (1991). *Dose planning and dose delivery in radiation therapy.* Doctoral Dissertation, Department of Radiation Physics. Lund University, Malmö, Sweden.

Korhonen, L. (2009). *Methods for dose calculation and beam characterization in external photon beam radiotherapy.* Doctoral Dissertation. Helsinki: Helsinki University of Technology Faculty of Information and Natural Sciences, Department of Biomedical Engineering and Computational Science.

Lanzl, L. H. (1995). *The rando phantom and its medical applications.* Illinois: Department of Radiology, The University of Chicago,

Lieser, K.H. (1991). Einführung in die Kernchemie. *S.223, Abb.* (7-22); ISBN 3-527-28329-3H

Li Hsu, C. M. (2010). *Three-dimensional computerized breast phantom based on empirical data.* Dissertation in the Department of Biomedical

Engineering. Graduate School of Duke University.

Lindsay, P., Rink, A., Ruschin, M., & Jaffray, D. (2010). Investigation of energy dependence of EBT and EBT-2 GafChromic Film. *Medical Physics, 37*(2), 571-576.

Lu, L. (2013). Dose calculation algorithms in external beam photon radiation therapy. *International Journal of Cancer Therapy and Oncology, 1* (2). doi:10.14319/ijcto.01025.

Mackie, T. R., Reckwerdt, P., McNutt, T., Gehring, M., & Sanders, C. (1996). *Photon beam dose computations' in teletherapy: Past and future.* Madison Wisconsin: Medical Physics Publishing.

Mahavir, S., & Babita, J. (2013). Association between body mass index and risk of breast cancer among females of North India. *South Asian Journal of Cancer, 3*, 121-125.

Marks, L. B., Bentzen, S. M., Deasy, J. O., Kong, F.-M., Bradley, J. D., Vogelius, I. S., Naqa, I. E., Hubbs, J. L., Lebesque, J. V., Timmerman, R. D., Martel, M. K., & Jackson, A. (2010). Radiation Dose volume effects in the lung. *International Journal of Radiation Oncology Biology Physics, 76*(3), 70-76.

Martisikova, M., Ackerman, B., & Jäkel, O. (2008). Analysis of uncertainties in GafChromic EBT film dosimetry of photon beams. *Physics in Medicine and Biology, 53*(24), 7013-7027.

Marroquin, E. Y. L., González, J. A. H., López, M. A. C., & Barajas, J. E.V., García-Garduño, O. A. (2016). Evaluation of the uncertainty in an EBT3 film dosimetry system utilizing net optical density. *Journal of Applied Clinical Medical Physics, 17*(5), 466-481.

Matney, J. E., Parker, B. C., Neck, D. W., Henkelmann, G., & Rosen, I. I. (2010). Evaluation of a commercial flatbed document scanner and radiographic film scanner for radiometric EBT film dosimetry. *Journal of Applied Clinical Medical Physics, 11*(2), 198-208.

Medela, A.G. (2006). *Anatomy and physiology of the breast*. Retrieved from http://www.medelabreastfeedingus.com/forprofessionals/cbe-information/106/breast-anatomy-research.

Menegotti, L., Delana, A., & Martignana, A. (2008). Radiochromic flim dosimetry with flatbed scanners: A fast and accurate method for dose calibration and uniformity correction with single film exposure. *Medical Physics, 35*(7), 3078-3085.

Metcalfe, P., Kron, T., & Hoban, P. (1997). *The physics of radiotherapy x-rays from linear accelerators*. Madison, Wisconsin: Medical Physics Publishing.

Mijnheer, B. J. (1985). Variations in response to radiation o a nylon-walled ionization chamber induced by humidity changes. *Medical Physics, 12*, 625-626.

Mijnheer, B. J., Battermann, J., & Wambersie, A. (1987). What degree of accuracy is required and can be achieved in photon and neutron therapy? *Radiotherapy and Oncology, 8*, 237-52.

NDT Resource Center. (2014). *2001-2014 film characteristic curves*. Retrieved from https://www.ndt-ed.org/EducationResources/CommunityCollege/Radiography/TechCalibrations/Sensitometric.htm.

Neuenschwander, H., Mackie, T. R., & Reckwerdt, P. (1995). MMC-a high-performance Monte Carlo code for electron beam treatment planning. *Physics in Medicine and Biology, 40*(4).

Niroomand-Rad, A., Blackwell, C. R., Coursey, B. M., Gall, K. P., Galvin, J. M., McLaughlin, W. L., Meigooni, A.S., Nath, R., Rodgers, J.E., & Soares, C. G. (1998). Radiochromic film dosimetry: Recommendations of AAPM radiation therapy committee task group 55. American Association of Physicists in Medicine. *Medical Physics, 20*(11), 2093-2115.

Paelinck, L., De Neve, W., & De Wagter, C. (2007). Precautions and strategies in using a commercial flatbed scanner for radiochromic film dosimetry. *Physics in Medicine and Biology, 52*(1), 231-242.

Pai, S., Indra, J. D., James, F. D., & Kwok, L. L. (2007). *TG-69: Radiographic film for megavoltage beam dosimetry*. Task Group 216. AAPM.

Podgorsak, E. (2005). *Radiation oncology physics: A handbook for teachers and students*. Vienna: International Atomic Energy Agency.

Prado, K. L. (2019). *Clinical dosimetry in radiotherapy. Argonne national laboratory course: 3DCRT for technologists*. Retrieved March 4, 2019 from https://international.anl.gov/training/materials/B1/Prado/Clinical-Dosimetry.pdf

Prokop, M. (2003). *Spiral and multislice computed tomography of the body.* New York: Thieme Medical Publishers.

Purdy, J. A., & Starkschall, G. (1999). *A practical guide to 3-d planning and conformal radiation therapy*. Madison, WI: Advanced Medical Publishing Inc.

Reinhardt, S., Hillbrand, M., Wilkens, J. J., & Assmann, W. (2012).

Comparison of GafChromic EBT2 and EBT3 films for clinical photon and proton beams. *Medical Physics, 39*(8), 5257-5262.

Renade, M. K., Li, J. G., Dubose, R. S., Kozelka, J., Simon, W. E., & Dempsey, J. F. (2008). A prototype quantitative film scanner for radiochromic film dosimetry. *Medical Physics, 35*(2), 473-479.

Rogers, O. D. W., & Ross, C. K. (1988). The role of humidity and other correction factors in the AAPM TG-21 dosimetry protocol. *Medical Physics, 15*, 40-48.

Rogers, D. W., Faddegon, B. A., Ding, G. X., Ma, J. W., & Mackie, T. R. (1995). Beam: A Monte Carlo code to simulate radiotherapy treatment units. *Medical Physics, 22*, 503-524.

Rogers, D. W. O. (2018). *The physics of the AAPM's TG-51 protocol, Chapter 9*. Retrieved on July 3, 2018 from https://medicalphysics.org/documents/aapm_mono34_CH09.pdf

RTOG. (2018). *RTOG radiation dose constraints, protocol 0617*. Retrieved from https://en.wikibooks.org/w/index.php?title=Radiation Oncology/Toxicity/RTOG&oldid=3432734.

Saeed, S. B. (2015). *Dynamic log files analysis for different dose rate IMRT using DVH and gamma index*. Retrieved from https://www.researchgate.net/publication/297806150_Dynamic_Log_Files_Analysis_For_Different_Dose_Rate_IMRT_Using_DVH_and_Gamma_Index/figures?lo=1, July 18, 2018.

Sarapata, A., Chabior, M., Cozzini, C., Sper, J. I., Beque, D., Langner, O., Coman, J., Zanette, I., Ruiz-Yaniz, M., & Pfeiffer, F. (2014). *Quantitative electron density characterization of soft tissue substitute* *plastic materials using grating-based x-ray phase contrast imaging*. Rev Sci Instrum. doi:10.1063/1.4898052.

Sauer, O. A. (1995). Calculation of dose distributions in the vicinity of high-z interfaces for photon beams. *Medical Physics, 22*, 1685-1690.

Schneider, C. A., Rasband, W. S., & Eliceiri, K. W. (2012). NIH image to ImageJ: 25 years of image analysis. *Nat Methods. 9*(7), 671–675. doi:10.1038/nmeth.2089.

Seutjens, J. P., Strydom, W., & Shortt, K. R. (2003). *Dosimetric prinicples, quantities and units. Radiation oncology physics: A handbook for teachers and students (Vol. 5)*. Wien: International Atomic Energy Agency.

Shani, G. (2001). *Radiation dosimetry: Instrumentation and methods* (2nd ed.). Boca Raton: CRC Press.

Sonia, M. R., Eman, M., Magda, S. H., Ibrahem, I. B., & Esmat, A. A. (2006). Monte Carlo dose calculations for breast radiotherapy using 60Co gamma rays. *Journal of Nuclear and Radiation Physics*, 61-72.

Spiers F.W. (1943). Materials for depth dose measurement. *Br J Radiol*. 16-90

Tailor, R. C., Chu, C., Followill, D., & Hanson, W. F. (1998). Equilibration of air temperature inside the thimble of a farmer-type ion chamber. *Medical Physics, 25*, 496-502.

Thapa, B. (2013). *Development of a patient specific image planning system for radiation therapy*. Retrieved July 27, 2017, from htt://uknowledge.uky.edu/physastron_etds/11.

Thomas, S. J. (1999). Relative electron density calibration of CT scanners for radiotherapy. *British Journal of Radiology, 72*, 781-786.

Van Dyk, J. (1999). *The modern technology of radiation oncology: A compendium for medical physicists and radiation oncologist*. Madison Wisconsin: Medical Physics Publishing. Retrieved from https://medicalphysics.org/documents/VanDyk1_Ch8.pdf

Verhaegen, F., & Seuntjens, J. (2003). Monte Carlo modeling of external radiotherapy photon beams. *Physics in Medicine and Biology*, 107-164.

Vikram, B., Coleman, C. N., & Deye, J. A. (2009). Current status and future potential of advanced technologies in radiation oncology: Challenges and resources. *Oncology, 23*(3), 279.

Washington, C., & Leaver, D. (2003). *Principles and practice of radiation therapy: Physics, simulation, and treatment planning* (1st ed.). Maryland Heights: Mosby.

Watanabe, Y. (1999). Derivation of linear attenuation coeffcients from CT numbers for low-energy photons. *Physics in Medicine and Biology, 44*(9), 2201-11.

Webber, C. E. (1987). The effect of fat on bone mineral measurements in normal subjects with recommended values of bone, muscle, and fat attenuation coefficients. *Clinical Physics and Physiological Measurement, 8*, 143-158.

WHO. (2008). *Radiotherapy risk profile: Technical manual*. Geneva: World Health Organization.

Wilcox, E. E., & Daskalov, G. M. (2007). Evaluation of GafChromic EBT film for cyberknife dosimetry. *34*(6), 1967-74.

Wunsch, J. R. (2000). *Polystyrene – synthesis, production and applications*. Shrewsbury: iSmithers Rapra Publishing.

Wypych, G. (2012). PS polystyrene. *Handbook of Polymers*. doi:10.1016/B978-1-895198-47-8.50162-4.

Xu, L. B. (2009). *Commissioning of a GafChromic EBT film dosimetry protocol at ionizing radiation standards group of National Research Council*. Montreal: Master of Science, Thesis. McGill University.

Yu, C. X., Mackie, T. R., & Wong, J. W. (1995). Photon dose calculation incorporating explicit electron transport. *Medical Physics, 22*, 1157-1165.

APPENDICES

APPENDIX A

Worksheet for the Determination of Absorbed Dose

Determination of the absorbed dose to water in a ^{60}Co γ ray beam

User: ____________ Date: ____________

1. Radiation treatment unit and reference conditions for D_w determination

^{60}Co therapy unit: ____________ Set-up: ❑ SSD ❑ SAD

Reference phantom: water Reference distance: ______ cm

Reference field size: 10 × 10 cm × cm

Reference depth z_{ref}: ______ g/cm²

2. Ionization chamber and electrometer

Ionization chamber model: ____________ Serial No.: ______ Type: ❑ cyl ❑ pp

Chamber wall/window material: ____________ thickness: ______ g/cm²

Waterproof sleeve/cover material: ____________ thickness: ______ g/cm²

Phantom window material: ____________ thickness: ______ g/cm²

Absorbed dose to water calibration factor $N_{D,w}$ = ____________ ❑ Gy/nC ❑ Gy/rdg

Reference conditions for calibration P_o: ______ kPa T_o: ______ °C Rel. humidity: ___ %

Polarizing potential V_1: ______ V Calibration polarity: ❑ +ve ❑ –ve ❑ corrected for polarity effect

User polarity: ❑ +ve ❑ –ve

Calibration laboratory: ____________ Date: ____________

Electrometer model: ____________ Serial No.: ____________

Calibrated separately from chamber: ❑ yes ❑ no Range setting: ______

If yes, calibration laboratory: ____________ Date: ____________

3. Dosimeter reading[a] and correction for influence quantities

Uncorrected dosimeter reading at V_1 and user polarity: ____________ ❑ nC ❑ rdg

Corresponding time: ____________ min

Ratio of dosimeter reading and time[b]: M_1 = ____________ ❑ nC/min ❑ rdg/min

(i) Pressure P: ______ kPa Temperature T: ______ °C Rel. humidity (if known): ______ %

$$k_{TP} = \frac{(273.2+T)}{(273.2+T_o)}\frac{P_o}{P} = \_\_\_\_\_\_$$

(ii) Electrometer calibration factor[c] k_{elec}: ❑ nC/dg ❑ dimensionless k_{elec} = ____________

(iii) Polarity correction[d] rdg at $+V_1$: M_+ = ____________ rdg at $-V_1$: M_- = ____________

$$k_{pol} = \frac{|M_+|+|M_-|}{2M} = \_\_\_\_\_\_$$

(iv) Recombination correction (two voltage method)

Polarizing voltages: V_1 (normal) = ____________ V V_2 (reduced) = ____________ V

Readings[c] at each V: M_1 = ______ M_2 = ______

Voltage ratio V_1/V_2 = ______ Ratio of readings M_1/M_2 = ______

$$k_s = \frac{(V_1/V_2)^2 - 1}{(V_1/V_2)^2 - (M_1/M_2)} = \_\_\_\_\_\_$$

Corrected dosimeter reading at the voltage V_1:

$M = M_1/k_{TP}k_{elec}k_{pol}k_s$ = ______ ☐ nC/min ☐ rdg/min

4. Absorbed dose rate to water at the reference depth z_{ref}

$D_w(z_{ref}) = M\,N_{D,w}$ = ______ Gy/min

5. Absorbed dose rate to water at the depth of dose maximum z_{max}

Depth of dose maximum: z_{max} = 0.5 g/cm²

(i) SSD set-up

Percentage depth dose at z_{ref} for a 10 cm × 10 cm field size: PDD (z_{ref} = ______ g/cm²) = ______ %

Absorbed dose rate calibration at z_{max}:

$D_w(z_{max}) = 100\,D_w(z_{ref})/PDD(z_{ref})$ = ______ Gy/min

(ii) SAD set-up

TMR at z_{ref} for a 10 cm × 10 cm field size: TMR (z_{ref} = ______ g/cm²) = ______

Absorbed dose rate calibration at z_{max}:

$D_w(z_{max}) = D_w(z_{ref})/\mathrm{TMR}(z_{ref})$ = ______ Gy/min

---

[a] All readings should be checked for leakage and corrected if necessary.

[b] The timer error should be taken into account. The correction at voltage V_1 can be determined according to

M_A is the integrated reading in a time t_A — M_A = ______ t_A = ______ min

M_B is the integrated reading in n short exposures of time t_B/n each ($2 \le n \le 5$) — M_B = ______ t_B = ______ min n = ______

Timer error, $\tau = \dfrac{M_B t_A - M_A t_B}{n M_A - M_B}$ = ______ min (the sign of τ must be taken into account)

$M_1 = \dfrac{M_A}{t_A + \tau}$ = ______ ☐ nC/min ☐ rdg/min

[c] If the electrometer is not calibrated separately set $k_{elec} = 1$.

[d] M in the denominator of k_{pol} denotes reading at the user polarity. Preferably, each reading in the equation should be the average of the ratios of M (or M_+ or M_-) to the reading of an external monitor, M_{em}.

[e] Strictly, readings should be corrected for polarity effect (average with both polarities). Preferably, each reading in the equation should be the average of the ratios of M_1 or M_2 to the reading of an external monitor, M_{em}.

[f] It is assumed that the calibration laboratory has performed a recombination correction. Otherwise the factor $k_s' = k_s/k_{s,Q_o}$ should be used instead of k_s. When Q_o is ^{60}Co, k_{s,Q_o} (at the calibration laboratory) will normally be close to unity and the effect of not using this equation will be negligible in most cases.

APPENDIX B

Equipment Specification for EBT3 Irradiation

Linear Accelerator	
Manufacturer	Elekta AB, Stockholm, Sweden
Model / SN	Synergy 11 Platform / 2486
Source Activity	Photons
Energies	6 MV & 15 MV
Cobalt-60	
Manufacturer	Best Theratronics
Model	Theratron Equinox 100 Cobalt-60
Source Activity	399 TBq
Energy	1.25 MeV
Ionization Chamber	
Type	Famer Type ROOS Chamber 34001
Manufacturer	PTW-Freiburg, Germany
Model / SN	TM30010-1 / 000821
Detector Calibration Factor, $N_{D,w}$	5.408×10^{7} Gy/C
Correction Factor	1.000
Uncertainty	1.1%
Chamber Voltage/ Polarity	+400 V
Ion Collection Efficiency	100%
Electrometer	
Type	PTW UNIDOS
Manufacturer	PTW-Freiburg, Germany
Model	T10021
Serial Number	000590
Barometer	
Type / SN	Sensor Type: (GE Barometer: Druck Pace1000) / 3547193
Thermometer	
Type / SN	Thermocouple / Testo 925

APPENDIX C

Tissue Compositions and Densities Based on ICRU 44

Atomic No.	1	6	7	8	11	12	15	16	17	19	20	26	53	Density
Symbol	H	C	N	O	Na	Mg	P	S	Cl	K	Ca	Fe	I	
	[%]	[%]	[%]	[%]	[%]	[%]	[%]	[%]	[%]	[%]	[%]	[%]	[%]	[g/cm^3]
SOFT TISSUE	10.5	12.5	2.6	73.5	0.2		0.2	0.18	0.22	0.21	0.01	0.01	0.01	1.05
ADIPOSE	11.4	59.8	0.7	27.8	0.1			0.1	0.1					0.95
LUNG	10.3	10.5	3.1	74.9	0.2		0.2	0.3	0.3	0.2				0.26
MUSCLE	10.2	14.3	3.4	71	0.1		0.2	0.3	0.1	0.4				1.05
SKIN	10	20.4	4.2	64.5	0.2		0.1	0.2	0.3	0.1				1.09
CARTILAGE	9.6	9.9	2.2	74.4	0.5		2.2	0.9	0.3					1.1
BONE	3.4	15.5	4.2	43.5	0.1	0.2	10.3	0.3			22.5			1.92
RED BM	10.5	41.4	3.4	43.9			0.1	0.2	0.2			0.1		1.03
YELL BM	11.5	64.4	0.7	23.1	0.1			0.1	0.1					0.98

BW = Bone Marrow; YELL = Yellow

APPENDIX D

Photon Plan Summary for Left Breast

APPENDIX D-1: Beam Information for 6 MV

Beam	F1 306	F2 131	F3 ISO MED	F4 ISO ANT
Beam number	1	2	3	4
Treatment Unit	Synergy 11	Synergy 11	Synergy 11	Synergy 11
Radiation Type	Photon	Photon	Photon	Photon
Energy	6 MV	6 MV	6 MV	6 MV
Fraction Group	1	1	1	1
Number of Fractions	25	25	25	25
MU or min Fraction	201.87	200.66	0.00	0.00
FX (cm)	17.7	17.7	17.7	17.7
FY (cm)	10.7	10.7	10.7	18.3
FEX1 (cm)	-8.0	-9.7	-8.0	-9.7
FEX2 (cm)	9.7	8.0	9.7	8.0
FEY1 (cm)	-5.9	-5.9	-5.9	-10.6
FEY2 (cm)	4.8	4.8	4.8	7.7
MLC	MLCX	MLCX	MLCX	MLCX
Isocenter X (cm)	9.7	9.7	9.7	9.7
Isocenter Y (cm)	0.3	0.3	0.3	0.3
Isocenter Z (cm)	10.3	10.3	10.3	10.3
Table Top Lateral (cm)	-9.7	-9.7	-9.7	-9.7
Table Top Longitudinal (cm)	-0.3	-0.3	-0.3	-0.3
Table Top Vertical (cm)	-10..3	-10..3	-10..3	-10..3
SSD (cm)	94.1	93.8	94.1	96.2
Depth of isocenter	5.9	6.2	5.9	3.8
Gantry (degrees)	306	131	306	0
Collimator (degrees)	90	270	90	270
Couch (degrees)	0	0	0	0
Algorithm	CC (GPU)	CC (GPU)	CC (GPU)	CC (GPU)
Inhomogeneity correction	On	On	On	On

APPENDIX D

Photon Plan Summary for Left Breast

APPENDIX D-1: Beam Information for 6 MV

Beam	F1 306	F2 131	F3 ISO MED	F4 ISO ANT
Beam number	1	2	3	4
Treatment Unit	Synergy 11	Synergy 11	Synergy 11	Synergy 11
Radiation Type	Photon	Photon	Photon	Photon
Energy	6 MV	6 MV	6 MV	6 MV
Fraction Group Number	1	1	1	1
Number of Fractions	25	25	25	25
MU or min Fraction	201.87	200.66	0.00	0.00
FX (cm)	17.7	17.7	17.7	17.7
FY (cm)	10.7	10.7	10.7	18.3
FEX1 (cm)	-8.0	-9.7	-8.0	-9.7
FEX2 (cm)	9.7	8.0	9.7	8.0
FEY1 (cm)	-5.9	-5.9	-5.9	-10.6
FEY2 (cm)	4.8	4.8	4.8	7.7
MLC	MLCX	MLCX	MLCX	MLCX
Isocenter X (cm)	9.7	9.7	9.7	9.7
Isocenter Y (cm)	0.3	0.3	0.3	0.3
Isocenter Z (cm)	10.3	10.3	10.3	10.3
Table Top Lateral (cm)	-9.7	-9.7	-9.7	-9.7
Table Top Longitudinal (cm)	-0.3	-0.3	-0.3	-0.3
Table Top Vertical (cm)	-10..3	-10..3	-10..3	-10..3
SSD (cm)	94.1	93.8	94.1	96.2
Depth of isocenter	5.9	6.2	5.9	3.8
Gantry (degrees)	306	131	306	0
Collimator (degrees)	90	270	90	270
Couch (degrees)	0	0	0	0
Algorithm	CC (GPU)	CC (GPU)	CC (GPU)	CC (GPU)
Inhomogeneity correction	On	On	On	On

APPENDIX D-2: Beam Information for 1.25 MeV

Prescription 5000.0 cGy to the 100.0% isodose line
Normalization: Isocenter
Calculation Model: Fast Photon
Heterogeneity Correction Model: none

Max Isodose	119.7 @ (3.44, 0.00, 1.83)	
Beam #	1	2
Name	Med Tang	Lat Tang
Machine	Equinox 100 Cob	Equinox 100 Cob
Energy	Co-60 1.25 MeV	Co-60 1.25 MeV
Blocks	No	No
Wedge Name	--	--
Wedge Angle	--	--
Gantry (Start^0, Stop^0)	305.3	129.4
Couch (^{0})	0.0	0.0
Couch (Lat, Vert, Long)	-9.60, -16.40, 3.5	-9.60, -16.40, 3.5
Isocenter (X, Y, Z)(cm)	2.41, 0.00, 0.28	2.41, 0.00, 0.28
Dose to Isocenter (cGy)	2395.83	2604.17
Fit (Volume, Margin)	none	none
SSD (cm)	96.0	87.5
Collimator (^{0})	0.0	0.0
Field Size (cm)	6.8 x 17.4	6.8 x 17.4
Jaw 1 (cm)	X1:3.4 X2: 3.4	X1:3.4 X2: 3.4
Jaw 2 (cm)	Y1: 8.7 Y2: 8.7	Y1: 8.7 Y2: 8.7
Depth (cm)	7.50	6.50
Effective Square (cm)	9.78	9.78
TPR	0.781	0.819
RCS	0.998	0.998
RPS	0.999	0.999
Wedge Factor	1.000	1.000
Inverse Square	1.010	1.010
Accessory Trans. Factor	1.000	1.000
Total OCR	1.000	1.000
Primary OCR	1.000	1.000
Block Edge OCR	1.000	1.000
Coll Edge OCR	1.000	1.000
Wedge OCR	1.000	1.000
Weight Point	Isocenter	Isocenter
Total Weight	0.9	1.0
Dose to Weight Point (cGy)	95.8	104.2
Dose at dmax (cGy)	138.9	143.9
Number of Fractions	25	25
Machine Settings/Rx	1.37 Min	1.42 Min

APPENDIX E

Quadrants of MCNP

APPENDIX E-1: Reference plane section into smaller volumes

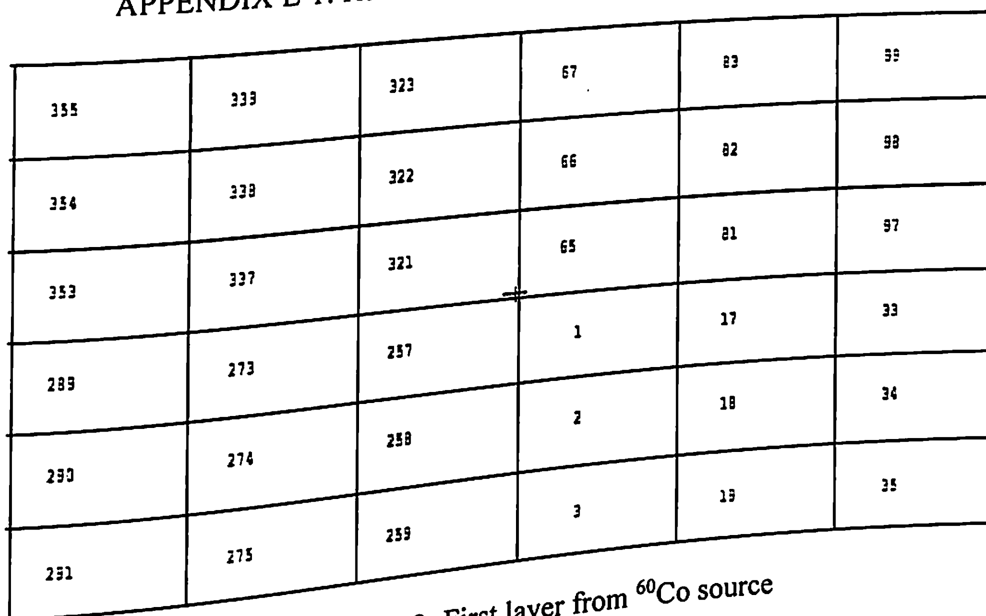

APPENDIX E-2: First layer from ^{60}Co source

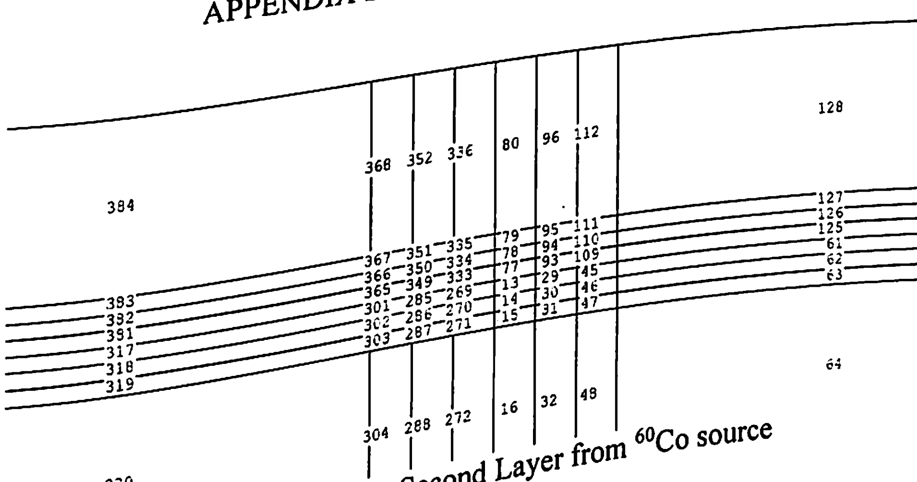

APPENDIX E-3: Second Layer from ^{60}Co source

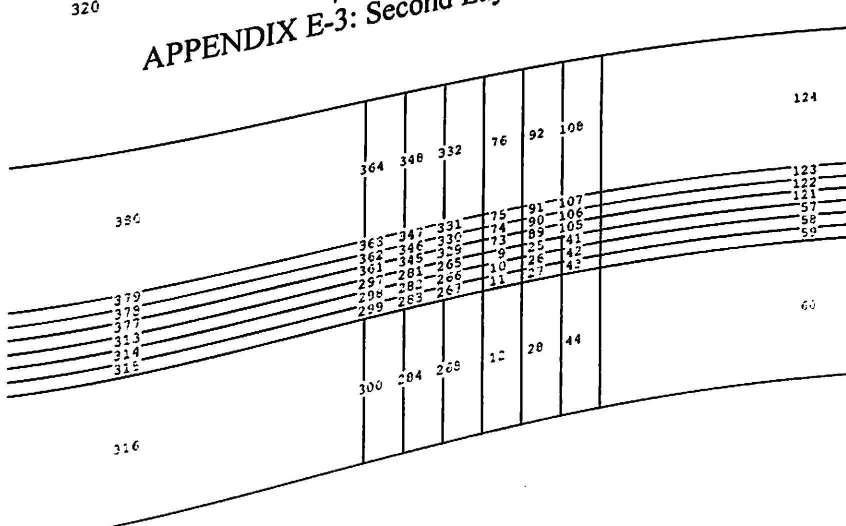

APPENDIX E-4: Third Layer from ^{60}Co source

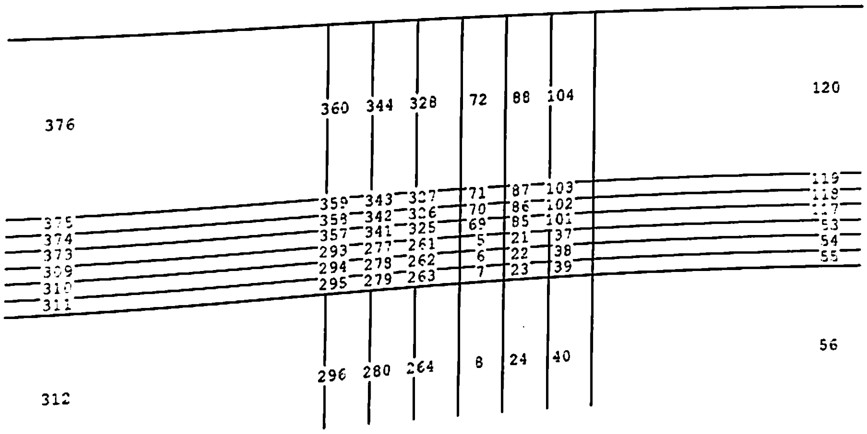

APPENDIX E-5: Fourth Layer from ^{60}Co source

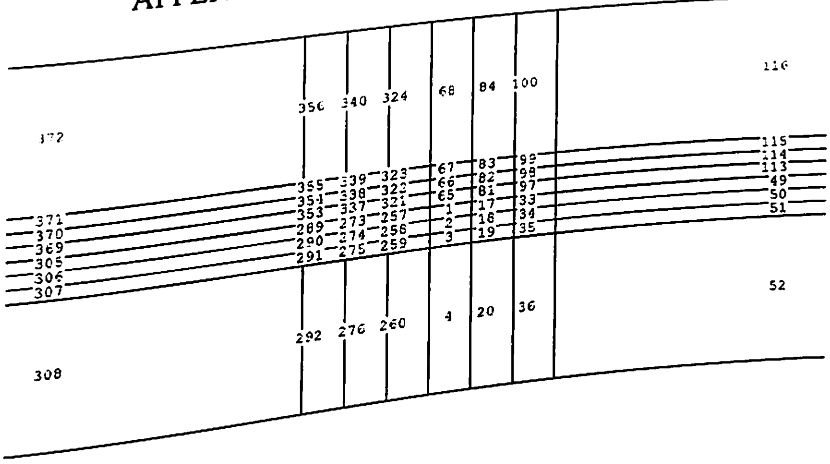

APPENDIX E-6: Fifth Layer from ^{60}Co source

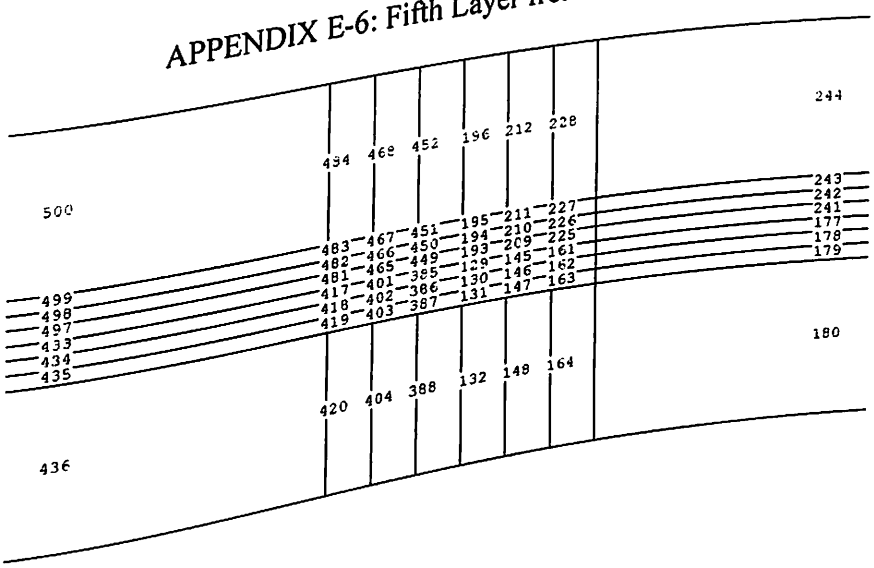

Appendix E-7: Sixth Layer from ^{60}Co source

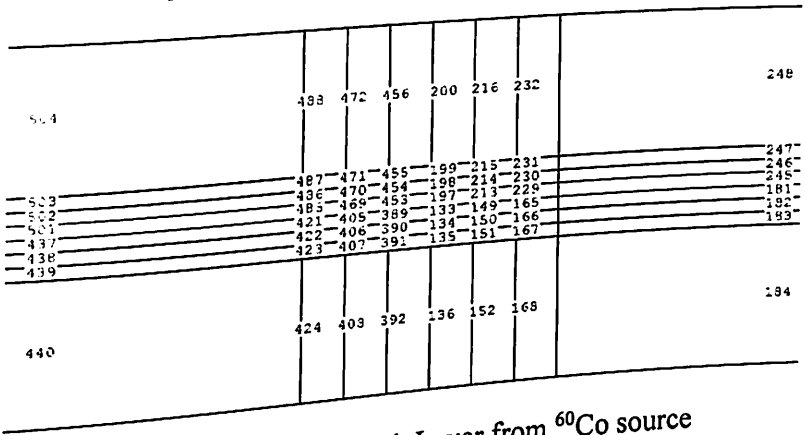

Appendix E-8: Seventh Layer from ^{60}Co source

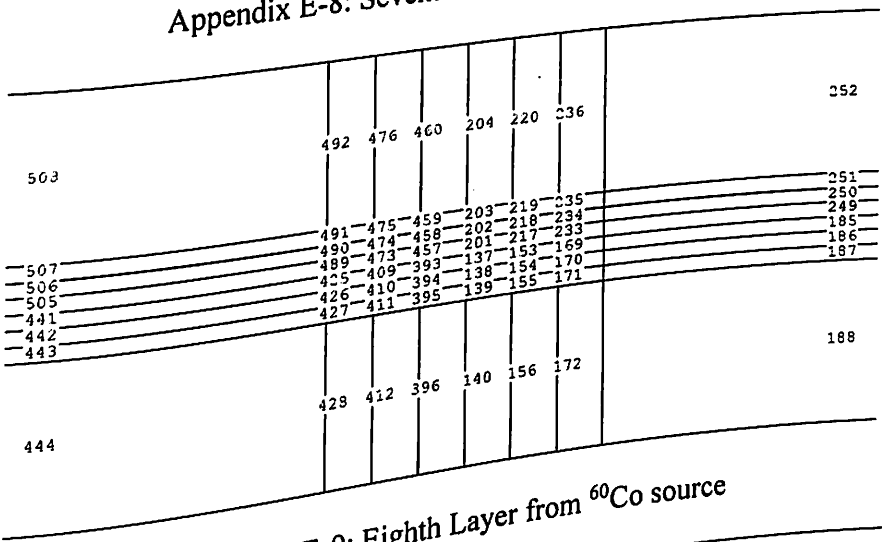

Appendix E-9: Eighth Layer from ^{60}Co source

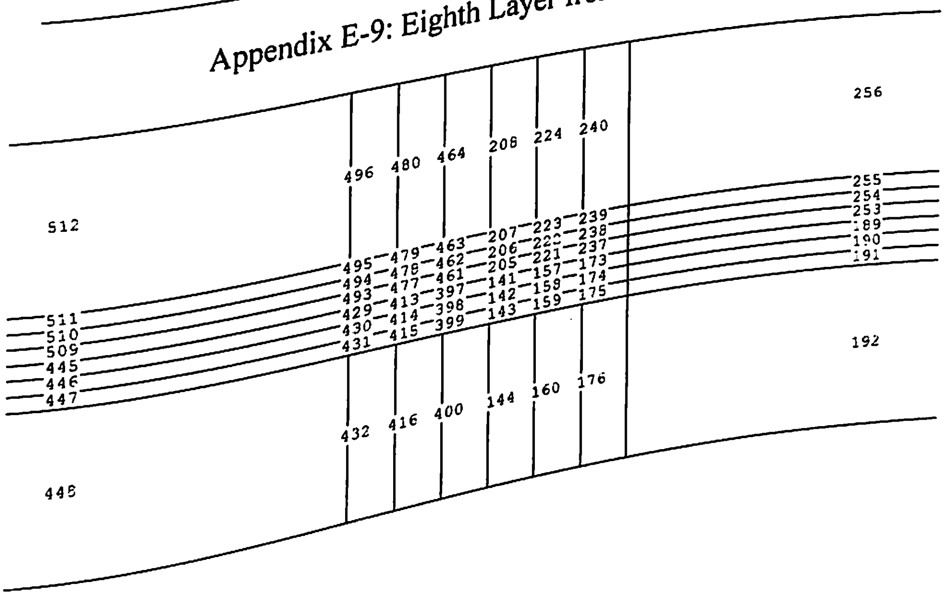

APPENDIX F

Optical Densities of the Energy Beams

Dose (cGy)	Co-60	6 MV	15 MV
	Optical Densities (OD)		
0	0	0	0
20	0.047971	0.036531	0.038911
40	0.074806	0.066308	0.070285
80	0.120504	0.123293	0.122612
160	0.194716	0.176291	0.198248
240	0.242666	0.225176	0.250528
320	0.271828	0.278932	0.269145
400	0.281328	0.302995	0.304166
500	0.308496	0.334302	0.302827

APPENDIX G

Dose Measurement with Ionization Chamber

	1.25 MeV		6 MV		15 MV	
Dose (Gy)	TT (min)	Measured (nC)	TT (MU/100)	Measured (nC)	TT (MU/100)	Measured (nC)
0.2	0.21	3.265	20.06	3.481	20.52	3.9735
0.4	0.43	6.857	40.12	6.966	41.04	7.361
0.8	0.85	13.876	80.23	13.935	82.07	14.715
1.6	1.70	26.471	160.47	27.895	164.15	29.435
2.4	2.55	40.990	240.70	42.040	246.22	44.17
3.2	3.40	55.042	320.93	56.030	328.29	58.91
4.0	4.26	66.804	401.17	70.000	401.37	73.64
5.0	5.32	85.892	501.46	87.500	512.96	92.20

PUBLISHED ARTICLES FROM THESIS

1. Theresa Dery, Joseph Amoako, Paul Buah-Bassuah, William Osei-Mensah. (2018). Virtual Simulation of Co-60 Gamma Ray Beam Geometry International Journal of Sciences: Basic and Applied Research (IJSBAR). 38(2), 116-122.
2. Dery, TB, Amoako, JK, Buah-Bassuah, PK. (2018). Evaluation of Scanner Response with Radiochromic EBT3 Film in Radiation Therapy. IJSRST1845459. 4(5): 1646-1649

International Journal of Sciences: Basic and Applied Research (IJSBAR)

ISSN 2307-4531
(Print & Online)

http://gssrr.org/index.php?journal=JournalOfBasicAndApplied

Virtual Simulation of Co-60 Gamma Ray Beam Geometry

Theresa Dery[a*], Joseph Amoako[b], Paul Buah-Bassuah[c], William Osei-Mensah[d]

[a]*Radiological and Medical Sciences Research Institute, GAEC, Box LG 80, Legon, Accra, Ghana*

[b]*Radiation Protection Institute, GAEC, Box LG 80, Legon, Accra, Ghana*

[a,c]*Department of Physics, University of Cape Coast, Cape Coast, Ghana*

[d]*National Nuclear Research Institute, GAEC, Box LG 80, Legon, Accra, Ghana*

[a]*Email: theresadery2000@gmail.com*

Abstract

Radiotherapy forms an essential part in the increase survival and relieve of cancer globally. Tumoricidal dose are delivered to cancerous tumours conformal as practically achievable. Radiation delivery mode, dosimetric verification and quality assurance play a key role in prior to patient treatment. The focus of this study is to present a modality for ensuring good quality control prior to treatment delivery using Cobalt (^{60}Co) source. In the study, absorbed dose to water is computed in a virtual phantom with approximate full scatter conditions with gamma as the radiation source. Monte Carlo Neutron Photon (MCNP) code system was used to simulate the properties of the system geometry of the phantom following the International Atomic Energy Agency (IAEA) Technical Report Series 398 protocol. The research was limited to the use of virtual simulation of water phantom for the Cobalt-60 treatment unit. This work provides information recommended for photon energy according to the medical situation at the radiotherapy facilities in Ghana.

Keywords: Radiotherapy; Monte Carlo; Virtual Phantom; Cobalt -60.

1. Introduction

The amount of radiation dose delivered to the target and surrounding tissues is one of the major predictors of radiotherapy treatment outcome. This could be achieved by conforming the dose distribution to the shape of the intended target whilst minimizing radiation to normal tissues in close proximity.

* Corresponding author.

It is non-invasive and allows for sparing of normal healthy tissues and dose escalation [1]. A physical phantom or a computational phantom that mimics human anatomical features could be used to derive the irradiation dose inside the body. In *in-vivo* dosimetry with Monte Carlo (MC) could be used as a quality assurance (QA) tool for treatment planning systems (TPS) in therapy. Quality assurance in the radiotherapy treatment planning process is essential for minimizing the possibility of undue exposure [2]. This approach is to monitor the radiation dose in radiation facility, which would serve as a safety measure to estimate the e xtremity dose to patients during treatment where avoidance of high radiation exposure is the ultimate goal. The IAEA TRS398 protocol used for beam calibration in terms of absorbed dose to water of ^{60}Co was employed. This is because a number of countries still use the Co-60 sources for treating cancers and also the gamma ray source has a significant part of low energy scattered photons, which originates in the source itself or in the treatment head [3].

2. Method

A gamma source of mean energy 1.25 MeV (^{60}Co) was used as the radiation source in the Monte Carlo simulation. A water (H_2O) phantom was used as the reference medium for measurement of absorbed dose for photon beams as recommended by the IAEA code of practice [3]. As the beam incident on the phantom, t he absorbed dose varies dependent on the beam energy, depth, field size and distance from the source and beam collimation system [4, 5]. Thus, the modelling of the dose in the phantom considered the variations that affect dose distribution. The field size used was 10 cm x 10 cm and distance from the source was 100 cm. Figure 1 shows the experimental setup of the irradiation geometry used for the determination of absorbed dose to water procedure adopted by IAEA TRS398 in the radiation field.

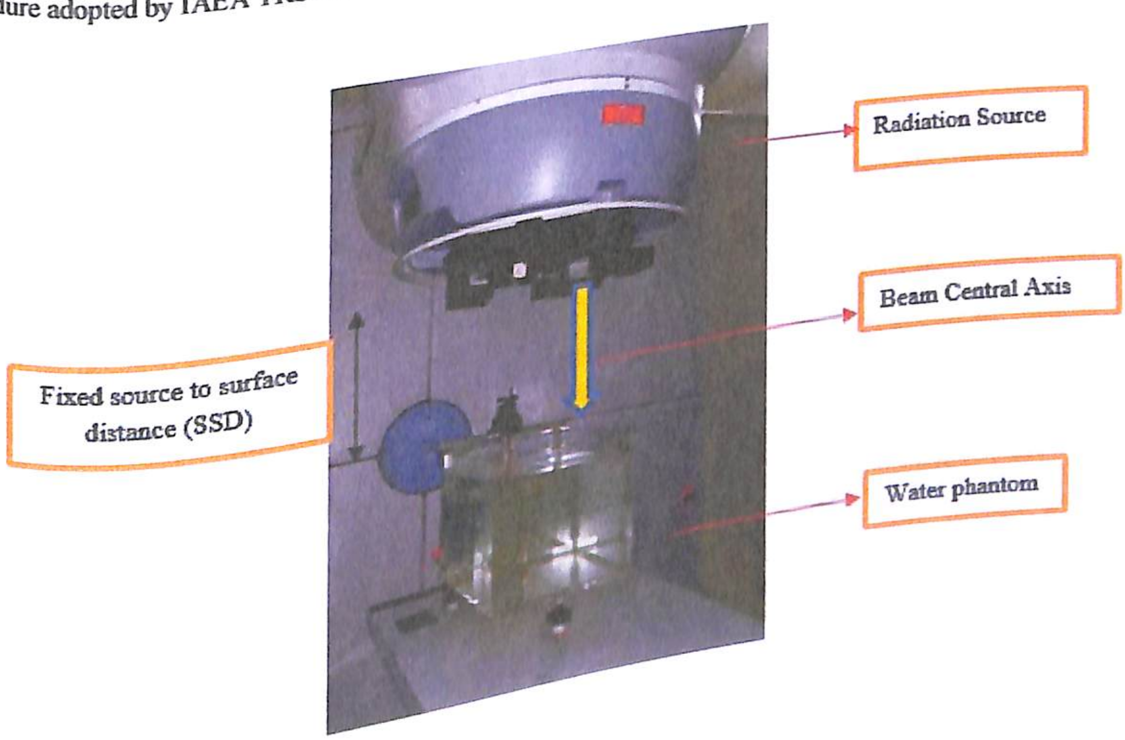

Figure 1: Setup for irradiation geometry for beam calibration

A photon virtual source was used for simulating the arbitrary beam distribution using Monte Carlo code. The MCNP code was used because of its ability to simulate any 3D geometry with precision. The simulated virtual phantom used has the same absorption and scatter properties as water. The code sectioned or meshed the 1000 cm^3 water phantom into 25,000 smaller volumes for which the dose for every volume element (i.e. voxel) could be calculated. The meshing of the phan tom were 50x50x10 in x, y and z-planes respectively. The results of the dose in the z-plane were plotted using M ATLAB. Figures 2 and 3 shows the 3D and 2D geometric view of the water phantom and the source respectively.

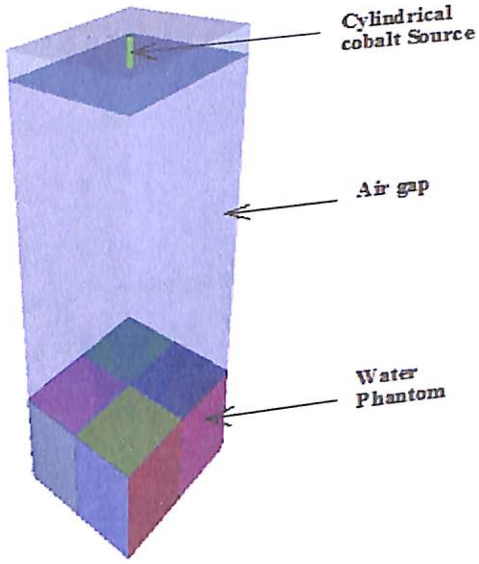

Figure 2: MCNP 3D geometric view of simulated virtual phantom

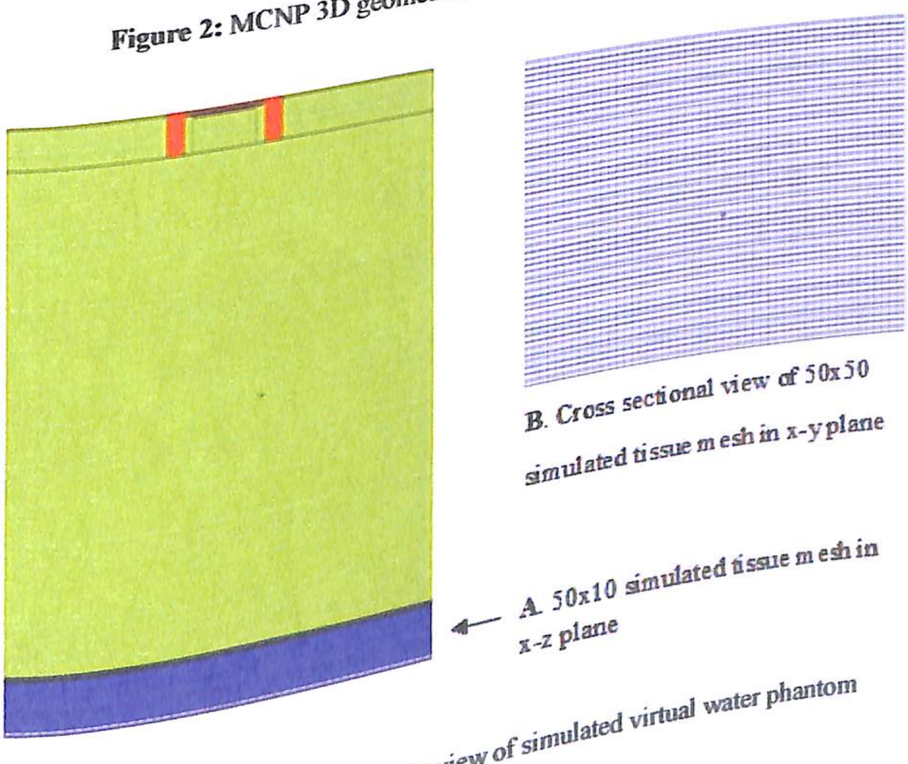

Figure 3: MCNP 2D geometric view of simulated virtual water phantom

Cylindrical geometries were employed for modelling of the source holders while planer geometries were used for the virtual water phantom. The gamma source was specified as surface source, collimated beam and mono-energetic source energies with uniform distribution of radioactive. The gamma source was modelled to emit photons perpendicular to the phantom, parallel in direction of cylinders containing the source in direction of z - plane. These hypothetical source energies were assumed as a disc with 1.5 cm diameter (not to real size) and parallel to x-y plane. Materials constituting the geometric setup were stainless steel, water and air. The elemental composition of the source holder was stainless steel 316L. Whilst that of the water in the phantom constituted hydrogen and oxygen (H_2O) and air was used to fill the gaps in the geometry. The Co-60 source strength at the time of the experimental measurement is used to determine the number of photons emitted by the source per second. The strength of the source and its associate d photons together with dose conversion tables in reference according to IAEA TRS398 are used to calculate the dose per each cell.

3. Results and Discussion

Figure 4a-c show the results of the spatial distribution of absorption events of the energy deposited per photon in the z-plane using Matlab. The z-plane was sectioned into ten layers representing the different distance from the surface with each layer having 25,000 voxels.

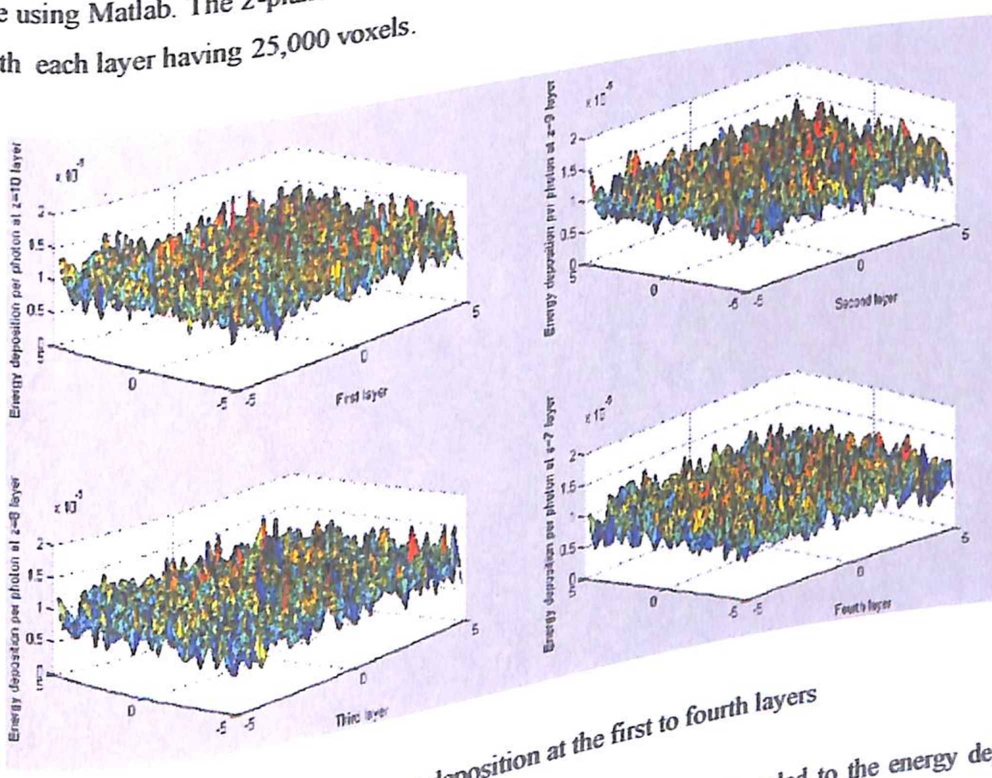

Figure 4a: Energy deposition at the first to fourth layers

From the results, it was observed that the first layer in the MCNP corresponded to the energy deposited per photon at z=10 in the meshed layers in Matlab. The highest peaks in each of the layers shows where the ...ceived. The model computed the dose in each voxel in each layer by ...probability theory of interacting with the virtual phantom ...ing the precise location of a tumour by

Cylindrical geometries were employed for modelling of the source holders while planer geometries were used for the virtual water phantom. The gamma source was specified as surface source, collimated beam and mono-energetic source energies with uniform distribution of radioactive. The gamma source was modelled to emit photons perpendicular to the phantom, parallel in direction of cylinders containing the source in direction of z - plane. These hypothetical source energies were assumed as a disc with 1.5 cm diameter (not to real size) and parallel to x-y plane. Materials constituting the geometric setup were stainless steel, water and air. The elemental composition of the source holder was stainless steel 316L. Whilst that of the water in the phantom constituted hydrogen and oxygen (H_2O) and air was used to fill the gaps in the geometry. The Co-60 source strength at the time of the experimental measurement is used to determine the number of photons emitted by the source per second. The strength of the source and its associate d photons together with dose conversion tables in reference according to IAEA TRS398 are used to calculate the dose per each cell.

3. Results and Discussion

Figure 4a-c show the results of the spatial distribution of absorption events of the energy deposited per photon in the z-plane using Matlab. The z-plane was sectioned into ten layers representing the different distance from the surface with each layer having 25,000 voxels.

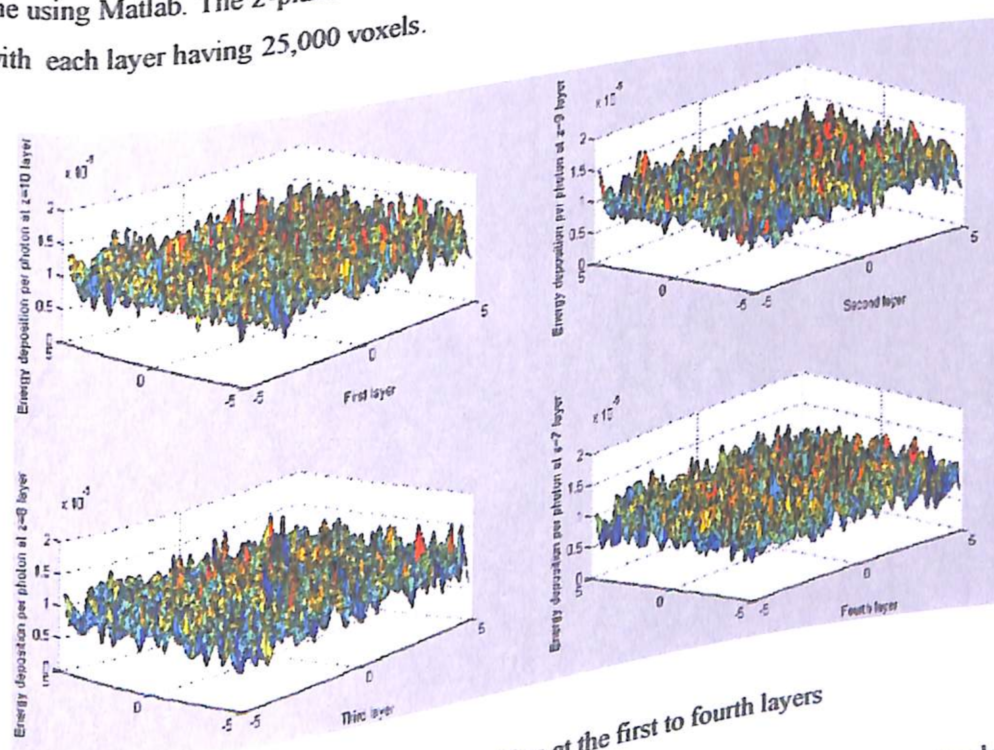

Figure 4a: Energy deposition at the first to fourth layers

From the results, it was observed that the first layer in the MCNP corresponded to the energy deposited per photon at z=10 in the meshed layers in Matlab. The highest peaks in each of the layers shows where the maximum dose was absorbed and acheived. The model computed the dose in each voxel in each layer by transporting several millions of particles based upon probability theory of interacting with the virtual phantom mimicking the patient. This is because radiotherapy involves finding the precise location of a tumour by optimizing the intensity of the radiation and the orientations of the beams shaped to match the plan delineation of the tumour. The simulation model was able to calculate the set of radiation intensities that pass through the phantom for a desired dose distribution mimicking exactly what happens to patient during treatment .

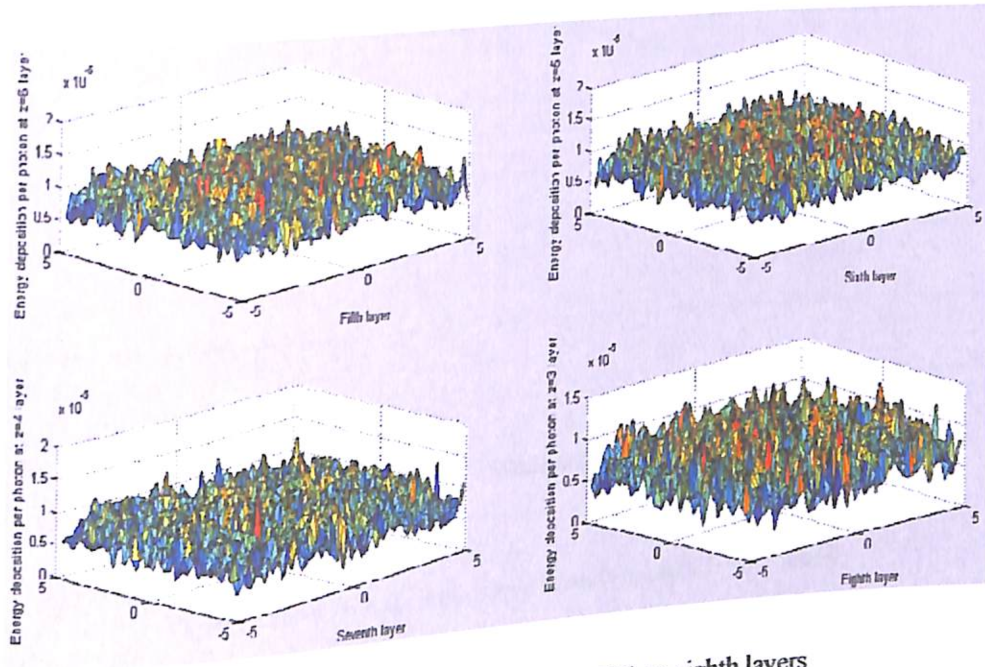

Figure 4b: Energy deposition at the fifth to eighth layers

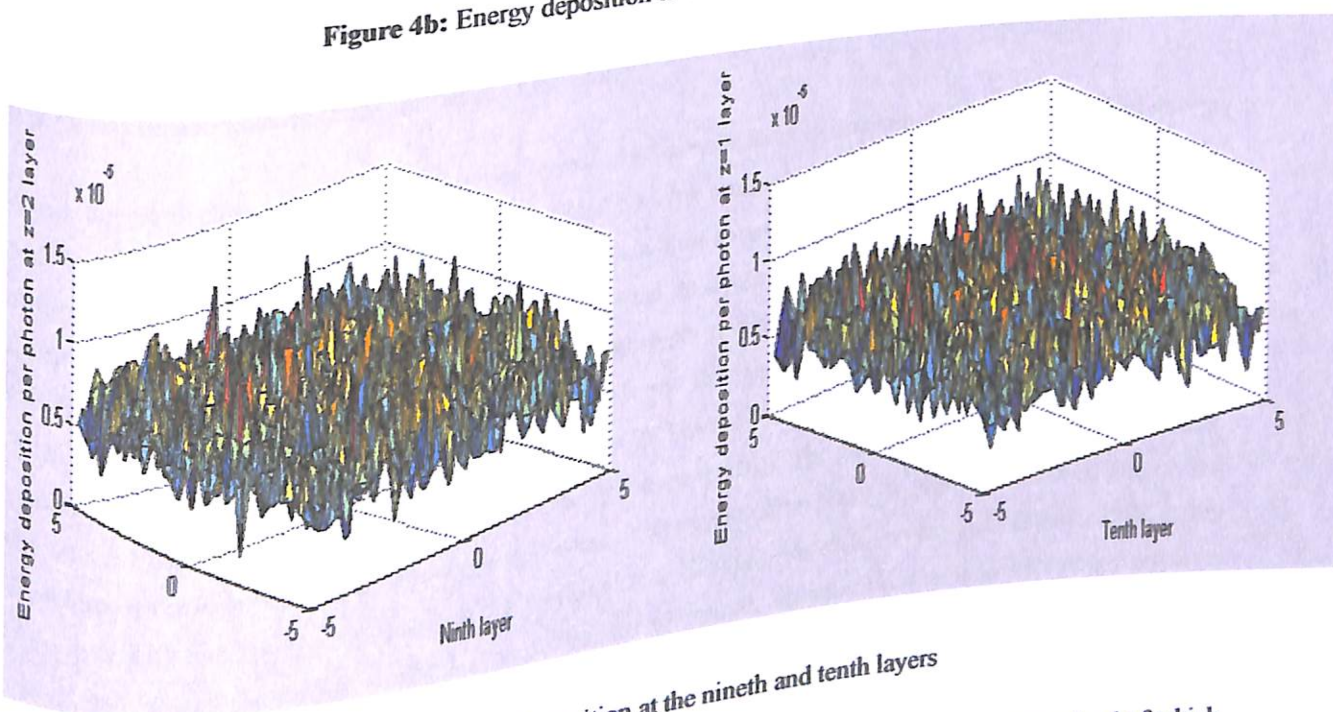

Figure 4c: Energy deposition at the nineth and tenth layers

Based on the results from the simulation a linear response in each layer in the z-plane was determined of which the radiation dose could be accurately estimated. Figure 5 shows a correlation graph which indicates the linear relationship between the response variable (relative absorbed dose) and the predicator (layer number) representing the different distance from the surface within the virtual phantom.

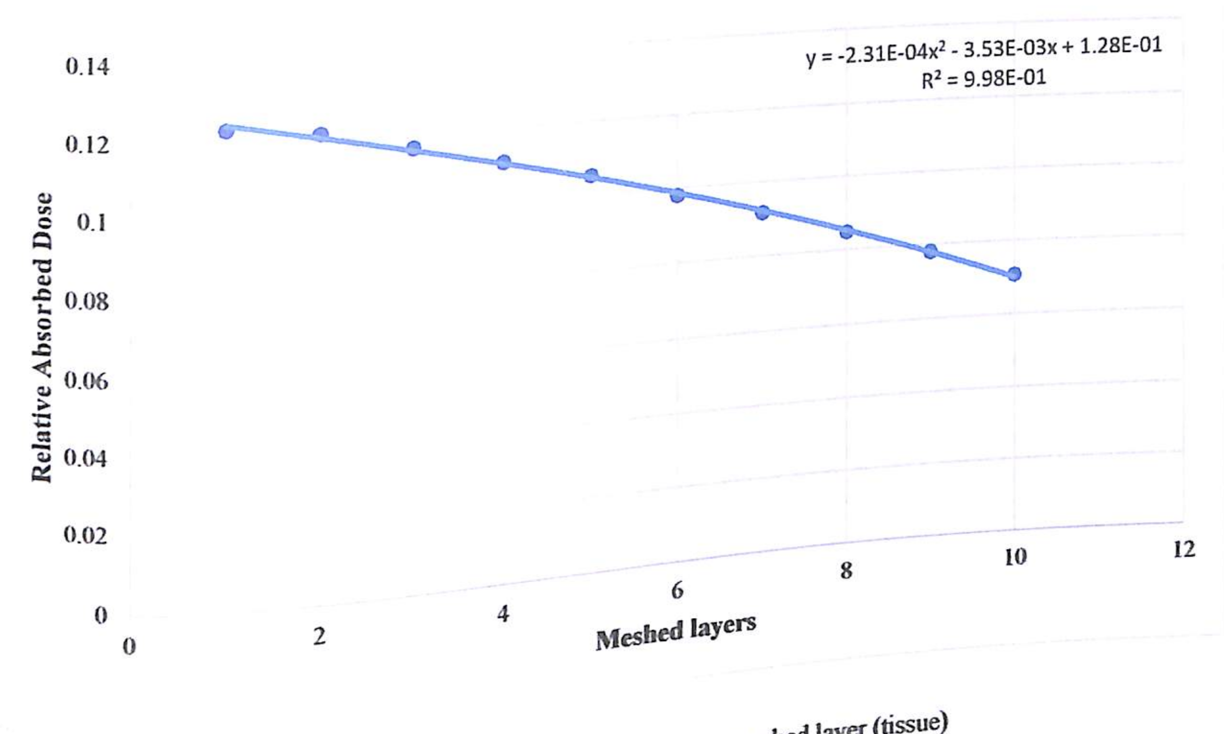

Figure 5: Relative absorbed dose in each meshed layer (tissue)

In Figure 5, the graph gives information on the goodness of the model. The coefficient of determination (R^2) value of 0.998 indicates that the regression line fits the data perfectly with the significance value ($p <$ 0.050) less than indicating strong evidence of the model.

Again, the graph shows the estimated regression model of the relationship between the rel ative absorbed dose in each layer within the virtual phantom using Co-60 teletherapy machine. The layers represents the summation of all the different points located in the different direction within a particular section of the phantom. From Figure 5, the first layer received the highest/maximum absorbed dose while the tenth layer received the lowest dose signifying that, as the photon energy with shorter wavelength passes through the material, the doses at different distances from the surface also changes. The different layers did not absorb the same dose. The non-uniformity of radiation distribution within the virtual phantom might have resulted in the size, location, and composition variations. The absorbed dose was greater at the entrance surface than those deeper within the phantom. Therefore, it could be stated that for a given photon, it absorption dependent on the pentration ability, on the material density to be used and the size of the exposed area. The dose distribution estimated to the various layers within the phantom (virtual) is useful for predicting the therapeutic value in determining the safety treatment outcome for the patient represented by the virtual phantom. It is therefore necessary to precisely know the dose deposited at any point within the body of a patient during radiation therapy as part of dose optimization. The Monte Carlo used for the simulation ensured the estimated dose precision in the therapy of cancer with radionuclides as reported by Sonia and his colleagues [6].

4. Conclusion

The MCNP focused on predicting the dose by calculating the photons that pass through the phantom. The dose values were determined at many points under varying treatment conditions such as field size, source to surface distance and the beam energy. The study provided a theoretical model to predict the dose distribution in each point of the phantom mimicking the tissues in the body during external beam treatment using Co-60 source. The study also demonstrated the advantage of using MCNP as a readily tool that accurately describes the radiation therapy system. Therefore, it is envisaged that with improved algorithms in Monte Carlo, it would be the method simulation technique for radiation therapy.

5. Recommendation

It is recommended that the simulation results should be compared with measured experimental measurements to validate the theoretical results.

Acknowledgements

I am grateful to Ghana Education Trust Fund and the Department of Physics, University of Cape Coast, Ghana for their immense contribution and support.

References

[1] G. Baker. "Localization: conventional and CT simulation." British Journal of Radiology, vol. 79, 36-49, 2006.

[2] IAEA. "Commissioning and Quality Assurance of Computerized Planning Systems for Radiation Treatment of Cancer." IAEA Technical Report Series, 430, 2004.

[3] IAEA. "Absorbed Dose Determination in External Beam Radiotherapy." Technical Report Series No. 398 (TRS-398), 2000.

[4] M.F. Khan. "The Physics of Radiation Therapy." 2nd ed., Williams and Wilkins, A Wolters Kluwer Company, London, 1994.

[5] M.F. Khan. "The Physics of Radiation Therapy." 4th ed., Lippincott Williams and Wilkins, London, 2010.

[6] M.R. Sonia, M. Eman, S.H. Magda, I.B. Ibrahem, and A.A.Esmat. "Monte Carlo Dose Calculations for Breast Radiotherapy Using ^{60}Co Gamma Rays." Journal of Nuclear and Radiation Physics, vol. 1, 61-72, 2006.

© 2018 IJSRST | Volume 4 | Issue 5 | Print ISSN: 2395-6011 | Online ISSN: 2395-602X
Themed Section: Science and Technology

Evaluation of Scanner Response with Radiochromic EBT3 Film in Radiation Therapy

Dery, TB[1], Amoako, JK[2], Buah-Bassuah, PK[3]

*[1]Radiological and Medical Sciences Research Institute, Ghana Atomic Energy Commission, Accra, Ghana

[2]Radiation Protection Institute, Ghana Atomic Energy Commission, Accra, Ghana

[3]Department of Physics, University of Cape Coast, Cape Coast, Ghana

ABSTRACT

The study quantified the performance and evaluated a flatbed scanner, Epson Stylus CX5900 used for scanning the radiochromic EBT3 films for dosimetry with two other widely used commercial scanners. The performance of each scanner was based on constancy and uniformity. Scanners were tested using film irradiated with doses ranging from 0-500 cGy using 1.25 MeV cobalt-60 isotope. Image J software was used for analysing the scanners. The average dose discrepancy (δ) in percentage of the delivered dose was 0.65 % and standard deviation (σ) of 0.92 for the Epson Stylus CX5900 Scanner.

Keywords: Scanner; Cobalt-60; EBT3 film; Dosimetry; Calibration

I. INTRODUCTION

The radiochromic film widely used is targeted to the measure the absorbed doses of ionizing radiation in for high energy photons, electron and proton beams [1, 2]. Moreover, the radiochromic film shows low linear energy transfer (LET) and energy dependence over a wide range of beam energies used in radiation therapy [3, 4, 5]. EBT3 film is a new type of film which serves as radiation detector in radiation therapy with greater uniformity of less than 1% [6] and within 1.5% according to Reinhardt et al., [7]. The film provides significant performance in the dose range up to 10 Gy, and it is a nearly tissue equivalent that develops blue when irradiated with absorption maxima at approximately 633nm. The EBT3 optical density changes stabilizes rapidly within 2 hours of waiting time window [6]. The film consists of H (56%), C (27.6%), O (13.3%), Al (1.6%) and Li (0.6%) with effective atomic number of 7.26 [8]. EBT3 films are comparatively hardy sturdy with the active layer protected on both sides by clear polyester film substrates. The active layer incorporates a yellow dye, decrease ultraviolet and light sensitivity that enables multi-channel dosimetry. This allows the film to be immersed in water for a short periods and handled by the edges according to the recommendation of the manufacturer's specification. The recommended protocol procedure for radiometric film dosimetry described by the AAPM TG-55 Report 63 [5, 9] was used for the study. Gafchromic EBT3 film is symmetrical, therefore it can be scanned with either side facing the light source on the flatbed colour scanner. The symmetric layer configuration of the film allows the elimination side orientation dependence, and the presence of microscopic silica particles embedded into the polyester substrate prevents the formation of Newton's rings in images obtained using a flatbed scanner [10]. This study was conducted to investigate and evaluate scanners appropriate for EBT3 dosimetry. This is important because the number of photons reaching the EBT3 film is a function of the intensity of the radiation and the time that the film is exposed to the radiation. The type of scanner to be used is in scanning the film is essential.

II. METHODS AND MATERIAL

The GafChromic EBT3 with product code 828206, from Ashland Speciality Ingredients was the dosimeter used in the study. The EBT3 used has 10 films per box and dimensions of 12.8 x 14.7". The sheet (12.8 x 14.7") of the EBT3 film was cut into rectangular pieces of dimensions 2 cm x 3 cm for easy orientation by using a sharp scissor.

A water phantoms made of PMMA was used for the film calibration irradiation for Cobalt-60. The field size used for the irradiation of the films was 10 cm x 10 cm at the isocenter and the source to surface distance (SSD) was set at 100 cm for cobalt-60 treatment machine.

The EBT3 films were placed perpendicular to the beam central axis at a depth of 5 cm in the water phantom. Correction and scaling factors was corrected for in the water phantom. One of the pieces of the film was placed in the water phantom and were exposed at dose range of 0 - 500 cGy for dose levels of 0, 20, 40, 80, 160, 240, 320, 400, 500 cGy as shown in Figure 1. The dose values were calculated and converted to treatment time (TT) according to the relation as:

$$TT = \frac{Prescribed\,Dose}{Percentage\,Depth\,Dose * Dose\,Rate * Scatter\ factor} \quad (1)$$

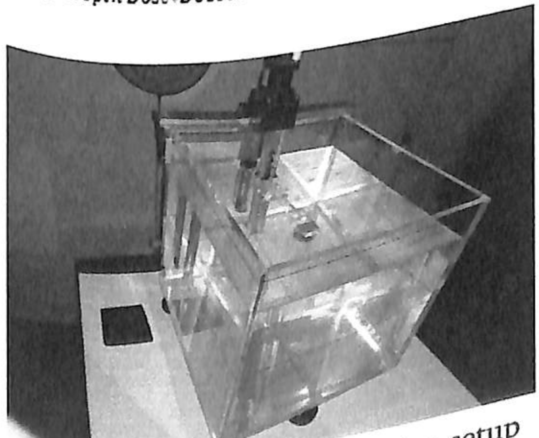

Figure 1: EBT3 film irradiation setup

Digitization

Three different scanners (Epson Stylus CX5900, Scanner A and Scanner B) were used to evaluate an appropriate scanner in scanning the EBT3 films. The EBT3 films were stored in a dark location until it was scanned. All the films were scanned in the landscape orientation in order to reduce variations within the film as recommended by the manufacturer and Menegotti et al., [11]. The films were positioned in the centre of the scanner in the direction perpendicular to the scan direction. Uniformity test at a reproducible central location on the scan surface was checked. This was checked by placing the unexposed films on the scanner and scanned. To keep track of orientation, the exposed films were labelled A, B, C, D, E, F, G, and H at the bottom left corner which corresponded to the doses of 20, 40, 80, 160, 240, 320, 400, 500 cGy respectively for the photon of energies 1.25 MeV. The EBT3 film scanned image saved in tagged image file format (TIFF) was split into red, green and blue component using image processing software, Image J Image J1.46r (64 bit) (National Institute of Health, Bethesda, MD). A region of interest (ROI) of 0.4 cm x 0.6 cm was chosen for each scanned image and colour channel.

The relationship between the dose to the film and the response when the film exposed was determined as the sensitometric curve for the beam energy. The curve provides information for the film response conversion. The optical densities of the film response were determined for the scanners used from the mean pixel values from the image data.

The optical density is defined as the $\log_{10} I_0/I$, where is I_0 the light intensity measured in the absence of the film and I is the intensity transmitted through the film in a direction perpendicular to its plane. The optical density of the film scanner response was calculated using the equation:

$$OD = -log_{10}\left(\frac{Mean\ Pixel\ Value_{exposed}}{Mean\ Pixel\ Value\ _{unexposed}}\right) \quad (2)$$

III. RESULTS AND DISCUSSION

Sensitometric Curve

A film sensitometric curve or H-D curve (named after developers Hurter and Driffield) was determined to know the relationship between the applied exposure and the resulting film density. Figure 2 shows the three RGB film characteristics curves with the exposures for the beam energy of 1.2 MeV used.

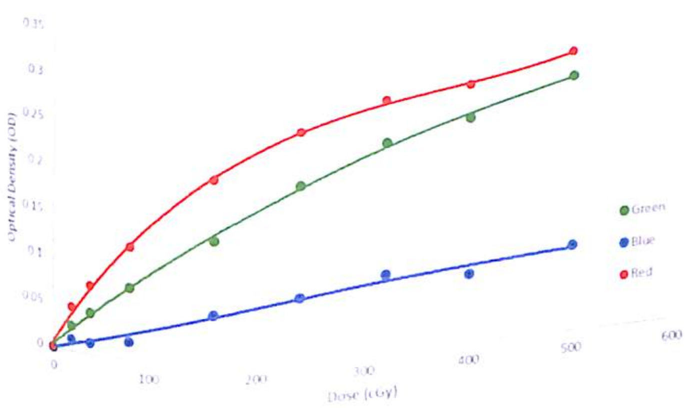

Figure 2: Characteristic Curve for 1.25 MeV Beam Energy

It was observed in Figure 2, that the response curves of the EBT3 film scanned in the red and green channels are above the curve for the blue channel. This results are in agreement with the response curve of EBT film [12]. The red channel showed a relatively high slope because the signal is highly dose dependent than the blue which has a relatively low slope because the signal has weak dose-dependent. Consequently, the red channel exhibited the highest response, therefore the red channel was used for the image analysis of the fit.

The red channel pixel values obtained from the calibration curve were converted into optical density using the 5th order polynomial. The estimated regression equation between the response variable (dose) and the predicator (OD) was used to calculate the absorbed dose delivered and measured from the optical densities of the film.

EBT3 Scanners

Figure 3 shows a plot of the three different scanners studied, and with the scanned images analysed using Image J.

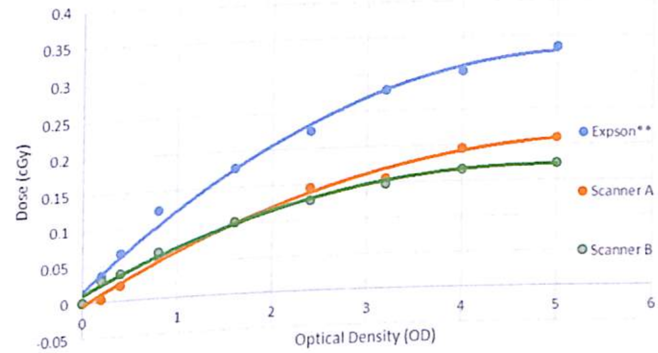

Figure 3: Scanner response

The graph in Figure 3 three shows the optical densities of the Epson Scanner, Scanner A and Scanner B versus the dose delivered. It was observed that all the three scanners had a perfect correlation fit (R^2 >0.99). The Epson Stylus CX5900 showed the greatest response in the spectrum, while Scanner B showed a relative low response. The percentage error (δ) was estimated for the measured dose and the expected doses for Epson Stylus CX5900 Scanner. Table 1 shows the results of the measured doses based on equation 2.

Table 1: Epson scanner response to doses

Expected Dose (cGy)	Measured Dose (cGy)	%Error ($\lvert\delta\rvert$)	Standard deviation (σ)
0	0	0	0
20	19.97499	0. 12521	0.017685
40	39.11834	2.25383	0.623428
80	77.59042	3.10551	1.703830
140	144.8076	3.31999	3.399487

160	157.4514	1.61866	1.802132
320	321.2030	0.37453	0.850649
400	395.7213	1.081241	3.025498
500	496.6558	0.673344	2.364706

The discrepancy δ between the measured dose $D_{measured}$ and the expected dose $D_{expected}$ was calculated according to the relation:

$$|\delta|\ \% = \frac{D_{expected} - D_{measured}}{D_{measured}} \times 100 \qquad (4)$$

δ was calculated for each measurement to estimate the difference between the actually measured, and the calculated dose at the central beam. The average dose discrepancy (δ_{avg}) calculated was 0.645409 % and its standard deviation (σ) of 0.924529. The percentage error calculated was between 0. 13 % and 3.32 %. The standard deviation ranged from 0.02 to 3.40. This might be as a result of lack of uniformity in the scan area, the scanner stability and the response of the film on orientation dependence [12, 13, 14, 15, 16].

Currently, the manufacturers of EBT3 film recommend that a 48-bit (16-bit per channel) flatbed RGB scanner, with FilmQA software should be used for scanning. This is because of the scanner's ability to produce data response in three colour channels, red, green and blue. Epson scanners are particularly recommended due to their large scanning area. The scanning parameters of the flatbed RGB scanner is of resolution of 75 dpi, no colour corrections with a professional scan mode and transparency document type. With the Epson Stylus CX5900 Scanner used, the image type is of 24-bit colour, resolution of 75 dpi, no colour corrections, professional scan mode and a reflective document type. From the results, it was observed that the Epson Stylus scanner used for the study was appropriate in scanning EBT3 films.

Farah et al., performed an experiments with the Varian TrueBeam 1.6 accelerator by was flatbed EPSON 10000 XL and HP Scanjet 4850 in reflection mode to compare the EBT3 film responses of doses up to 500 cGy for both photons and electrons [17]. They concluded that, the reflective scanning method could be used on EBT3 as an economic alternative to the transmission method. In addition, the behavior for doses ranging from 0 to 40 Gy corroborated the results reported by Borca et al. [6] for EBT3 film.

IV. CONCLUSION

The study found the Epson Stylus CX5900 scanner to be an appropriate alternative for film dosimetry with the film providing a reliable relative dose measurement. Different scanners used might not be sensitive to the EBT3 films by introducing errors in the measurements of doses. Therefore, the type of scanners to be used in reading or scanning the EBT3 films is very important.

Additionally, care should be taken to place the film at the center of the scanner bed because the light from the lamp is not emitted evenly and its orientation should be consistent.

The average percentage error for the study measurement was within 1% uniformity as reported by Borca et al., (2013).

V. ACKNOWLEDGEMENT

I am grateful to Ghana Education Trust Fund (GETFund) and the Department of Physics, University of Cape Coast, Ghana for their immense contribution and support.

VI. REFERENCES

[1]. Dreindl R., Georg D. and Stock M.Z. (2014). "Radiochromic Film Dosimetry: Considerations on Precision and Accuracy for EBT2 and EBT3 Type Films," Z. Med. Phys. 24 (2), 153–163.

[2]. Zhao L. and Das I.J. (2010). "Gafchromic EBT Film Dosimetry in Proton Beams," Phys. Med. Biol. 55, 291–301.

[3]. Butson M.J., Cheung T., Yu P.K.N. (2005). Absorption Spectra Variations of EBT

Radiochromic Film from Radiation Exposure. Phys Med Biol., 50(13), N135–N140.

[4]. Chiu-Tsao S.C., Ho Y., Shankar R., Wang L., and Harrison L.B. (2005). Energy Dependence of Response of New High Sensitive Radiochromic Films for Megavoltage and Kilovoltage Radiation Energies. Med Phys., 32(11), 3350–3354.

[5]. Arjomandy B., Tailor R., Anand A., Sahoo N., Gillin M., Prado K., and Vicic M. (2010). Radiochromic Film Dosimetry. Medical Physics Publishing, 37, 1942-1947.

[6]. Borca V.C., Pasquino M., Russo G., Grosso P., Cante D., Sciacero P., Girelli G., La Porta, M.R., and Tofani S. (2013). Dosimetric Characterization and use of GAFCHROMIC EBT3 Film for IMRT Dose Verification. Journal of Applied Clinical Medical Physics, 14(2), 158-171.

[7]. Reinhardt S., Hillbrand M., Wilkens J.J., and Assmann W. (2012). Comparison of Gafchromic EBT2 and EBT3 Films for Clinical Photon and Proton Beams. Med Phys., 39(8), 5257–5262.

[8]. León Marroquin E.Y., Herrera González J.A., Camacho López M.A., Villarreal Barajas J.E., García-Garduño O.A. (2016). Evaluation of the Uncertainty in an EBT3 Film Dosimetry System Utilizing Net Optical Density. Journal of Applied Clinical Medical Physics, 17(5).

[9]. Niroomand-Rad, A., Blackwell, C. R., Coursey, B. M., Gall, K. P., Galvin, J. M., McLaughlin, W. L., . . . Soares, C. G. (1998). Radiochromic film dosimetry: recommendations of AAPM Radiation Therapy Committee Task Group 55. American Association of Physicists in Medicine. Med. Phys, 25(11), 2093–2115.

[10]. Vadrucci M., Esposito G., Ronsivalle C., Cherubini R., Marracino F., Montereali R.M., Picardi L., Piccinini M., Pimpinella M., Vincenti M.A., and De Angelis C. (2015). Calibration of GafChromic EBT3 for Absorbed Dose Measurements in 5 MeV Proton Beam and 60Co?-rays, Medical Physics, 42(8).

[11]. Menegotti L., Delana A., and Martignana A. (2008). Radiochromic Film Dosimetry with Flatbed Scanners: A Fast and Accurate Method for Dose Calibration and Uniformity Correction with Single Film Exposure. Medical Physics, 35(7), 3078–3085.

[12]. Devic S., Tomic N., Soares C.G., and Podgorsak E.B. (2009). Optimizing the Dynamic Range Extension of a Radiochromic Film Dosimetry System. Med Phys., 36(2), 429–437.

[13]. Bouchard H., Lacroix F., Beaudoin G., Carrier J.F., and Kawrakow I. (2009). On the Characterization and Uncertainty Analysis of Radiochromic Film Dosimetry. Med Phys., 36(6), 1931–1946.

[14]. Renade M.K., Li J.G., Dubose R.S., Kozelka J., Simon W.E., and Dempsey J.F. (2008). A Prototype Quantitative Film Scanner for Radiochromic Film Dosimetry. Med Phys., 35(2), 473–479.

[15]. Martisikova M., Ackerman B., and Jäkel O. (2008). Analysis of uncertainties in Gafchromic EBT Film Dosimetry of Photon Beams. Phys Med Biol., 53(24), 7013–7027.

[16]. Paelinck L, De Neve W, De Wagter C. (2007). Precautions and Strategies in Using a Commercial Flatbed Scanner for Radiochromic Film Dosimetry. Phys Med Biol., 52(1), 231–242.

[17]. Farah N., Francis Z., and Abboud M. (2014). Analysis of the EBT3 Gafchromic Film Irradiated with 6 MV Photons and 6 Mev Electrons Using Reflective Mode Scanners. Phys Med., 30(6), 708-712. doi: 10.1016/j.ejmp.2014.04.010.